Solar Physics (2025) 300:75
https://doi.org/10.1007/s11207-025-02485-1

RESEARCH

SUNRISE III: Overview of Observatory and Instruments

Andreas Korpi-Lagg · Achim Gandorfer · Sami K. Solanki · Jose Carlos del Toro Iniesta · Yukio Katsukawa · Pietro Bernasconi et al. ***[full author details at the end of the article]***

Received: 10 December 2024 / Accepted: 12 May 2025 / Published online: 30 May 2025
© The Author(s) 2025

Abstract

In July 2024, SUNRISE completed its third successful science flight. The SUNRISE III observatory had been upgraded significantly after the two previous successful flights in 2009 and 2013, to tackle the most recent science challenges concerning the solar atmosphere. Three completely new instruments focus on the small-scale physical processes and their complex interaction from the deepest observable layers in the photosphere up to chromospheric heights. Previously poorly explored spectral regions and lines are exploited to paint a three-dimensional picture of the solar atmosphere with unprecedented completeness and level of detail.

The full polarimetric information is captured by all three instruments to reveal the interaction between the magnetic fields and the hydrodynamic processes. Two slit-based spectropolarimeters, the SUNRISE UV Spectropolarimeter and Imager (SUSI) and the SUNRISE Chromospheric Infrared spectro-Polarimeter (SCIP), focus on the near-ultraviolet (309 – 417 nm) and the near-infrared (765 – 855 nm) regions respectively, and the imaging spectropolarimeter Tunable Magnetograph (TUMAG) simultaneously obtains maps of the full field-of-view of 46×46 Mm^2 in the photosphere and the chromosphere in the visible (525 and 517 nm). The instruments are operated in an orchestrated mode, benefiting from a new Image Stabilization and Light Distribution unit (ISLID), with the Correlating Wavefront Sensor (CWS) providing the autofocus control and an image stability with a root-mean-square value smaller than 0.005". A new gondola was constructed to significantly improve the telescope pointing stability, required to achieve uninterrupted observations over many hours.

SUNRISE III was launched successfully on 10 July 2024, from the Esrange Space Center of the Swedish Space Corporation near Kiruna (Sweden). It reached the landing site between the Mackenzie River and the Great Bear Lake in Canada after a flight duration of 6.5 days. In this paper, we give an overview of the SUNRISE III observatory and its instruments.

Keywords Sun: magnetic fields · Sun: photosphere · Sun: chromosphere · Sun: magnetic fields · Instrumentation: polarimeters · Stratospheric balloons · High angular resolution

1. Introduction

SUNRISE is the most powerful solar telescope ever to have left the ground. It escapes the disturbing influence of air turbulences by floating in the stratosphere above more than 99% of the Earth's atmosphere. This location opens up the important near-ultraviolet (near-UV) spectral range for study, which is hard to access from ground. During two successful flights

in 2009 and 2013, SUNRISE I and II demonstrated the potential of the observatory. The magnetic field and velocity data and the ultraviolet (UV) images of highest spatial and temporal resolution unaffected by atmospheric turbulence provided new insights into small-scale magnetic fields in the photosphere of the Sun.

In 2016, the work on SUNRISE III began. The observatory has been upgraded considerably, with three new science instruments, improved light distribution and image stabilization systems, and a new gondola. This expands the scientific scope of SUNRISE significantly, especially since it is now possible to seamlessly probe a greater range of heights in the solar atmosphere, ranging from the solar surface to the middle chromosphere. To achieve this goal, the new science instruments now cover the solar spectrum from the near-UV to the near-infrared (near-IR). The SUNRISE UV Spectropolarimeter and Imager (SUSI), a novel near-UV spectropolarimeter built by the Max Planck Institute for Solar System Research (MPS, Germany), explores and exploits the very rich, but, due to poor accessibility from the ground, so far little studied spectral range between 309 and 417 nm. The SUNRISE Chromospheric Infrared spectro-Polarimeter (SCIP), a near-IR spectropolarimeter, built jointly by the National Astronomical Observatory of Japan (NAOJ, Japan), the Spanish Space Solar Physics Consortium[1] (S^3PC, Spain) and MPS, specializes on the chromospheric Ca II infrared lines and on the upper photospheric K I lines around 770 nm, poorly accessible from the ground. The Tunable Magnetograph (TUMAG), a very fast tunable imaging spectropolarimeter able to access multiple spectral lines and built by S^3PC, delivers the high time and spatial resolution full field-of-view (FoV) information in both, the chromospheric and the photospheric layers, quasi-simultaneously.

A completely new gondola, designed and built by the Johns Hopkins University Applied Physics Laboratory (APL, USA), provides the pointing stability allowing the science instruments to benefit from the absence of a day-night cycle to obtain ultra-long time series. In combination with the Correlating Wavefront Sensor (CWS), contributed by the Institut für Sonnenphysik (KIS, Germany), an unprecedented pointing accuracy better than 0.005" root-mean-square (rms) is achieved over multiple hours, corresponding to a distance on the Sun of only 3.5 km. In addition, the CWS controls the optimum focus of the telescope in closed-loop and provides the information for the correction of a residual coma. The new instrument suite required a complete redesign of the Image Stabilization and Light Distribution unit (ISLID), containing not only the mirrors and beam splitters to feed the science instruments, but also the fast tip/tilt mirror controlled by the CWS for compensating residual image motion not corrected by the gondola. A powerful Instrument Control System (ICS) houses a multi-node workstation and the Data Storage System (DSS), capable of controlling all the instruments autonomously, storing science and housekeeping (HK) data, and responsible for the communication and commanding between ground station and observatory during the 6.5 days long flight.

SUNRISE III was launched on 10 July 2024, at the very end of the 40-day long launch window, defined by two boundary conditions: the sunset-free time around northern hemisphere summer solstice, and the presence of circumpolar stratospheric winds transporting SUNRISE III westwards from Esrange Space Center near Kiruna, Sweden, to north-western Canada at a float altitude of 33 – 37 km (see Section 2.2.1). During the flight, SUNRISE III completed its scientific program on a zero-pressure long-distance balloon (LDB) of NASA's

[1] The Spanish Space Solar Physics Consortium (S^3PC) is a consortium formed by the Spanish research institutes Instituto de Astrofísica de Andalucía (IAA), Instituto Nacional de Técnica Aeroespacial (INTA), Universitat de València (UV), Universidad Politécnica de Madrid (UPM), and Instituto de Astrofísica de Canarias (IAC) under the leadership of IAA (https://s3pc.es).

scientific balloon program (Balloon Program Office, BPO), operated by the Columbia Scientific Ballooning Facility (CSBF).

With this paper, we describe the scientific goals of the mission, and present an overview of the SUNRISE III hardware and its technical specifications. The paper is structured as follows: We start with the history of the SUNRISE project (Section 2), followed by a description of the scientific topics to be addressed with SUNRISE III (Section 3). The observatory with all its subsystems is described in Section 4, including the thermal concept. Section 5 summarizes the most important tests and the path towards flight readiness. We conclude the paper with a brief overview of the scientific performance and the data concept and policy in Section 6, and present a summary in Section 7.

2. SUNRISE History

The SUNRISE project is one of the long-term scientific pillars of MPS. It started already in the beginning of this millennium at the Max-Planck-Institut für Aeronomie (MPAe) in Katlenburg-Lindau (Germany), which was renamed to MPS in 2004. In this section, we briefly recapitulate the history of the SUNRISE observatory and its science, including the successful flight of SUNRISE III in 2024.

2.1. SUNRISE I and II

The SUNRISE observatory is composed of a telescope with a 1 m aperture. For the first two flights, it was equipped with two scientific instruments, the Imaging Magnetograph eXperiment (IMAX) and the SUNRISE Filter Imager (SUFI). Additional important subsystems were the CWS providing the signal needed to stabilize images to the necessary precision, the ISLID, the on-board computer and data storage system, and a protective gondola. The instrumentation flown during the first flight of SUNRISE in June 2009 has been described by Barthol et al. (2011), Martínez Pillet et al. (2011), Gandorfer et al. (2011); and Berkefeld et al. (2011).

Two successful long-duration science flights on a zero-pressure stratospheric balloon took place in June 2009 (under solar activity minimum conditions; referred to as SUNRISE I) and in June 2013 (at a relatively high activity level; SUNRISE II). The missions were operated and launched from Esrange Swedish Space Corporation (SSC) in Kiruna, Sweden. After launch, the balloon slowly drifted westward, reaching northern Canada after 5 days, where the payload landed safely without major damage. The entire payload was successfully recovered after both flights. Overviews of the two flights (SUNRISE I and II), the instrumentation, the data gathered, and of some of the early science are given by Solanki et al. (2010, 2017), respectively. SUNRISE I and II provided data that are diffraction-limited at wavelengths as short as 300 nm, making these the highest resolution solar images until then. They also provided the highest resolution solar data at 214 nm and at 279.5 nm and excellent polarimetric precision in the visible wavelengths.

The first scientific results from the two flights were published in special issues of *Astrophys. J. Lett.* (see Solanki et al. 2010) and *Astrophys. J. Suppl. Ser.* (see Solanki et al. 2017; Solanki 2017), respectively.

2.2. SUNRISE III

The data from SUNRISE I and II were mainly sensitive to the solar photosphere and the lowest layers of the chromosphere. They could not provide detailed insight into the influence of

the small-scale dynamical and magnetic photospheric phenomena on the overlying layers of the atmosphere, in particular the chromosphere. SUNRISE III carries dedicated instruments that spectropolarimetrically sample both the photospheric sources and the chromospheric response in a multitude of spectral lines over a broad wavelength range from about 309 to 855 nm.

The SUNRISE I and II experience as well as general advances in solar physics have shown the need for seeing-free observations at high resolution that make simultaneous use of narrow-band polarimeters, broad-band imagers, and scanning slit-spectropolarimeters. These instruments complement each other by, on the one hand, allowing to follow rapidly evolving features, while, on the other hand, providing detailed diagnostics and the 3-dimensional stratification of the relevant physical parameters in the solar atmosphere, including the magnetic field. Such a carefully balanced set of instruments was chosen to form the core of the new SUNRISE payload.

The SUNRISE UV Spectropolarimeter and Imager (SUSI, see Section 4.4.1, Feller et al. 2020, 2025) on SUNRISE III images and spectropolarimetrically explores the wavelength range 309 – 417 nm at high spatial resolution. The possibilities of this wavelength range are exciting, as it provides a large number of lines that can sample the chromosphere, and also resolve weak magnetic fields using the Hanle effect. Furthermore, the high density of spectral lines allows analysing their polarization signals jointly to increase the signal-to-noise (S/N) ratio and also enables sampling many heights in the solar atmosphere simultaneously.

The Tunable Magnetograph (TUMAG, see Section 4.4.2, Álvarez Herrero et al. 2022; del Toro Iniesta et al. 2025) performs narrow-band imaging polarimetry in the visible, employing the Fe I 525.02/525.06 nm photospheric line pair, with the first line being highly magnetically sensitive (effective Landé factor $g = 3$), plus the Mg I 517.27 nm line, sampling the boundary between the chromosphere and photosphere. TUMAG allows dynamic events to be followed and connections across the full FoV of 46×46 Mm^2 to be made.

Spectropolarimetry in two of the Ca II infrared triplet lines, carried out by the SUNRISE Chromospheric Infrared spectro-Polarimeter (SCIP, see Section 4.4.3, Katsukawa et al. 2020, 2025), provides diagnostics with a proven capability of deducing the 3D structure of the chromospheric magnetic field through non-local thermodynamic equilibrium (non-LTE) inversions. In addition, the line core is formed particularly high in the solar atmosphere, and with the high Zeeman sensitivity and photon flux, a good S/N ratio can be obtained already at rather short exposure times. Together, these attributes allow high precision polarimetry at high spatial and temporal resolution. The temperature minimum heights above the photosphere are probed with the K I 769.9/766.5 nm lines, which have extremely high velocity sensitivities, and are poorly accessible from the ground due to telluric blends.

However, the full power of SUNRISE III lies in simultaneously probing (through both spectropolarimetry and imaging) the near-UV, while simultaneously carrying out narrow-band polarimetric imaging in the visible and spectropolarimetry in the infrared. Together, this makes SUNRISE III a unique observatory, with capabilities going far beyond those that were available during the first two flights. One shortcoming of previous flights was the relatively short continuous time series, due partly to the limited time for which the gondola could maintain stability. This has been countered by improvements in the internal image stabilization system, the CWS (Berkefeld et al. 2025), and by employing a new gondola (see Section 4.1, Bernasconi et al. 2025).

The new instrumentation and the improvements in the image stabilization required a complete new design for the ISLID and the Post Focus Instrumentation (PFI) platform (see Section 4.3). A redesign of the Heat Rejection Wedge (HRW), which limited the length of time series during the latter part of the SUNRISE II mission, ensures that it poses no such

limitations during the flight of SUNRISE III. A new ICS (see Section 4.5.2) was developed to cope with the increased complexity of the observatory, and the significantly higher data rates from the scientific instruments. Consequently, also the harness concept and the onboard network infrastructure had to be renewed.

SUNRISE III had an unsuccessful flight on 10 July 2022, caused mainly by non-ideal launch conditions. The mission had to be aborted only 6 hours after the launch, because the launch-lock mechanism, designed to hold the telescope in place in the gondola during the launch and the ascent/descent phases, did not withstand the unduly strong acceleration during the release of SUNRISE III from the launch vehicle. Strong winds at an altitude of 100 to 300 m above the launch pad resulted in an approximately ten times higher release shock than typical for previous launches of balloon payloads. The bolts of the launch-lock mechanism were not designed for this shock and sheared off, allowing the telescope to move freely in elevation. Unfortunately, the telescope got stuck at an elevation of $\approx 60°$, and all attempts to move the telescope during the short excursion into the stratosphere failed. The landing of the observatory, still in Sweden close to the Norwegian border, was rather smooth and the observatory could be recovered after 10 days with marginal damage to the scientific payload.

As part of the preparations for the re-flight in 2024, the observatory was cleaned of any dirt accumulated during the 10 days spent on a Swedish hillside, refurbished and thoroughly tested. This included re-coating the main and the secondary mirrors (M1 and M2) as well as the folding mirrors M3 and M4, a repair of the tilt mechanism for the etalon within TUMAG, the high-precision re-alignment of the telescope and the scientific instruments, and the detailed testing of all scientific instruments and mechanisms. In addition, the launch-lock mechanism was strengthened to withstand even rougher launch conditions than those seen during the 2022 launch.

2.2.1. SUNRISE III Flight in 2024

Exactly two years after the 2022 mishap, SUNRISE III started on its second science flight on 10 July 2024, at 04:22:40 UTC from Esrange under CSBF flight number 740N (see Figure 1). The release from the launch vehicle was again quite rough, but the reinforcements in the launch-lock mechanism were effective and kept the telescope in place. At 07:34 UTC the float altitude of 37.5 km was reached, and the stratospheric float winds transported SUNRISE III to the west on a trajectory at a latitude between 64.5° and 67°, significantly more southward than the previous two successful flights. The SUNRISE III flight trajectories are displayed in Figure 2 (*top* panel), along with the information about the solar elevation and the flight altitude (*bottom* panel).

Directly after reaching float altitude, the commissioning phase was started at the Göttingen Operations Center (GOC), from where all the science operations were executed (see Section 5.9). All subsystems were operational and in good condition, so that on 10 July at 17:05 UTC the first scientific program could be started. All pre-defined programs could be executed according to the priorities defined in the daily meetings of the SUNRISE Science Working Group (SSWG). Despite the southward trajectory, SUNRISE III did not see any sunset, but the telescope elevation was negative for about 2 to 4 hours around local midnight (the horizon at float altitude is at $-4.9°$, see *blue solid* line in Figure 2, *bottom*). During this time the observations were affected by the absorption and seeing caused by observing the Sun through the Earth's atmosphere.

Science operations ended on 16 July 2024 at 15:00 UTC. Flight termination occurred at 18:20:54 UTC at the position 66°07'47"N 127°12'06"W. The observatory impacted



Figure 1 SUNRISE III a few minutes before the launch on 10 July 2024 on the balloon pad of Esrange space center. The balloon is already fully inflated, the red and white parachute is attached to the flight train, that stretches over the launch vehicle to the observatory. Image courtesy: SSC / Mattias Forsberg.

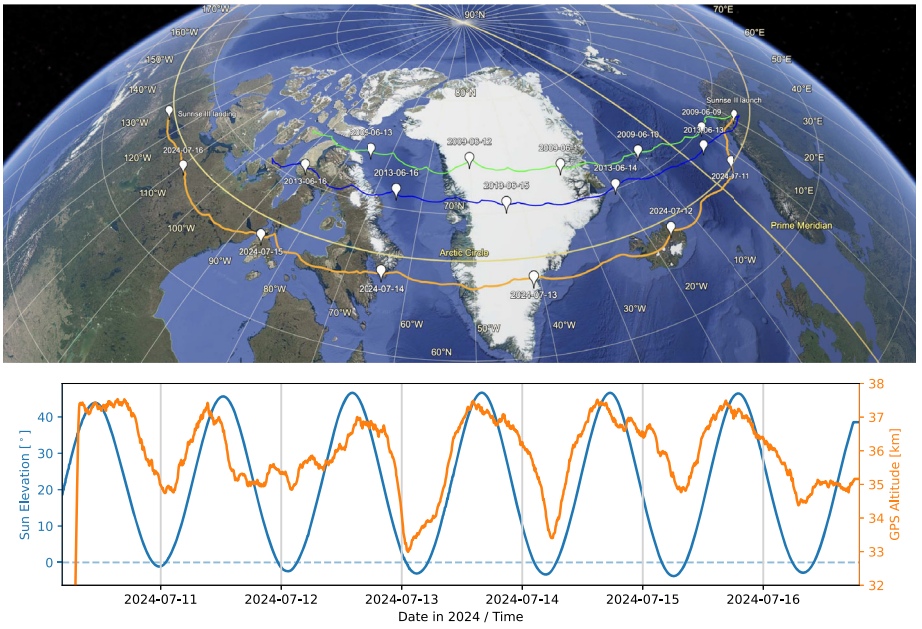


Figure 2 *Top*: Trajectories of the three successful SUNRISE flights: SUNRISE I (*green*), SUNRISE II (*blue*), and SUNRISE III (*orange*). *Bottom*: Sun elevation angle (*blue*) and flight altitude obtained from the gondola GPS receiver (*orange*) for SUNRISE III. Background map: Google Earth (data attribution: Google Landsat / Copernicus Data SIO, NOAA, U.S. Navy, GEBCO IBCAO U.S. Geological Survey INEGI).

on 16 July 2024, at 19:09:00 UTC west of Great Bear Lake in Canada (66°28'34.8"N 127°00'00"W), marking a total flight duration of 6 days, 14 hours and 46 minutes (total float time: 6 days, 10 hours, 47 minutes). The landing site was located in a forest, making the recovery operations more difficult than expected. The recovery team first secured the data vaults, and completed the dismantling of the observatory on 29 July 2024 with the final helicopter transport from the landing site to the airport of Norman Wells. A winged airplane continued the transport to Yellowknife Airport on 05 August 2024, where the observatory was loaded into two shipping containers, marking the end of the recovery operation. The data vaults were transported to MPS by the recovery team.

The observatory worked extremely stably and reliably. Two technical issues interrupted scientific observations for a short time. The power supply by the photovoltaic system stopped working twice, forcing SUNRISE III to run on batteries. Both times, the battery charging could be reestablished and normal operation resumed. The gondola Pointing Control System (PCS) had only one major pointing loss on the last day of the mission, exceeding the scientists' high expectations. The full potential and quality of the SUNRISE III dataset can only be assessed after the data have been reduced.

2.2.2. Scientific Performance During the 2024 Flight

During the 6.5-day-long flight, SUNRISE III recorded more than 200 TByte of data. Using the preflight-defined sequences of science observations and calibrations described in Section 3.2.1, and exploiting all the various instruments observing modes, we targeted a wide variety of solar features. The observatory executed successfully all high-priority predefined observing programs. Additionally, through daily science planning meetings, we performed many additional observations based on thorough analysis of the real-time solar features.

The total campaign duration from launch to landing was 155.77 h. First light in flight occurred 3.5 h after launch with the opening of the aperture door, which stayed open for 97.7% of the remaining flight duration until termination. For 102.7 h (68%) the CWS was in state 1, indicating that stable locking and auto-focus was established, either on a solar feature, or on an F2-filter wheel target for calibration purposes (see Section 4.3.1) For the remaining 24.6% of the time the observatory was either in flatfielding mode or in other calibration modes (e.g., taking dark images). The total time of science observation was 68 h. Other non-observing times covered periods of negative solar elevation (a result of the southern trajectory) and setup procedures (e.g., finding the right target for the observations).

The solar targets covered the quiet Sun, plage and network field regions, a coronal hole, sunspots, and flaring regions. Center to limb variations were recorded, including observations at the limb. All instrument modes were executed, like the full spectral scan of the SUSI instrument over the spectral region from 309 – 417 nm, the interlaced observation between the photospheric Fe I 525 nm line and the chromospheric Mg Ib 517.3 nm line by TUMAG, or the rapid scan mode by SCIP. While TUMAG always observed with the full FoV of 63" × 63", SUSI and SCIP varied their scanning region from sit & stare observations over narrow, repetitive scans, to 60" large scans, always using the 60" full slit length, and within the FoV of TUMAG.

3. SUNRISE III Science

3.1. Science Objectives

SUNRISE III is a high-spatial resolution solar observatory. The large-aperture solar telescope combined with the state-of-the-art image stabilization allows SUNRISE III to resolve solar

features down to a size of 60 km at the shortest wavelength, which is within a factor of two of the theoretical resolution limit of the National Science Foundation's Daniel K. Inouye Solar Telescope (DKIST: Rimmele et al. 2020; Rast et al. 2021) at 600 nm. The stratospheric vantage point above 99% of the Earth's atmosphere provides an image stability over multiple hours not achievable from the ground, similar to space-borne instruments, like the Spectro-Polarimeter (SP) and the Narrowband Filter Imager (NFI) of the Solar Optical Telescope (SOT) aboard *Hinode* (Kosugi et al. 2007; Tsuneta et al. 2008), the Helioseismic Magnetic Imager (HMI) on Solar Dynamics Observatory (SDO: Pesnell, Thompson, and Chamberlin 2012; Schou et al. 2012; Scherrer et al. 2012) or the Polarimetric and Helioseismic Imager (PHI) on Solar Orbiter (Solanki et al. 2020; Müller et al. 2020). Compared to space missions, balloon-borne observatories have less restrictions on payload mass and data rate (data can be stored on-board and recovered), and can rely on standard, off-the shelf components. This allows SUNRISE III to be equipped with significantly more complex and versatile instrumentation than possible for a space mission at relatively low costs (see Iglesias and Feller 2019, for a comparison of state-of-the-art instrumentation for spectropolarimetry). The space-like observing conditions allow to simultaneously cover wavelengths from the near-UV to the near-IR for nearly the whole 6.5-day long flight. This makes SUNRISE III well suited to address important topics in the physics of solar magnetism and its manifestations in the lower solar atmosphere.

3.1.1. The Crucial Role of the Magnetic Field

Magnetic fields in the solar atmosphere are the root cause of the many phenomena that together constitute solar activity (e.g., Solanki, Inhester, and Schüssler 2006). Hereby, the interaction of the magnetic field with the solar plasma is of fundamental importance, since it is the key to the conversion of energy between its mechanical, magnetic, radiative, and thermal forms. The interaction between the turbulent solar convection (Nordlund, Stein, and Asplund 2009) and the magnetic field leads to a rich variety of magnetic structures in the photosphere at many scales.

Equally fascinating, but less understood is the solar chromosphere (e.g., Lagg et al. 2017; Carlsson, De Pontieu, and Hansteen 2019), directly overlying the photosphere. There the magnetic energy density, the thermal energy density and the kinetic energy density in waves and flows are all of roughly equal magnitude, so that they can be easily transformed into each other. This leads to a very dynamic environment, with many complex interactions. These give rise to structures as diverse and dynamic as canopies of magnetic field, jet-like spicules, and prominences of dense material dangling on magnetic field lines high up in the thin atmosphere.

Mechanical and magnetic energy is injected into the solar atmosphere in the turbulent and dense photospheric layers. Most of this energy is deposited in the chromosphere, where it heats the gas and drives its dynamics, and much of the rest is converted into another form there. Therefore, it has become increasingly clear in the past few years that to understand the flow of energy in the solar atmosphere, both photosphere and chromosphere must be studied simultaneously. In particular, the magnetic field in these two layers must be investigated in detail at the highest achievable resolution (because many of the key interactions take place at small scales), but also with the best possible sensitivity (to catch the weak magnetic flux that dominates a large part of the quiet Sun).

3.1.2. The Complex Magnetic Field in the Photosphere

The magnetic field in the solar photosphere shows a very complex and diverse structure (e.g. Solanki 1993). Magnetic-flux concentrations of kG strength appear in a broad range of

sizes: from sunspots, with diameters reaching up to 50,000 km, to small flux concentrations on a scale of 30 – 100 km (Stein 2012). In addition to these strong-field features, turbulent magnetic fields pervade the photosphere.

The flux concentrations on the small-scale end of the size distribution have field strengths of 1 – 2 kG (Stenflo 1973). The first flight of SUNRISE (SUNRISE I) provided the first spatially resolved observations of such small-scale flux concentrations with kG fields in the quiet Sun internetwork (Lagg et al. 2010; Martínez González et al. 2012). State-of-the-art magneto-hydrodynamic (MHD) simulations and SUNRISE data have also shown that the magnetic elements are extremely dynamic. Thus, the convective intensification of such magnetic features in the quiet Sun often only lasts a minute or two and they constantly break up or merge with other features (e.g., Requerey et al. 2014, 2017; Anusha et al. 2017). To follow these complex dynamics, a near-perfect and time-independent image quality is required, which is difficult to be achieved from the ground.

The large magnetic features such as dark pores and sunspots also display a host of dynamic small-scale structures (Solanki 2003). Numerical simulations indicate that magnetic filamentation is the key to understanding energy transport in sunspot umbrae and the surrounding penumbrae (Schüssler and Vögler 2006; Rempel et al. 2009; Rempel and Schlichenmaier 2011; Rempel 2012). SUNRISE III allows testing the predictions from the simulations (and hence the validity of the simplifications underlying them) by spectropolarimetrically investigating the structure and dynamics of sunspots on their intrinsic spatio-temporal scales, thus revealing the mode(s) of energy transport acting in them.

Besides the magnetic-flux concentrations there are mixed-polarity magnetic features all over the solar surface, constituting a turbulent magnetic field (Danilovic, Schüssler, and Solanki 2010a; Borrero et al. 2017; Bellot Rubio and Orozco Suárez 2019). The field strengths in these features are often quite low. This, together with the mixing of magnetic polarities at very small scales, implies that such fields are very hard to catch using the Zeeman effect generally employed to measure solar magnetic fields. The Hanle effect, a quantum interference effect, which is most potent in the UV, is the method of choice for examining the properties of turbulent fields, as it does not suffer from the problems besetting the Zeeman effect (Stenflo 1994). The Hanle effect combined with the stable conditions offered by a balloon-platform is ideal for finally determining the true distribution of the so far hidden magnetic energy proposed to reside in the quiet Sun (e.g., Trujillo Bueno, Shchukina, and Asensio Ramos 2004).

To probe both the strong, more organized, and the weak, more turbulent fields, a combination of Hanle and Zeeman diagnostics in multiple spectral lines is needed. Meeting this goal of SUNRISE III requires instruments probing additional wavelengths to those covered by SUNRISE I and II.

3.1.3. Turbulent Magnetoconvection: Origin and Fate of Magnetic Flux

The emergence of magnetic flux in the photosphere is frequent and widespread (e.g., Centeno et al. 2007; Martínez González et al. 2007; Thornton and Parnell 2011). Bipolar structures appear over a large range of sizes, from sunspot-forming, coherent magnetic flux bundles in the tens of Mm range (e.g., Stenflo and Kosovichev 2012; Cheung and Isobe 2014; Chen, Rempel, and Fan 2017) down to scales barely detectable with current solar telescopes. These small-scale emergences happen continuously in every single granule, and various aspects of their turbulent nature were already uncovered by the SUNRISE I and II flights (Danilovic et al. 2010; Guglielmino et al. 2012; Anusha et al. 2017; Centeno et al. 2017; Smitha et al. 2017). SUNRISE III observations add the height information about the physical

conditions during these emergences and allow to determine their role in shaping the higher atmospheric layers of the Sun. The high activity level during the 2024 flight and the long time series not only provide detailed statistics of these tiny emergences, but also increase the likelihood of capturing the rise of a larger bipolar magnetic bundle and its complex, small-scale interaction with the turbulent convective cells (Weber et al. 2023).

The processes by which the magnetic flux is removed from the solar surface are even less well known, mainly because much of it is thought to happen at very small spatial scales. Flux removal has to take place at the same, very high average rate as the emergence of new flux, to keep the total flux in balance. It is expected that all the magnetic flux in the quiet Sun is replaced within 1 – 3 days (Schrijver et al. 1997; Lamb et al. 2013). Although there are a number of processes which can remove flux, only two of these are accessible to observations: submergence of Ω-shaped magnetic loops to below the surface and ejection of U-shaped loops from the Sun (Zwaan 1987; Cameron, Vögler, and Schüssler 2011). Magnetic reconnection is likely to play an important role in both flux removal processes (van Ballegooijen and Martens 1989) and consequently provides a considerable amount of energy for local heating and acceleration of plasma jets (Thaler and Borrero 2023). Observational studies of flux removal have not delivered any clear results favouring one or the other mechanism (Bellot Rubio and Orozco Suárez 2019). Flux removal and associated processes generally take place on or below the spatial scale of the individual flux elements and over a large range of heights, making observations at high spatial resolution and height coverage mandatory. SUNRISE I and II already revealed a large number of cancellation events (Centeno et al. 2017; Anusha et al. 2017). However, only a spectropolarimeter sampling a number of spectral lines simultaneously, together with a vector magnetograph, allows the full three-dimensional evolution of the magnetic field in a cancelling event to be followed and thus the various possible scenarios of flux removal to be distinguished.

3.1.4. The Upper Solar Atmosphere

The atmospheric layers above the solar photosphere are of fascinating beauty, but still full of mystery when it comes to the understanding of the underlying physical processes. The chromosphere with its poorly studied magnetic field has increasingly moved into the focus of solar physics in recent years (Lagg et al. 2017; de la Cruz Rodríguez and van Noort 2017; Molnar et al. 2019; da Silva Santos et al. 2022; Rouppe van der Voort, van Noort, and de la Cruz Rodríguez 2023; Kuridze et al. 2024). Its structure and dynamics are characterized by the interaction of plasma flows, waves, radiation and magnetic field. Because the plasma-β, i.e., the ratio between thermal and magnetic energy density, may drop below unity in parts of the chromosphere, and the kinetic energy density in shock waves can reach the thermal energy density, the chromosphere provides the appropriate conditions for the easy conversion of energy from one of these forms to another.

How the chromospheres and coronae of the Sun and other stars are heated is one of the outstanding open problems of solar and stellar physics. Although on average only 8000 K hot, the chromosphere, by dint of its higher density, requires a factor of 2 – 10 larger energy input than the corona to maintain its temperature (Withbroe and Noyes 1977; Anderson and Athay 1989). The key lies in the magnetic field with its decisive role in heating large parts of the chromosphere and the corona (Judge et al. 2024). At the solar surface, the magnetic field interacts strongly with turbulent convection and is moved around by the flows, imparting the energy from the flow to the field. Slow motions of the plasma braid magnetic field lines, inducing currents in the upper solar atmosphere (Parker 1983; Klimchuk 2006; Pontin and Hornig 2020). Rapidly varying surface motions excite a multitude of MHD wave modes

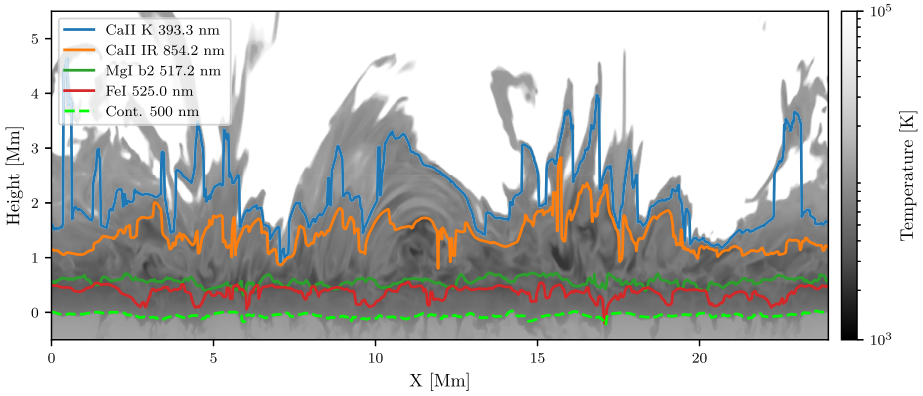


Figure 3 Vertical cut showing the temperature stratification in a MURaM-ChE simulation. The heights for optical depth unity for the continuum at 500 nm and for selected spectral lines observed by the SUNRISE III instruments are indicated by the *colored solid* lines.

that carry energy as they propagate upwards (Jess et al. 2009; van Ballegooijen et al. 2011). Interaction of an existing magnetic structure with nearby opposite polarity fields can lead to magnetic reconnection in the lower atmosphere. This heats the local plasma, which is then injected into the upper regions in the form of small (Chitta et al. 2017, 2020), or larger jets (Shibata et al. 2007; Matsumoto et al. 2023, see also Figure 4). Self-interactions of undulated flux tubes can also induce magnetic reconnection in the emerging flux region, manifesting themselves as Ellerman bombs (Georgoulis et al. 2002; Vissers et al. 2015; Rouppe van der Voort, Rutten, and Vissers 2016; Kawabata et al. 2024). Finally, magnetic vortex flows with twisted magnetic fields, so-called solar tornadoes, have been identified as an additional source of energy transfer into the upper atmosphere (Wedemeyer-Böhm et al. 2012).

Signatures of some of these processes have been observed. For example, various modes of MHD waves were found in the solar atmosphere (Jess et al. 2009; McIntosh et al. 2011), although energy estimates may be uncertain (e.g., Yadav, Cameron, and Solanki 2021). For braiding, mainly indirect observational evidence has been reported (Peter, Gudiksen, and Nordlund 2004), except for the rare cases of direct observations (Cirtain et al. 2013; Chitta et al. 2022), which still leave important questions unanswered. To determine the contribution of these processes to chromospheric and coronal heating, knowledge of the physical quantities (temperature, density, velocity, and magnetic field) in the photosphere and in the chromosphere is required. Recent MHD simulations with the chromospheric extension of the MPS/University of Chicago Radiative MHD code (MURaM-ChE: Przybylski et al. 2022) demonstrate the need for the high spatial, height, and temporal resolution of such measurements to characterize the fine-structured and strongly dynamic chromospheric plasma (Rouppe van der Voort, van Noort, and de la Cruz Rodríguez 2023; de la Cruz Rodríguez and Leenaarts 2024). A snapshot of the temperature stratification from a MURaM-ChE simulation is shown in Figure 3. It illustrates the small-scale nature of the chromospheric features, and how strongly the optical-depth-unity surface varies in height, indicated for some of the spectral lines observed by the SUNRISE III instruments.

Most chromospheric spectral lines have a rather limited sensitivity to the magnetic field, which is generally weak in the chromosphere compared with its photospheric counterpart (de la Cruz Rodríguez and van Noort 2017). The near-UV, observed by the SUSI spectropolarimeter, contains a large number of magnetically sensitive spectral lines, increasing the

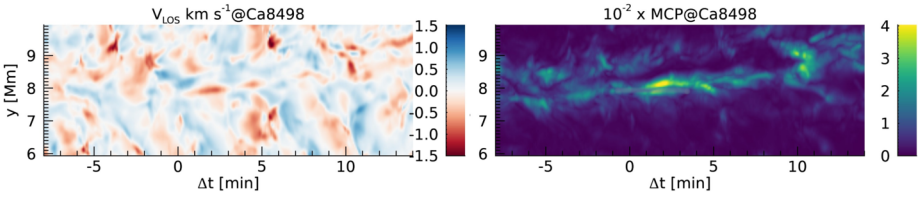


Figure 4 Simulated SCIP observation in the Ca II 849.8 nm line showing the temporal evolution of a chromospheric jet (adopted from Matsumoto et al. 2023, Figure 5). The time-distance diagram of the line-of-sight velocity (v_{LOS}, *left*) and the maximum amplitude of circular polarization (MCP, *right*) demonstrate the highly dynamic nature of the chromosphere.

sensitivity of the chromospheric magnetic field measurements when many lines are observed simultaneously (Riethmüller and Solanki 2019). Small scans over narrow FoV provide the necessary high cadence to capture the dynamics and, with long and constant-quality time series of such small scans, the signature of the various MHD wave modes. A unique feature of observations from the stratosphere is the absence of atmospheric refraction, which allows obtaining co-spatial and co-temporal information also in the near-IR Ca II line observed by SCIP. Time-distance diagrams like the one shown in Figure 4 (adopted from Figure 5 of Matsumoto et al. 2023) for this spectral line can be created from these small scans for all relevant atmospheric parameters and at multiple height layers. By embedding these scans in the high-cadence maps of the photosphere and the chromosphere provided by TuMag, Sunrise III provides the magnetic field information at high spatial and height resolution, high cadence and high S/N, and thus hopefully helping to solve many mysteries of the chromospheric magnetic field.

3.1.5. The Small-Scale Dynamo

The continuous dissipation of magnetic flux and its ejection from the Sun requires its constant replenishment by magnetic-field generating or amplifying processes. In the current understanding, a large-scale dynamo is operational in the solar convection zone, and this mechanism, powered by non-uniform rotation, convection and buoyancy, results into the generation of large bipolar regions (for an overview see Charbonneau and Sokoloff 2023). For the magnetism in the quiet Sun, 3-dimensional MHD simulations make the exciting prediction that a small-scale turbulent dynamo operates in the Sun (Petrovay and Szakaly 1993; Cattaneo 1999; Vögler and Schüssler 2007; Rempel 2014; Hotta, Rempel, and Yokoyama 2015; Khomenko et al. 2017; Rempel et al. 2023; Warnecke et al. 2023). The relevance of a small-scale dynamo for the fields measured in the solar atmosphere is still controversial (Stenflo 2012; Martínez-Sykora et al. 2019; Ebert, Milic, and Borrero 2024), and an observational proof of its existence is extremely difficult (Danilovic, Schüssler, and Solanki 2010b; Shchukina and Trujillo Bueno 2011; Buehler, Lagg, and Solanki 2013; Lites, Centeno, and McIntosh 2014; Danilovic et al. 2016). Tests carried out so far suffer from non-ideal, sometimes inhomogeneous datasets. Time series at a constant very high spatial resolution, reliably covering all photospheric heights are needed to address this question.

Another promising observational approach relies on the technique of local helioseismology (Gizon and Birch 2005; Gizon, Birch, and Spruit 2010), allowing to probe the convection in the layers immediately below the surface (Singh, Raichur, and Brandenburg 2016; Korpi-Lagg et al. 2022; Waidele et al. 2023). To achieve this aim, long (three hours or more) time series of velocity and magnetic field at highest spatial resolution are needed. Providing

such time series at constant quality is a unique feature of SUNRISE III and cannot be obtained from the ground, due to the ever-present and fluctuating image degradations caused by turbulence in the Earth's atmosphere.

3.1.6. Exploration of the Polarized Solar Spectrum in the Near-UV

The polarization properties of the solar spectrum are poorly known over most of the wavelength interval between 300 and 400 nm. At these short wavelengths, it becomes increasingly challenging to obtain high-resolution data from the ground, and basically impossible to do so with a good S/N ratio, owing to the strong absorption and Rayleigh scattering by the air molecules in the Earth's atmosphere. The strong absorption requires prohibitively long integration times when approaching the short-wavelength end of this spectral range, while the Rayleigh scattering introduces significant stray light contamination that strongly dilutes the intrinsic polarization signals. Both limitations can only be addressed by observing from above most of the Earth's atmosphere, as is the case for SUNRISE III. No space mission has yet covered these wavelengths at high spatial resolution, so that SUNRISE III provides the first high resolution spectropolarimetric data in this wavelength band, opening up new discovery space, and enhancing our understanding of the so-called 'second solar spectrum' (Stenflo and Keller 1997; Gandorfer 2005).

In spite of being poorly studied, the near-UV is of particular interest for a number of reasons: Firstly, the near-UV contributes dominantly to the irradiance variability of the Sun (i.e. to the variation of the Sun's total radiative output), and is a strong driver of the chemistry of the Earth's stratosphere (Krivova, Solanki, and Floyd 2006; Haigh et al. 2010; Solanki, Krivova, and Haigh 2013). The Sun's UV variability is prototypical of that displayed by other stars, which can have an important influence on the habitability of exoplanets.

Secondly, the near-UV part of the solar spectrum harbours a very high density of spectral lines, allowing for the use of many-line Zeeman and Hanle diagnostics (Solanki and Stenflo 1984; Riethmüller and Solanki 2019). The line density between 300 and 400 nm is more than four times larger than that between 500 and 600 nm, so that the information content of a far larger number and variety of spectral lines can be made use of than in the visible or infrared. Riethmüller and Solanki (2019) demonstrated also that the polarization signals of many of the spectral lines are very strong, with peak values between 30 and 40% even for the small flux concentrations in magnetically quiet areas of the Sun.

In addition, the near-UV harbours many spectral lines whose diagnostic potential is largely unexplored. To assess this potential, we computed the formation heights (the heights where the opacity at the given wavelength reaches unity) of $\approx$ 60,000 spectral lines in the SUSI wavelength range from the Kurucz line-list database (Kurucz and Bell 1995), and present the result in Figure 5. The computations were performed using the radiative transfer code RH (Uitenbroek 2001; Pereira and Uitenbroek 2015) with a FALC model atmosphere (Fontenla, Avrett, and Loeser 1993), and all spectral lines were treated in local thermodynamic equilibrium (LTE), except the Ca II H&K lines which were treated in non-LTE. Figure 5 demonstrates that, in sharp contrast to the handful of chromospheric lines that can be found in the visible and near-infrared, more than 150 lines form above 600 km, i.e., are clearly chromospheric. Because of the large number of chromospheric lines in the UV, and their widely varying thermodynamic sensitivities, this spectral range opens a new window to studying the chromospheric structure, dynamics and magnetic field and offers seamless height coverage from the deepest photospheric layers up to heights of 2000 km.

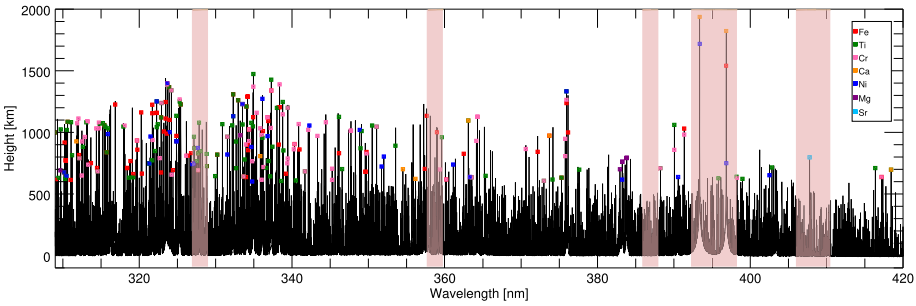


Figure 5 Formation height of ≈ 60,000 spectral lines in the SUSI spectral range from 309 to 417 nm. The highest forming lines (above 600 km) of a few selected species are indicated by *colored* symbols. The shaded regions indicate the six most requested SUSI spectral windows, with two windows overlapping at the Ca II H&K lines around 390 nm.

3.2. Preparing for SUNRISE III Science and Operation Planning

Parallel to the hardware development phase, the SUNRISE partner institutes established the SUNRISE Science Working Group (SSWG). The main task of this working group was to develop an observation strategy for the flight, which exploits fully the unique capabilities of the observatory, and satisfies the demands by the international community of solar researchers. Prior to the 2022 flight, more than 60 science proposals requesting access to data or specific observations were collected, and nine proposals were accepted within the SOLARNET Transnational Access program. Since much of the science of SUNRISE III is unique, the science proposals could be used unaltered as the basis for the observations during the 2024 flight.

3.2.1. Timeline Concept

A timeline concept was developed to operate all science instruments and the Pointing Control System (PCS) in an orchestrated mode controlled by the ICS. This concept ensures not only a nearly autonomous operation of SUNRISE III (important if real-time communication with the observatory is disturbed or slow), but also the efficient use of the limited observing opportunities. The aim was to gather data with a given instrumental setup and solar target that fulfil the requirements of as many as possible of the observing proposals submitted. Data from a single observing program enable a variety of analyses with different scientific goals.

The timeline consists of individual observing blocks, concatenating the scientific observing modes of every instrument, defined by specific settings (e.g., FoV, wavelength, scan-speed), with the necessary calibration measurements required to ensure that the recorded data can be reduced on ground with the best possible accuracy.

Figure 6 shows, as an example, the observing block 'SP_2', defining an observation dedicated to study the penumbral fine structure. The top panel of Figure 6 is an excerpt of the science planning sheets: A 12-minute full-FoV context scan by SCIP and SUSI (mode 'SP3') is followed by a 3-hour long observation ('SP8') with the spectrograph slits placed along a penumbral filament: SCIP provides narrow 1" scans with a time resolution of 12.5 s, while the SUSI slit is moved over a slightly wider region of 3" in 37.5 s. During the whole time, TUMAG observes the full FoV, quasi-simultaneously in the photosphere and the chromosphere. The bottom panel of Figure 6 presents the details of the observing block 'Spot

		SCIP				SUSI					TuMag		
No.	Target	FOV	Exposure	Scan time	Duration (min)	FOV	Scan speed ("/s)	Sp. window	Scan time	Duration (min)	Mode	Cadence	Duration (min)
SP3	Sunspot	58"	1.0s (N1F)	11.9 min	11.9	58"	0.0812	410.5-407.5	11.9 min	11.9	Obs 1 + Obs 2	70.4s	191.9
SP8	Sunspot penumbra	1"	1s (N4F)	12.6s	180	3"	0.08	327-329	37.5s	60			

State						Duration	Timestamp	
TuMag	SUSI	SCIP	ICU	PS	CW		Start	End
Reset	Reset	Reset	Open	Pointing	Autolock	0:02:40	0:00:00	0:02:40
Setting	Wavelength (328.8 nm)	Camera setting	Open	Pointing	Autolock	0:00:10	0:02:40	0:02:50
Prefilter	Wavelength (328.8 nm)	preobs	Open	Pointing	Autolock	0:04:00	0:02:50	0:06:50
call_2	call_2	call_2	call_2	call_2	call_2	0:59:27	0:06:50	1:06:17
finepoint	finepointing	finepointing	finepoi	finepointing	finepointir	0:01:00	1:06:17	1:07:17
Idle	Idle	Camera setting	Open	Pointing	Autolock	0:00:05	1:07:17	1:07:22
SP3	SP3	SP3	Open	Pointing	Autolock	0:12:30	1:07:22	1:19:52
SP3	Wavelength (328 nm)	Camera setting	Open	Pointing	Autolock	0:02:10	1:19:52	1:22:02
SP8	SP8	SP8	Open	Pointing	Autolock	3:00:00	1:22:02	4:22:02
call_2	call_2	call_2	call_2	call_2	call_2	0:59:27	4:22:02	5:21:29
Ping	Ping	Ping	Open	Pointing	Autolock	0:00:01	5:21:29	5:21:30

Figure 6 Timeline 'SP_2' defining the operation of the three science instruments, the ICS, the PCS, and the CWS to study the fine structure of a penumbral filament.

#2' to be executed by the ICS. It contains the commands for the instrument settings, and two long calibration measurements ('call_2', containing, e.g., dark current measurements, flat fields, stray light target measurements) surrounding the two science observing modes 'SP3' and 'SP8'.

Similar observing blocks of lengths between 2 and 8 hours were compiled for observations of the quiet Sun close to solar disc centre, sunspots, plage regions, emerging flux regions, the poles, active regions, center-to-limb variations, flares, and coronal holes. A six hours long full spectral scan in the so far unexplored near-UV region is a first of its kind. The observing blocks have been prioritized by the SSWG, but the final decision on the order of their execution and the detailed target selection was performed shortly before and during the flight in daily science planning meetings. This allowed to react to the prevailing solar conditions, observatory parameters like solar elevation (important for observations in the UV) or image rotation speed (see Section 3.2.2), and the instrument performance. The so-defined sequence of observing blocks constitutes the timeline, which was executed autonomously by the ICS without requiring commanding from the ground station. However, to optimize telescope and instrument performance, as well as to fine-adjust the pointing to an interesting solar feature, a real-time communication with HK value and thumbnail image transfer to the observatory was available throughout the whole flight (see Section 4.5.4).

All observing blocks were tested on ground with the observatory in flight configuration. The timeline concept also allowed to handle unplanned interruptions to the timeline (e.g. because of a possible instrumental problem or loss of pointing), and a resumption after the problem is solved. At any time, all the instruments could also be operated 'manually', i.e., by direct commands from the GOC through the ICS (see Section 4.5.4). The SUNRISE III Document Database (S3-DocDB) document SR3-MPS-HO-SI000-001 (Smitha and Korpi-Lagg 2024) summarizes all observing blocks, timelines and scientific ideas.

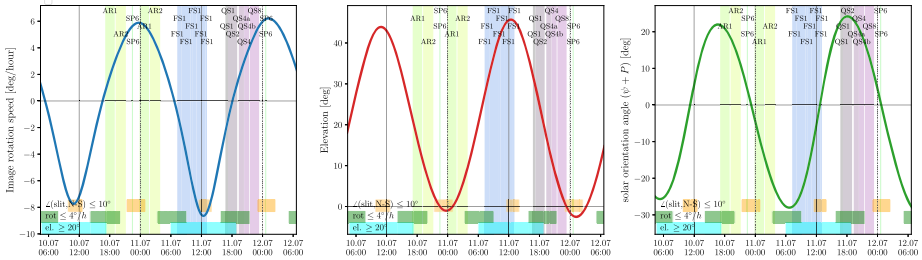


Figure 7 Image rotation speed (*left panel*), telescope elevation angle (*middle*) and slit orientation angle with respect to the solar North-South direction (*right*) for the first 48 hours of the 2024 flight as produced by SPPT (see Section 3.3). The *horizontal bars* at the bottom indicate the periods with high telescope elevation (*cyan bars*), low image rotation speed (*green bars*) and a slit orientation parallel to the solar rotation axis (*orange bars*). The *vertical bars* indicate the observing modes defined in the science planning meeting prior to the launch.

3.2.2. Observational Boundary Conditions

The optimal placement of the timelines and the observing blocks required to take into account not only the current state of the Sun, but also two important observational boundary conditions in the daily science planning meetings: the elevation of the telescope, and the image rotation inherent for alt-azimuth mounted telescopes.

Telescope elevation: Although SUNRISE III floated at an altitude between 33 and 37 km, there was still some residual absorption by the Earth's atmosphere. (SUFI) observations from the first two flights of SUNRISE showed that for low telescope elevations ($\leq 10°$, i.e. around local midnight), the ozone layer affects the sky transparency at the short end of the SUSI wavelength range. The measured variation of the photon flux from lowest (3°) to the highest (42°) elevation by (SUFI) during the SUNRISE I flight was a factor of 2 at a wavelength of 313 nm. At 388 nm, the photon flux did not show any elevation dependence. The start and end times of SUSI observations at the shortest wavelengths therefore need to be scheduled accordingly.

Image rotation: The image rotation speed for SUNRISE III was below $\pm 10°$/h for the 2024 flight trajectory from Kiruna to Canada (see Figure 7). The center of rotation is defined by the lock-point of the CWS, lying within ±15" to the center of the TUMAG FoV. The scan mechanisms of SCIP and SUSI allowed to put the slit of both instruments independently so that the center of the image rotation is on the spectrograph slit for both instruments. This was of special relevance when performing observations in sit and stare mode (i.e., without moving the slit), or when scanning a very narrow FoV in the sub-arcsecond to arcsecond range. Such scans were placed at times when the image rotation is small, in order to maximize the spatial coherence over a large portion of the slit for the whole duration of the time series (typically in the range of 1 hour, see green shaded areas in Figure 7). A small image rotation during such a scan is acceptable, as it results in a 'circular' scan, with spatially coherent information at the slit center, and an increasing FoV towards the slit ends, accompanied with a seamless decrease of the S/N ratio along the slit.

3.2.3. Co-Observations with SUNRISE III

The SSWG invited all major ground-based and space-borne high- or medium-resolution solar observatories to co-observe with SUNRISE III. All contacted leaders of the observatories

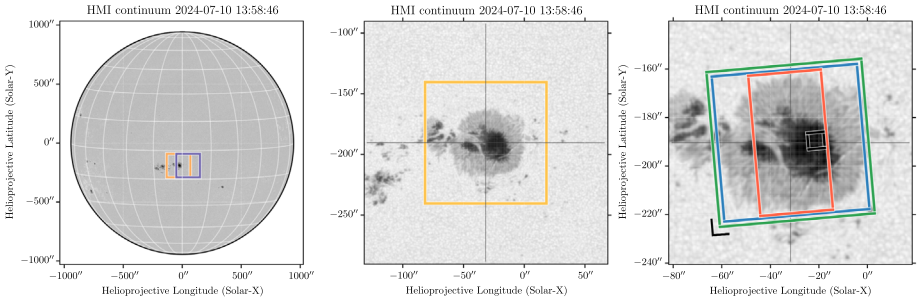


Figure 8 Snapshot from the SPPT observation planning page. The most recent solar images (here SDO/HMI) are used to define the pointing of Sunrise. The tool presents the FoVs of the individual instruments (*green* TUMAG, *red* SCIP, *blue* SUSI, *black* CWS, *right panel*), taking into account the image rotation at the planned start time of the observation. The *orange* and the *blue rectangle* in the *left* panel indicate the location on the Sun at the time of the observation planning and the planned execution time, respectively.

agreed to prepare their facilities for co-observations and run specific observing programs. Of special relevance was the support by the world's largest solar telescope, the National Science Foundation's Daniel K. Inouye Solar Telescope (DKIST: Rimmele et al. 2020), and other large-aperture solar telescopes distributed over the globe: the Goode Solar Telescope (GST, U.S.: Goode et al. 2010; Cao et al. 2010) operating at the Big Bear Solar Observatory (BBSO), GREGOR and German Vacuum Tower Telescope on Tenerife (VTT, Spain: Schmidt et al. 2012; Soltau 1991), the Swedish Solar Telescope with its new adaptive optics (AO) system on La Palma (SST, Spain: Scharmer et al. 2024), the New Vacuum Solar Telescope (NVST, China: Liu et al. 2014), Multi-Application Solar Telescope (MAST, India: Mathew et al. 2017), the Dunn Solar Telescope (DST, U.S.: Zirker 1998), and the Solar Magnetic Activity Research Telescope (SMART: Ueno et al. 2004) at the Hida observatory (Japan). Highly complementary data sets were obtained by the space-based observatories *Hinode* (Kosugi et al. 2007) and Interface Region Imaging Spectrograph (IRIS: De Pontieu et al. 2014), for which a special SUNRISE III/IRIS/*Hinode* Operations Plan (IHOP) was executed during the flight, and by the new full-disk Hα observatory Chinese Hα Solar Explorer (CHASE: Li et al. 2022), and the space-based instruments Solar Ultraviolet Imaging Telescope (SUIT: Varma et al. 2023) on board Aditya-L1 (Seetha and Megala 2017), Solar Ultraviolet Imager (SUVI: Darnel et al. 2022) on board GOES-R, and Solar Upper Transition Region Imager (SUTRI: Bai et al. 2023).

Unfortunately, the Atacama Large Millimeter/sub-millimeter Array (ALMA: Wootten and Thompson 2009; Wedemeyer et al. 2016), which was ready to support the 2022 flight, was not available for the 2024 flight because of the observatory setup not allowing for solar observations. Similarly, no co-observations with Solar Orbiter (Solar Orbiter: Müller et al. 2020) were possible due to the orbital configuration (Solar Orbiter was on the far side of the Sun at the time of the SUNRISE III flight).

The coordination of the co-observation during the flight was based on a website with live-updates on the current and the planned observations of SUNRISE III, including the accurate pointing and timing information and recent images from the Solar Dynamics Observatory (SDO: Pesnell, Thompson, and Chamberlin 2012). Co-pointing of SUNRISE III and the co-observing facilities was based on these images, with overlaid FoVs of the SUNRISE III instruments (see Figure 8).

3.3. The SUNRISE III Science Planning and Pointing Tool (SPPT)

The observational boundary conditions described in Section 3.2.2 require a thorough placement of the pre-defined observing blocks to construct the final timeline. The solar conditions needed to be taken into account in real-time, using the data from multiple solar observatories, most importantly from SDO. The versatility of the SUNRISE III instrumentation and the large number of solar features to be addressed during the relatively short flight (duration: 6.5 days) relied on a sophisticated planning tool, the Python software package SUNRISE III Science Planning and Pointing Tool (SPPT) developed explicitly for the SUNRISE III flight. All information required for the planning is displayed in the context of the SUNRISE III instrumentation (e.g. by showing their FoVs on the real-time images of the Sun, see Figure 8). Observing blocks could be loaded and shuffled around to minimize conflicts of their placement with respect to the observational boundary conditions described in Section 3.2.2. Figure 7 shows an example of the planning for the first observing blocks produced by SPPT after the pre-flight science planning meeting. Conflicts of the individual observing modes with respect to the observational boundary conditions are clearly marked by SPPT, allowing to optimize the placement of the observing blocks in the final timeline.

Additionally, SPPT is equipped with a thumbnail display and analysis tool, showing the real-time images from all SUNRISE III instruments during the flight with the important capability of determining the offset between the different instruments. This enabled to monitor the position of the SCIP and the SUSI slits during the 2024 flight to achieve near-perfect alignment, a unique feature of SUNRISE III allowing to combine full-Stokes spectropolarimetric data in the near-IR and the near-UV. After the planning phase, the tool presented the final timeline of the observations, and fed the current and planned pointing of SUNRISE III to the co-observer website.

4. The SUNRISE III Observatory

The SUNRISE III observatory is the payload of a NASA/CSBF operated long-distance balloon (LDB) flight from Esrange (Sweden) to Canada. It is suspended from a 34.43 million cubic feet (975,000 m^3) Helium balloon and flight train, the latter consisting of a parachute and the so-called ladder, a set of steel cables connected on one end to the parachute and on the other end via a spreader plate to the gondola suspension point. The design of the SUNRISE III observatory is shown in Figure 9, and some key parameters are listed in Table 1. It is composed of four major building blocks, as illustrated in Figure 10:

(i) The heart of the observatory is the telescope with its light-weighted Zerodur® mirror with a diameter of 1 m in a Gregory configuration and an altitude-azimuth mounting (see Section 4.2). The altitude (or elevation) is controlled by a motor acting on the horizontal axis of the telescope perpendicular to its optical axis, while the azimuth pointing is achieved by rotating the whole gondola (see Section 4.1). Attached to the telescope are the Sun Guider Telescope (SGT) (see Section 4.2.1) and the Inertial Measurement Unit (IMU) (see Section 4.2.2). Feedback from these devices is used to determine the drive signals for the elevation, azimuth, and roll motors.

(ii) The Post Focus Instrumentation (PFI, see Section 4.3) is the box housing the Image Stabilization and Light Distribution unit (ISLID) with the CWS (Section 4.3.1 and Section 4.3.2), and the three science instruments SUSI (Section 4.4.1), TUMAG (Section 4.4.2) and SCIP (Section 4.4.3). It also contains the ISLID controller and mechanism (the F2 filter wheel) and the Main Telescope Controller (MTC).

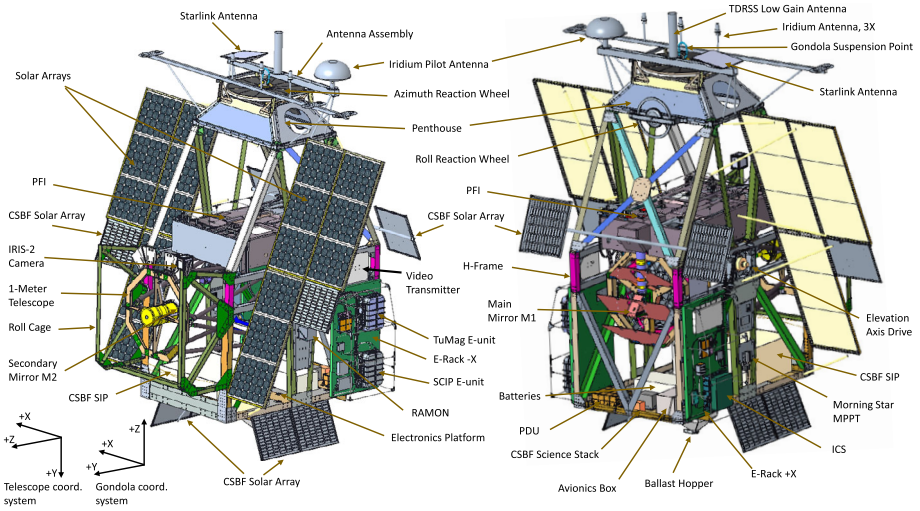


Figure 9 Design drawing of the SUNRISE III observatory. The telescope is located in the middle of the gondola and is oriented horizontally in the plotted configuration. The *gray-purple box* on top of the telescope is the Post Focus Instrumentation (PFI) platform housing the science instruments. Instrument control electronics are housed on two panels on the lower back part of the gondola. The gondola control and power electronics units, as well as the CSBF Support Instrumentation Package (SIP) are housed on the bottom electronics platform. The *lower left corner* of the figure shows the two separate coordinate systems used by the telescope and instruments (*on the left*) and the gondola (*on the right*). The telescope coordinate system rotates about the x-axis relative to the gondola one depending on its elevation angle.

Table 1 SUNRISE III key parameters.

Parameter	Description
Flight details	Launch: 10 July 2024, Esrange (Sweden); 6.5 day uninterrupted solar observations; stratospheric 33 – 37 km float altitude; landing: west of Great Bear Lake, Canada. NASA/CSBF LDB 34.43 million cubic feet Helium balloon ($\approx$ 975,000 m^3).
Mass	Science payload: 828 kg; gondola: 1269 kg; CSBF equipment: 275 kg; equipment above / below pin: 442 kg / 103 kg; ballast: 272 kg; balloon film: 2330 kg; required Helium mass (10% lift) $\approx$ 1065 kg.
Dimensions	Gondola: height (without ballast, solar panels): 523 cm; width without solar panels: 196 cm, with solar panels: 540 cm; length (including roll cage): 419 cm. Flight train: suspension ladder: 22.5 m; parachute length: 73 m (diameter: 48.5 m); balloon size at float altitude: 'pumpkin' shape, width 134 m, height 103 m.
Power	Solar panels with 1.8 kW peak power, buffered by 4 lead batteries (1728 Wh). Max. power consumption during ascent: 1031 W, at float altitude (science): $\approx$ 750 W.
Key features	Gregory-type telescope with 1-meter main mirror, 24.2 m focal length. Pointing stability: $<$ 3" rms (gondola); $\leq$ 0.005" rms (internal image stabilization).
Science	3 scientific instruments; wavelength 309 – 855 nm; full Stokes spectropolarimetry; diffraction-limited spatial resolution: 57 km (@309 nm) to 154 km (@855 nm).
Data	On-board data storage: approx. 240 TByte net storage on 48 SSDs.
Communication	In-flight communication via satellite (max. 8 Mbit/s); LoS downlink-only during ascent and first hours of flight (12.5 Mbit/s).

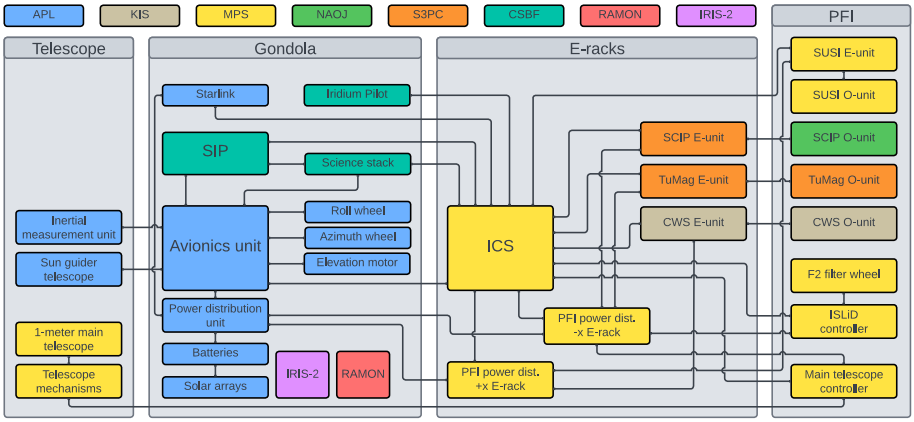


Figure 10 Schematic illustrating the four major building blocks of the SUNRISE III instruments and infrastructures. The *coloring* indicates the responsible institute or team.

(iii) The gondola provides the housing for all components of the observatory and connects the observatory to the flight train with the parachute and the balloon (see Section 4.1). It acts as a protection from the shocks during launch, flight termination, parachute inflation, and finally the landing. During the flight, the gondola provides power to the entire observatory and the stable pointing that allows the scientific instruments to obtain several hours of uninterrupted observations of specific targets on the Sun. Finally, it also contains the hardware responsible for the communication with the ground station.

(iv) The electronic racks (E-racks) are mounted on the $+x$ and $-x$ side of the gondola (see gondola coordinate system in Figure 9). They provide the platform for the electronic units (see Section 4.5), which control all subsystems of the observatory. The central unit is the Instrument Control System (ICS), responsible for executing the commands from the ground station, running a coordinated observation timeline for all instruments by sending commands to their individual electronic units, and for reporting HK values and thumbnail data to the ground station.

4.1. Gondola

The SUNRISE III gondola structure provides the stable platform enabling the precision telescope pointing towards the Sun, and keeps the scientific instrumentation safe during launch and landing. Photovoltaic arrays generate the required power for the electronics and keep the system's batteries fully charged during science operations. The two previous flights of SUNRISE have proven that maintaining a constant pointing and tracking of the Sun for extended periods of more than a few hours is a very challenging task due to pendulum motion of the gondola and occasional wind shear which introduced significant disturbances, even in the stratosphere. The Johns Hopkins University Applied Physics Laboratory (APL) provided a new gondola for SUNRISE III featuring a state-of-the-art attitude control system (see Figure 9 and Brian Alvarez et al. 2023), that during the 2024 6.5 days of flight provided precise and nearly uninterrupted stable and constant pointing at the Sun.

4.1.1. Structure

The gondola structure has three main assemblies. The uppermost section, called the penthouse, supports the Momentum Transfer Unit (MTU), azimuth reaction wheel, roll wheel and azimuth and roll control electronics. It is a truncated pyramid structure constructed with a machined aluminum top plate, shear panels and edge support members. The middle section, called the H-Frame, supports the two elevation gimbals assemblies, the elevation drive motor, elevation hard stops, elevation brake, roll cage, and the elevation control electronics. It is primarily constructed with aluminum tubes that are interconnected with machined aluminum fittings and gusset brackets. The elevation gimbals support the telescope and allow it to smoothly rotate in elevation. The lower section is the electronics deck which houses the gondola control computers (avionics), Power Distribution Unit (PDU), batteries, Support Instrumentation Package (SIP), and ballast hopper. This section is primarily constructed with aluminum tubes, aluminum angles, aluminum sheet metal and aluminum gussets. The three sections are connected to each other using aluminum angle beams. All structural part connections are mated using high strength bolts. The entire gondola frame is painted white to maintain it thermally stable. Exterior to the primary structure are the photovoltaic arrays and roll cage. The photovoltaic array support structure is a welded and bolted aluminum assembly that is bolted to the gondola structure. The roll cage is a bolted aluminum assembly that protects the telescope should the gondola roll over upon landing, which happened at the end of the 2024 flight.

The gondola structure is designed to support the loads as described in Balloon Program Office (BPO) structural requirements document 820-PG-8700.0.1a (Hamilton 2024). The gondola must show a positive margin of safety for both yield and ultimate strength of ductile metallic materials when oriented vertically at 8 g (gravitational force), oriented 45° at 4 g, and oriented horizontally at 4 g. The loads are applied at the balloon flight train attachment point on the MTU. Design factors of safety are 1.25 for yield strength and 1.4 for ultimate strength. The method to perform the analysis uses inertia relief. An additional load case was analyzed that was not documented in 820-PG-8700.0.1a. A high rotational load case that can occur at launch was analyzed as a result of a lesson learned from a failure experienced during a first launch attempt of SUNRISE III in 2022. This rotational load caused a shear failure for the bolts securing the elevation drive to the brake mechanism. The analysis was performed at twice the measured angular acceleration of 190° s^{-2} and resulted in design updates to many of the brake parts. The launch in July 2024 likely exerted even larger rotational loads than in 2022, nevertheless the brake structure operated flawlessly. The gondola structure was finite element modeled (FEM) using NASTRAN. The structure FEM contains 97,000 plate elements and 101,000 nodes. The bolts stresses were analyzed for axial and shear loads using loads from the NASTRAN analysis. All structural parts meet the requirements in 820-PG-8700.0.1a.

4.1.2. Pointing Control System (PCS)

The attitude control system is colloquially referred to as the Pointing Control System (PCS). The gondola utilizes elevation-azimuth actuation (often called altitude-azimuth or alt-az mount) to point the telescope (see Figure 11, left) at the Sun. Telescope elevation is controlled using a direct-drive torque motor on the elevation axis. Azimuthal control is more complicated. It is accomplished by rotating the entire gondola about its vertical axis by means of a complex mechanism called the MTU. The MTU provides also the attachment point from the gondola to the flight train/balloon. Thus it must accommodate three rotating



Figure 11 SUNRISE III during the first-light hang test on 01 May 2024 at Esrange, illustrating the gondola Pointing Control System (PCS): The elevation-azimuth actuation, and the roll wheel compensation. The *right image* shows the location of the Sun Guider Telescope (SGT).

elements about the vertical, azimuth, axis: the gondola, the azimuth reaction wheel, and the suspension connection to the balloon flight train. Each of these elements is free to rotate in its own direction and speed independently of the other two. To control gondola azimuth, the gondola is torqued against the azimuth reaction wheel, and in turn, the azimuth reaction wheel sheds its momentum into the balloon flight train.

If the gondola were to remain perfectly leveled during flight, elevation-azimuth actuation control alone would be sufficient for providing the necessary stability for telescope pointing. However, as the gondola is suspended from a floating balloon, it is subject to several modes of pendulum motion. When this motion is front-to-back (or vice versa) with respect to the gondola (pitch), the elevation drive (with the inherent assistance of the telescope's inertia) is enough to compensate for the motion. When this motion causes side-to-side movements (roll), the azimuth drive must compensate, but it is only able to do so slowly due to the gondola's inertia. This slow correction leads to undesirable pointing errors that manifest in a side-to-side oscillation of the images. This effect is stronger when pointing the telescope at high elevation angles as the azimuth correction is less effective. To combat this, the PCS utilizes another motor driven reaction wheel mounted along the gondola's roll axis. This is the roll reaction wheel that is seen as one component in Figure 9. This wheel is able to dampen frequency modes greater than 0.5 Hz of side-to-side gondola motion allowing the gondola to continue pointing the telescope with high-stability even with pendulum induced movements and disturbances during flight.

To acquire the Sun in flight, the PCS takes a methodical approach. First, the telescope's elevation is driven to match that of the Sun's. The telescope's elevation is verified utilizing a rotational encoder (also called a goniometer) on the elevation drive and knowing that the gondola always hangs close to vertical from the balloon. Once the telescope is at the proper

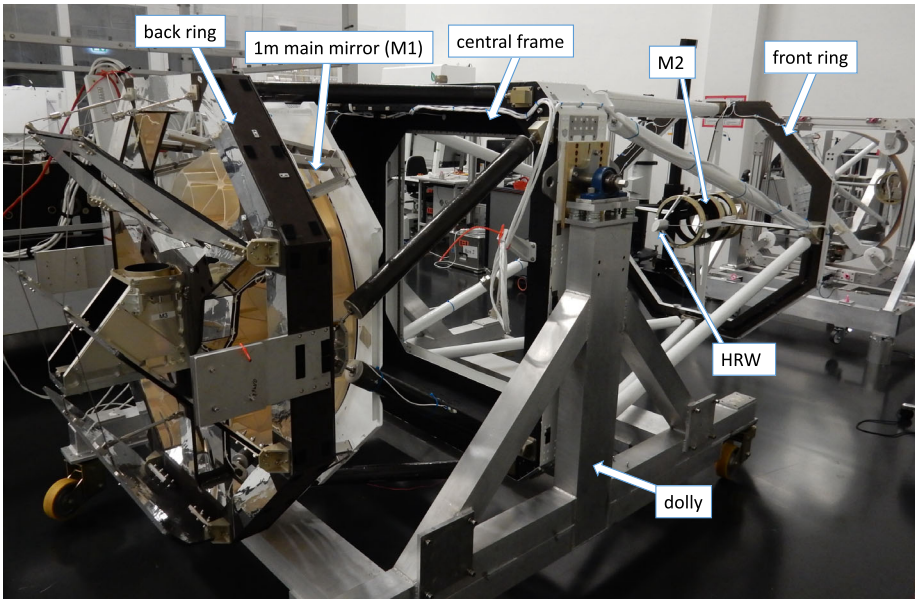


Figure 12 SUNRISE III telescope during alignment in the ISO-8 cleanroom at MPS. The 1-m primary mirror is on the left and can be recognized by the brownish honeycomb structure, the central frame houses the aperture door (open in this image) and the spider to the right holds the HRW at the primary focus of the telescope and the secondary mirror. The dolly is used for alignment and transport and is a non-flight item.

elevation, the PCS uses feedback from the IMU to rotate the gondola azimuthally in a circle at a rate of approximately 1° per second. The SGT is equipped with wide-angle sun sensors that have a field of view of roughly $\pm 15°$. When the gondola's slow rotation puts enough light onto these sun sensors, they provide the feedback for the PCS to roughly center the telescope on the Sun, which allows for the higher precision pointing of the SGT quad-cell to takeover (see Section 4.2.1).

The PCS was tested on the ground by suspending the gondola, including telescope and PFI, from a crane (outside the 'Ballonhalle' at MPS, and the 'Dome' at Esrange, see Figure 11) and by pointing at the Sun. These tests demonstrated its stability and tested its limits in dealing with wind and cloud based disturbances.

Excellent performance of the PCS was achieved during the 2024 flight. The pointing worked accurately and stably throughout the whole flight, with only one major pointing loss on the last observing day due to an unexpected avionics computer reboot. A detailed analysis of the pointing performance will be provided after completion of the data reduction phase (see Section 6.3).

4.2. Telescope

The SUNRISE telescope (see Figure 12) is a light-weight Gregory-type reflector with an aperture of 1000 mm, 324 mm central obscuration and 24.2 m effective focal length originally manufactured by Kayser-Threde in Munich in close collaboration with MPS. Eight struts arranged in triangles form its Serrurier structure, which is connected to the central frame, made of riveted sheet steel. Front and rear rings as well as connecting struts are made of carbon-fiber-based composite materials for high stiffness and low thermal expansion.

The parabolic main mirror (made from Zerodur® by SCHOTT AG in Mainz, Germany) was realised as an extremely light-weight structure, fine-ground and polished by Safran Reosc (formerly Sagem) in France. At the primary focus, the Heat Rejection Wedge (HRW) acts as a field stop with a central hole defining the usable FoV of 3.4', corresponding to about 150 Mm on the solar surface. Approximately 1 kW of solar radiation hits the field stop, of which 99% are removed mostly by reflection (85%) and partially by absorption, such that only 10 W enter the science instrumentation. Dedicated radiators connected by ammonia heat pipes prevent overheating of the HRW.

The telescope of SUNRISE III is almost identical to the one flown in 2009 and 2013 with only minor modifications (for a detailed description of the SUNRISE I telescope see Barthol et al. 2011). The secondary mirror was already replaced for the 2013 flight, due to damage during the 2009 landing. New M3 and M4 mirrors (plane folding mirrors towards the PFI) have been manufactured by the Korea Basic Science Institute (KBSI) prior to the 2022 flight. Damaged parts of the carbon fiber structure were re-manufactured or replaced by spare parts. All mirrors (M1, M2, M3, M4) have been re-coated at the Calar Alto Astronomical Observatory (Spain) in November 2023 with 120 nm bare aluminum without protection layer.

The HRW and its thermal subsystem were rebuilt. In contrast to the 2009 and 2013 flights, the surface of the primary focus field stop was diamond milled on the aluminum bulk by IMTEK (Department of Microsystems Engineering, University of Freiburg, Germany), avoiding the fragile second surface mirror (SSM), which was used before. A slightly higher absorptivity was accepted in favor of a reduced risk of failure. The thermal insulation of the telescope was adapted to the new gondola geometry.

The highest optical performance throughout the flight is achieved by the semi-active control system of the SUNRISE telescope. A wavefront sensor located in the post-focus instrumentation constantly monitors the alignment status, generating control signals for mirror re-positioning. The M2 lateral and axial position can be fine-tuned to ensure the correct relative M1/M2 alignment for all telescope elevations and the expected thermal loads. While the lateral position is manually optimized (by minimizing coma), axial position (focus) is automatically corrected in closed loop (see Section 4.3.2).

4.2.1. Sun Guider Telescope (SGT)

The Sun Guider Telescope (see Figure 11, right image) is the main source of feedback for the gondola PCS when it is tracking the Sun. The SGT has two sets of sensors for pointing: the intermediate sun sensors and the quad-cell photodiode. The intermediate sun sensors have a FoV of approximately $\pm 15°$ and are mounted in an azimuth/elevation configuration. They are used to coarsely align with the Sun, and are only used up until the point at which enough sunlight enters the SGT's aperture and hits the quad-cell photodiode. The optics of the SGT result in a 1 cm image of the Sun landing on the 14 mm diameter quad-cell. Mounted on the center of the quad-cell is a circular occulting disk, which prevents the sensor from saturating and makes it more sensitive to pointing errors. Once sufficient sunlight hits the quad-cell, the PCS works to keep the image of the Sun perfectly centered on the sensor. The quad-cell photodiode is mounted on an adjustable X-Y Stage, the movement of which causes an intentional misalignment between the SGT and the main telescope. This enables to accurately aim the main telescope at any location on the solar disk, including the limb, while the PCS constantly points the SGT at Sun center.

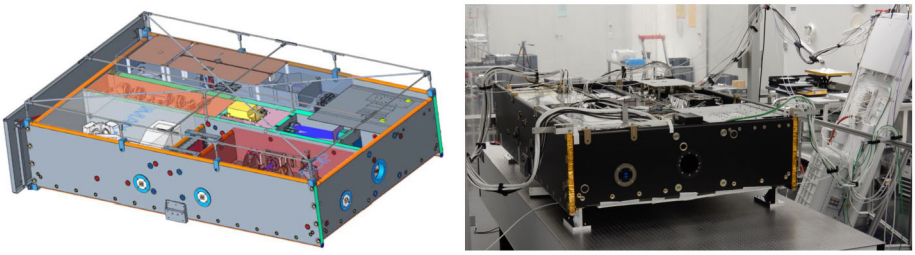


Figure 13 CAD model of the SUNRISE III PFI (*left*) and the flight-version of the PFI under the clean tent in the MPS clean room (*right*).

4.2.2. Inertial Measurement Unit (IMU)

A KVH 1725 IMU is mounted next to the SGT. It features three single-axis interferometric fiber optic gyroscopes as well as three single-axis accelerometers resulting in a six-degree of freedom inertial sensor. When tracking the Sun, the PCS uses IMU readings to dampen the gondola's roll movement. When first acquiring the Sun, the IMU readings are used to control the 1° per second azimuth spin.

4.3. Post Focus Instrumentation (PFI) Platform

The SUNRISE III PFI (see Figure 13) is mounted on top of the telescope, and houses the four instrument modules with their proximity electronics. The compact and lightweight bookshelf-like structure of the PFI is made from Carbon-fibre honeycomb elements and provides a stable platform for both, the scientific instruments, the image stabilizer and the light distribution optics. It also contains the ISLID controllers responsible of commanding the ISLID filter wheel in F2, and of the temperature control during the ascent and flight phases, as well as the MTC. On top of its surface, the individual radiators of the instruments are located for maximum cooling efficiency of cameras and electronics.

To achieve its science goals, SUNRISE III requires instruments that are capable of measuring with high precision the full polarization state of sunlight at a spatial resolution close to the diffraction limit of the 1-meter telescope and at a spectral resolution allowing to gain a maximum of information from the spectral lines. The basis for this lies in the Image Stabilization and Light Distribution unit (ISLID) and the Correlating Wavefront Sensor (CWS), described in the following two subsections.

4.3.1. Image Stabilization and Light Distribution Unit (ISLID)

ISLID is the central optical interface unit between the telescope and the scientific instruments. It also contains the fast tip/tilt mirror, which acts as image motion compensator, and which is controlled in closed loop by the CWS. The second important task of ISLID is to separate the wavelength bands in a photon efficient manner, such that each instrument gets the maximum available photon flux in its working wavelength range.

The design of the light distribution system of SUNRISE I and II was driven by the need to observe below 250 nm, and it was consequently tailored to this purpose (see Gandorfer et al. 2011). For SUNRISE III, we could concentrate on wavelengths above 300 nm, which greatly reduces the complexity of the system.

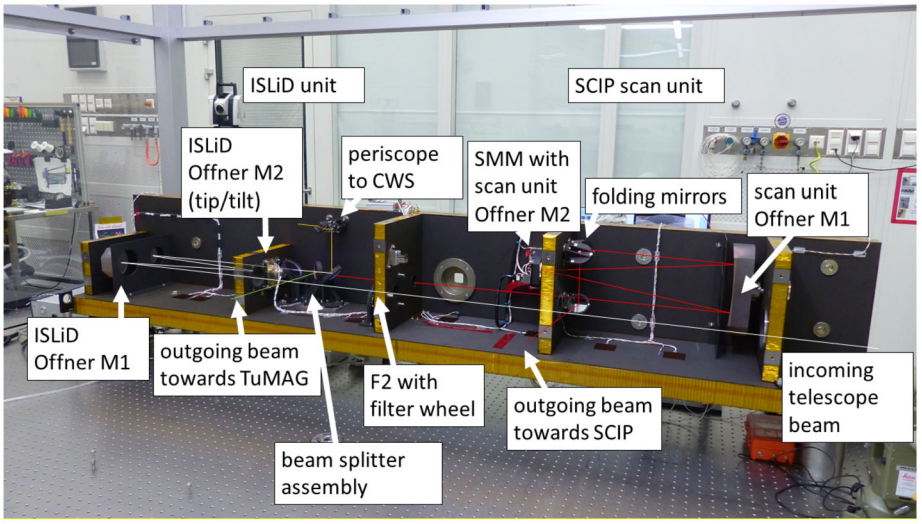


Figure 14 The ISLiD system during assembly, before the left-hand side stiffening wall is mounted. The optical paths within the ISLiD system including the SCIP scan unit are illustrated by *thin colored lines* (*white* means panchromatic, *green* symbolises the wavelength band sent to TuMag, *orange* for CWS, *red* goes to SCIP. The *blue part* is not visible in this picture, since it is sent to the other side of the vertical bench, see Figure 15). Major subunits are labeled.

The new ISLiD is a 1:1 optical relay, which means that each instrument can be built in such a way as it would be directly fed by the F#24.2 telescope beam. The optical arrangement (see Figure 14) is based on an Offner relay, consisting of two spherical mirrors (Offner-M1 and Offner-M2), sharing a common center of curvature (Offner 1973). Their radii of curvature have a ratio of 2:1. Such a system is per design free from spherical aberration, astigmatism and coma. The common center of curvature is positioned in the geometrical center of the PFI, minimizing any negative impact of (thermo-)elastic bending of the PFI structure to optical misalignment of ISLiD. The reflection geometry is chosen such that the three reflections (M1 – M2 – M1) compensate the polarimetric behaviour of the telescope mirrors M3 and M4 to a great extent. The Offner-M1 focal length is chosen such that it forms a real image of the telescope pupil on the Offner-M2 mirror, which can thus be used as a fast tip/tilt mirror for image motion compensation. It is mounted on a piezo actuator, which receives its control signal in closed loop by the CWS (see Section 4.3.2). The Offner M1 and M2 mirrors of ISLiD were manufactured by KBSI.

The light distribution and wavelength separation is achieved by 4 plane-parallel beam splitter plates, arranged in two pairs of anti-parallel orientation, such that the transmitted beam is free from any astigmatism and lateral chromatic aberration (see Figure 15). They all reflect the light by 90° in the following order: The first beam splitter plate reflects all wavelengths below 450 nm towards the SUSI instrument. The second plate compensates the astigmatism introduced by the oblique transmission through the first plate. The transmitted beam is therefore free of astigmatism, but shows chromatic lateral aberration. The third plate reflects 500 – 550 nm towards TuMag, which is from a technical point of view monochromatic and thus insensitive to the chromatic error. The fourth plate compensates the astigmatism introduced by the oblique transmission through the TuMag beam splitter and reflects 590 – 650 nm to the CWS. The CWS path is equipped with a narrowband filter, which is used as the astigmatism corrector for the uncompensated transmission through

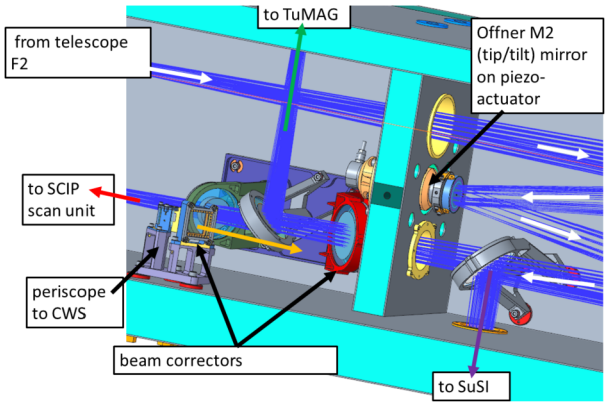


Figure 15 Central part of the ISLiD system, showing the Offner-M2 (tip/tilt) mirror on its piezo stage, and the beam splitter arrangement. *White arrows* mark the panchromatic beam from the telescope. The *colored arrows* indicate the wavelength bands sent towards the exit foci. *Black arrows* denote mechanical or optical devices.

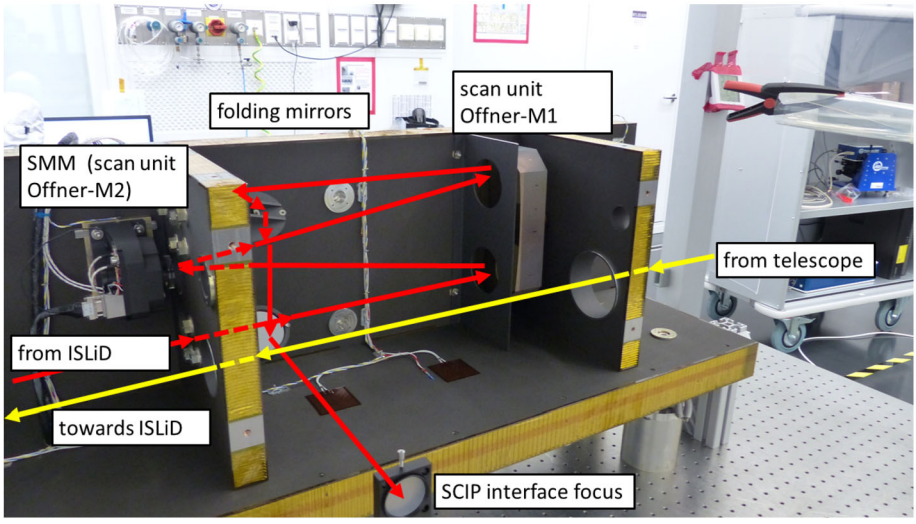


Figure 16 SCIP scan unit during assembly. The *red arrows* symbolize the light path from ISLiD towards the SCIP interface focus. The Offner relay uses the SMM as its secondary mirror. A set of three folding mirrors (only two are visible here) acts as path length compensator and is used to bring the exit focus and exit pupil to the desired positions, respectively.

plate 3. The transmitted beam through all plates is free from any chromatic lateral aberration and astigmatism and forms the interface focus to the SCIP scan unit.

This scan unit for the SCIP instrument contains the scan mirror mechanism (SMM, Oba et al. 2022) and is incorporated as a part of the ISLiD arrangement (see Figure 16). It consists of a second Offner relay, which is identical to the one in the ISLiD system, but rotated by 90° around the line-of-sight (LoS). In between the two systems, a field stop is located, which minimizes false light contamination towards SCIP. The mirrors of the SCIP scan unit (first mirror fabricated by KBSI and secondary mirror on SMM fabricated by Natsume Optical Corp.) are gold coated, making the system insensitive to back reflections of the TuMAG prefilters and protecting TuMAG against potential back-reflections of residual green light from the SCIP polarization modulator. Both Offner systems are equipped with a carefully designed set of vanes, in order to prevent any sneak paths.

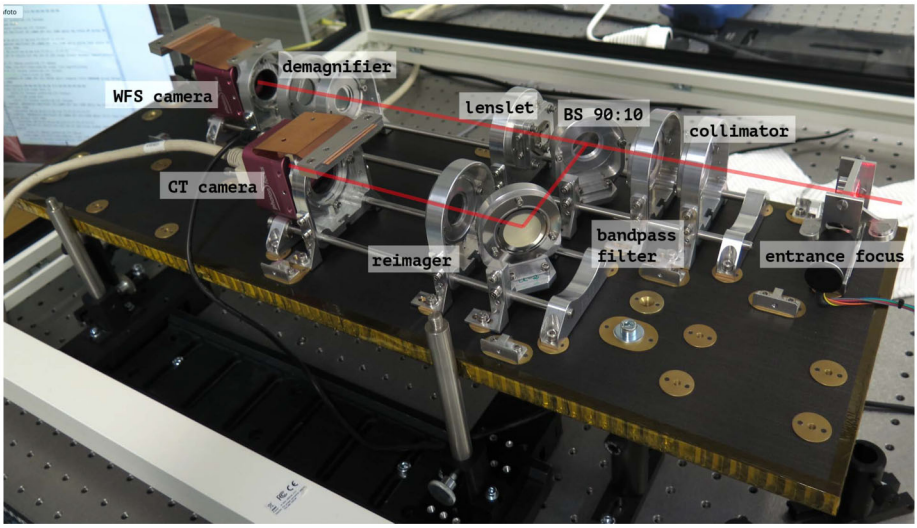


Figure 17 Optics Unit of the CWS. The light enters the CWS at the entrance focus on the right.

At the F2 focus, the entrance of ISLiD, a filter wheel is located with 8 positions (see Section 5.2). A field stop with a diameter of 180", and a shutter for common dark exposures. The 6 remaining positions carry alignment and test targets, which can be used by all instruments in flight for calibration purposes. The filter wheel is based on piezo-technology and has been manufactured for MPS by SmarAct in Germany.

A first glimpse of the excellent optical performance of telescope and ISLiD could already be obtained during the 2024 flight: all three science instruments transmitted near real-time full-resolution thumbnail images via satellite communication of superb quality. A detailed assessment of the image quality will only be possible after the data reduction phase (see Section 6.3).

4.3.2. Correlating Wavefront Sensor (CWS)

The CWS provides high-frequency precision image stabilization and autofocus. In contrast to SUNRISE I and II, where the CWS had a six-element Shack-Hartmann wavefront sensor (WFS) for fast tip-tilt correction, slow autofocus and coma measurement, SUNRISE III uses the WFS only for the slow autofocus and coma measurement and adds a correlation tracker (CT) for the fast tip-tilt-correction. This has the advantage of an improved tip-tilt measurement accuracy by using diffraction limited sampling of the full aperture resolution and a much faster readout of the CT camera which results in an increased correction bandwidth. The fast tip-tilt correction is done by the tip-tilt mirror (Offner-M2), the slow autofocus by positioning the secondary mirror M2 in the z-direction (see Figure 9, telescope coordinate system). Figure 17 shows the optics of the CWS during final testing before integration into ISLiD, Table 2 lists its parameters.

Tests have shown a 0 db correction bandwidth of 130 Hz and 160 Hz for tip and tilt correction, respectively. The tip-tilt measurement accuracy is of the order of 1 milli-arcsecond rms per axis for a typical granulation contrast at the operating wavelength of 640 nm. The focus and coma measurement accuracy is better than $\lambda/100$ (≈ 6 nm rms) per mode. The tip-tilt axes can be moved in steps of 1 milli-arcsecond over the full range of 60".

Table 2 Parameters of the WFS and CT inside the optics unit of the CWS.

	WFS	CT
# of subapertures (total)	6	1
measured aberrations	tip-tilt, focus, coma	tip-tilt
pupil size on sky [m]	0.33	1
FoV on sky [arcsec]	13	6.7
pixel scale [arcsec/pix]	0.2	0.07
# of pixels used for cross-correlation	64×64	96×96
camera (manufacturer Photonfocus)	MV1-D1024E-80-G2	MV1-D1024E-160-CL
typical framerate [Hz]	500	7000

The CWS electronic unit consists of a fast conduction-cooled 4-core compute board, 16-bit digital-to-analog conversion, two 100 V voltage amplifier channels for the fast tip-tilt mirror and additional DC-DC converters and components such as temperature sensors or the motor controller for the CWS entrance focus unit. All electronics (including the two cameras of the CWS optics unit) have been modified and thermally vacuum tested to ensure operation at millibar pressure levels without requiring a pressurized box. The consumed power, i.e., the resulting heat load of typically 60 W in total, is conducted away by heat straps attached to external radiation shields and radiated into space.

A more detailed description of the CWS can be found in Berkefeld et al. (2025). A preliminary assessment of the 2024 flight performance of the CWS confirmed excellent stability, enabling SUNRISE III to obtain a record-long time series of more than four hours without a single loss of the lock point, and to stably lock on a faculae region for limb observations.

4.4. Scientific Instruments

Three scientific instruments analyze the light provided by the telescope and ISLiD, stabilized to milli-arcsecond accuracy by the CWS. The instruments are highly complementary and make use of the unique possibility of observing spectral lines from the near-UV to the near-IR simultaneously, without suffering from the effects of seeing and the displacement introduced by the refraction in the Earth's atmosphere. All three instruments are measuring the full polarimetric information of the light (Stokes I, Q, U, V) and are optimized for photon efficiency to achieve the maximum possible S/N, important for the accurate determination of the magnetic field vector. The instruments deliver images and spectra at the diffraction limit of the telescope at high spectral resolution.

Table 3 summarizes the most important specifications for the three instruments. The first three rows are self-explanatory (spectral range, optical scheme, and science targets). The fourth row describes the FoV: For the two slit-spectrographs, SCIP and SUSI, with one spatial and one spectral dimension, a 2D-spatial FoV is achieved by scanning, i.e., moving the slit over the solar image. This is done in a step-like fashion for SCIP, and in a continuous way by SUSI (see Section 6.2), with the scanning range depending on the observing mode, but always lying within the 2D-FoV of TuMag.

The fifth row in Table 3 specifies the maximum temporal resolution of the instruments. For the slit spectropolarimeters, it is derived from the time required to record the spectrum for one slit position. In intensity mode, this is determined by the frame rate of the cameras, and in full-Stokes polarimetric mode, the time it takes to record a full modulation cycle. For

Table 3 Main specifications of the scientific post-focus instruments.

	SUSI	SCIP	TuMag
Spectral range	309 – 417 nm	765 – 855 nm	517 – 525 nm
Optical scheme	Modified Czerny-Turner spectrograph with tunable low-order grating; slit scan unit and slit-jaw imager	Littrow spectrograph with fixed high-order echelle grating; slit scan unit and slit-jaw imager	Collimated double-pass Fabry-Pérot filtergraph
Scientific target, wavelength bands	Spectrograph: many-line magnetic field diagnostics over entire spectral range Slit-jaw imager: 325 nm continuum (lower photosphere)	Photosphere: Fe I 846.8 & 851.4 nm Upper photosphere: K I 766.5 & 769.9 nm Chromosphere: Ca II 849.8 & 854.2 nm Slit-jaw imager: 770.5 nm continuum	Photosphere: Fe I 525.02 & 525.06 nm Temperature minimum: Mg I 517.3 nm
FoV	59”×(17 – 27) Å	58”×(61 – 83) Å	63” × 63”
Spatial sampling	0.03”/px	0.094”/px	0.037”/px
Resolution on Sun	56 – 76 km	138 – 154 km	92 km
Spectral sampling	(8.5 – 13.5) mÅ/px	(39 – 42) mÅ/px	66 mÅ spec. bandwidth
Time resolution: full-Stokes intensity-only	 4 fps 47 fps	 1 fps 16 fps	 29.07 s for 8 WL-pos 23.74 s for 15 WL-pos
Pol. sensitivity	$< 1 \cdot 10^{-3}$	$< 1 \cdot 10^{-3}$	$< 1 \cdot 10^{-3}$
Max. data rate	600 MByte/s	100 MByte/s	100 MByte/s

SUSI, all frames were stored on disk and the data are available for scientific analysis at these high frame rates. However, to achieve a polarimetric sensitivity of 10^{-3} (see row number six), at least 5 s accumulation time is needed, strongly dependent on the selected wavelength and observed solar feature. SCIP followed an on-board accumulation strategy. Depending on the observing mode, frames are accumulated over 1024, 5120, or 10,240 ms in full-Stokes mode, or 64 ms in intensity-only mode. SCIP reaches a polarimetric sensitivity of $3 \cdot 10^{-4}$ after an integration time of less than 10 s. The temporal resolution of TuMag given in the sixth row of Table 3 refers to the time required to acquire a complete single spectral line scan in full-Stokes mode and intensity-only mode, respectively. This time is about doubled when scanning both TuMag spectral lines.

4.4.1. Sunrise UV Spectropolarimeter and Imager (SUSI)

The SUSI spectropolarimeter has been designed, developed and built by MPS, with contributions from NAOJ. It observes the near-UV wavelength range between 309 nm and 417 nm. Compared to the visible or the near-IR, this spectral domain exhibits a much larger density of spectral lines, formed in different layers of the solar photosphere and chromosphere (see Figure 5). Due to the short wavelengths, SUSI is the Sunrise III instrument offering the highest spatial resolution of about 60 km on the Sun. The combined effect of the high spatial resolution and the large number of lines leads to a significant improvement in the detectability of small-scale magnetic structures and their height dependence. In order to meet these specifications, SUSI relies on a number of technical innovations.

The opto-mechanical layout of SUSI is shown in Figure 18. To measure the polarization of light, the polarization information is converted into a periodic intensity modulation

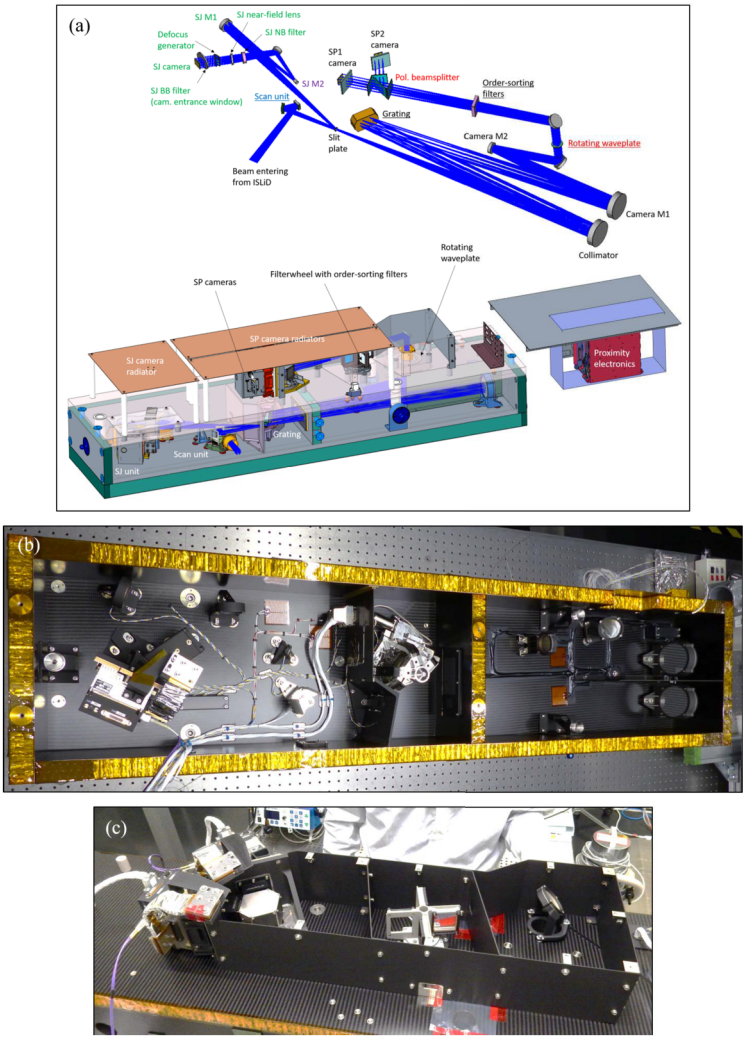


Figure 18 Layout of SUSI. Panel (a), *top*: basic optical layout; the components of the main functional units are labeled in different colors: scan unit (*sky blue*), spectrograph (*black*), polarization modulator (*red*) and slit-jaw unit (*green*); *underlined labels* denote a moving component involving a mechanism. Ray paths are marked in *navy blue*. Panel (a), *bottom*: Opto-mechanical layout with structural elements, radiators and proximity electronics. Panels (b, c): Lower and upper levels of SUSI, during integration in the MPS cleanroom.

and then demodulated with synchronized detectors. In SUSI, the polarization modulation is accomplished by a rotating waveplate. In order to meet the challenging polarimetric accuracy requirements, the rotating mechanism of this Polarization Modulation Unit (PMU) is designed for a very high rotation uniformity (deviations less than 0.3%, Kubo et al. 2020). The details of the polarimetric calibration of SUSI are described in Iglesias et al. (2025).

The three SUSI cameras operate at a framerate of 47.040 fps in synchronization with the PMU. This implies that each modulation cycle (half PMU rotation lasting 256 ms) is sampled by 12 frames of the spectrograph cameras. During pre-flight tests, the synchronization

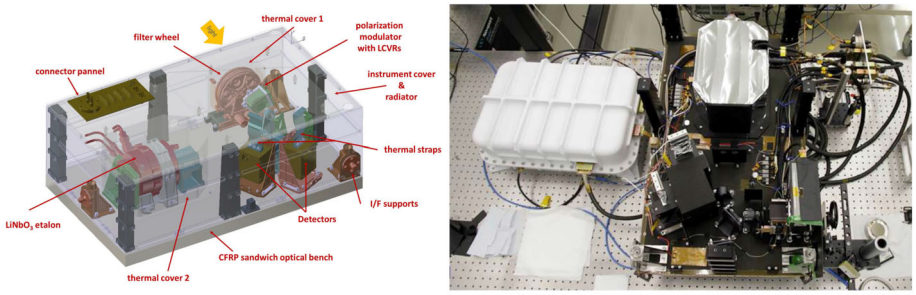


Figure 19 Opto-mechanical design of the TuMag instrument (*left*), and flight instrument before closing the housing, including the electronic unit in its white housing (*right*).

error between cameras and PMU was measured to be below 0.36 ms, and the residual image motion due to PMU misalignment (beam wobbling) was below the required 0.1 pixels rms.

The SUSI spectrograph is equipped with two cameras in a dual-beam polarimetric configuration which allows suppressing measurement errors originating from residual jitter. The cameras, developed at MPS, meet the harsh environmental requirements of a stratospheric balloon flight and are based on UV optimized image sensors with very low noise (2 e^- rms) to allow for efficient measurements in the deep, heavily photon-starved UV spectral lines. The data are recorded at a high frame rate of 47 frames per second (fps) to make them insensitive to residual large amplitude slow jitter of the system. All individual frames are stored on-board. This greatly enhances our flexibility in the later data reduction, in particular in terms of trading spatial and temporal resolution against signal-to-noise, depending on the actual science question.

High spatial resolution context images are obtained by re-imaging the 2D solar scene around the linear spectrograph entrance slit onto a separate camera. This setup is known as slit-jaw imaging. The slit-jaw imager, which is strictly synchronized to the two spectrograph cameras, detects residual jitter and optical wavefront errors. It allows for a post-facto numerical image restoration of the spectrograph scans following the technique developed by van Noort (2017) that has impressively stood the test in recent ground-based observations.

4.4.2. Tunable Magnetograph (TuMag)

TuMag (see Figure 19) is a tunable, dual-beam imaging spectropolarimeter in visible wavelengths (del Toro Iniesta et al. 2025). It has been designed, developed, and manufactured by the S^3PC to probe the LoS velocity and vector magnetic field of the photosphere and the low chromosphere across a FoV of 63” × 63”. It builds upon technical solutions proven in the Sunrise I and II flights of the IMaX instrument (Martínez Pillet et al. 2011) and on the PHI instrument (Solanki et al. 2020) aboard Solar Orbiter, like the use of liquid crystal variable retarders as polarization modulators and a $LiNbO_3$ solid Fabry-Pérot etalon as spectrometer in collimated configuration, while PHI incorporates the etalon in telecentric configuration. TuMag implements a number of technical innovations, like a state-of-the-art double filter wheel (Sánchez et al. 2022), two custom-made cameras (Solar Physics Group Cameras, SPGCams, Orozco Suárez et al. 2023), a composite-material optical bench (Fernández-Medina et al. 2023), specialized thermal control means for critical subsystems (Gonzalo et al. 2023), and completely new electronics, software and ground support equipment. Its optical design enables spatial sampling of the solar surface at frequencies above

the Nyquist cut-off. Quasi-simultaneous, precise full-Stokes polarimetry is possible in multiple wavelengths across the line profiles of any two among the three Zeeman-sensitive Fe I (525.02 nm and 525.06 nm) and Mg I line (517.3 nm) spectral lines in less than 90 s.

The optical unit is controlled by the electronic unit, which utilizes commercial off-the-shelf components within a pressurized box to ensure functionality in low-pressure environments. The electronic unit includes a power converter module, a high voltage power supply (HVPS) to drive the etalon, an Analog, Motor, and Heaters Drivers (AMHD) module to control the filter wheel, the liquid crystal variable retarders (LCVRs), the HVPS, and to thermally control the instrument and monitor its status, and a digital processing unit to manage and control the whole instrument. This processing unit is based on an NVIDIA® Jetson TX2, with an embedded multimedia card with 8 TByte solid state disk (SSD) external data storage, and it runs the different observation modes, compresses the data, and sends them to the ICS. The control software, firmware, and ground support equipment have been developed by S^3PC to maximize commonalities with SCIP.

TUMAG's spatial resolution is determined by the aperture of the SUNRISE telescope, and allows to resolve structures of ≈ 80 km on the Sun, oversampled by about a factor three, so that the pixel size is about 0.037", or 27 km on the Sun. The narrow-band tunable filter is a $LiNbO_3$ solid-state Fabry-Pérot etalon, an identical spare device to the one already flown on SUNRISE I and II. It is used in double pass, which relaxes the demanding requirements on passband stability and saves mass and power. The spectral resolution is ≈ 7 pm, corresponding to the full width at half maximum (FWHM) of a Gaussian function representing the spectral transmission profile of the instrument. To select the three different spectral lines, the filter wheel is equipped with narrowband interference prefilters, which can be switched at a speed better than 6 s. The filter wheel also hosts a plate introducing a well-defined defocus for phase diversity measurements, allowing to reconstruct the point spread function (PSF) of the instrument (Bailén et al. 2022b,a). The LCVRs provide optimum polarization modulation and guarantee a polarization efficiency exceeding 95% in all four Stokes parameters. This assures achieving a polarimetric sensitivity better than 10^{-3}, in units of the continuum intensity, at a cadence of one observation in about 10 s to 60 s, depending on the number of wavelength points and the observation mode of the instrument (see Table 8 in del Toro Iniesta et al. 2025). The filter wheel also hosts two in-flight polarization calibration devices, a linear polarizer and a micro-polarizer calibration target,[2] allowing for the first time to perform in-flight polarization calibration measurements.

4.4.3. SUNRISE Chromospheric Infrared Spectro-Polarimeter (SCIP)

SCIP, designed and built jointly by NAOJ (lead) and S^3PC with contributions from Japan Aerospace Exploration Agency (JAXA) and MPS, performs spectropolarimetry in near-IR photospheric and chromospheric lines with well-known properties. SCIP emphasizes spectral resolution and polarimetric precision. The Stokes spectra of these lines are characterized by a high magnetic sensitivity, thanks to large Zeeman splitting at the long wavelengths at which SCIP observes, and by the absence or at least greatly reduced strength of telluric blends. These characteristics greatly simplify the interpretation of SCIP spectropolarimetry data compared to data recorded from ground-based observatories in this wavelength range. SCIP is therefore highly complementary to the near-UV spectropolarimeter SUSI (Section 4.4.1), which offers increased resolution in the spatial and height domains at the expense of a lower photon flux and a more complex analysis.

[2]Patent pending. Patent application number: EP2282703.1 "Calibration target and method for the snapshot calibration of imaging polarimeters", Alberto Álvarez-Herrero and Pilar García Parejo, 22 July 2022.

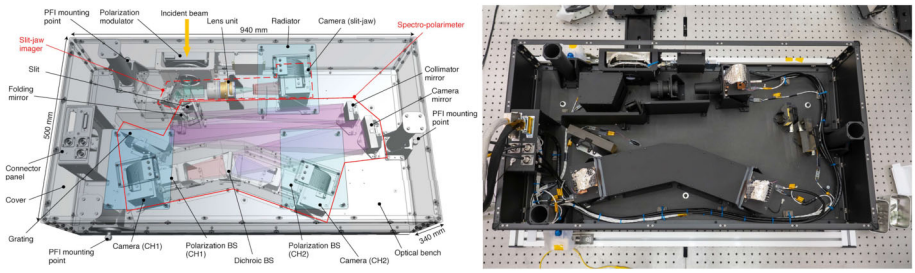


Figure 20 Opto-mechanical layout of SCIP (*left*) and pre-flight laboratory setup (*right*) showing opto-mechanical elements mounted on an optical bench made of a carbon fiber-reinforced polymers (CFRP) sandwich panel with low thermal expansion.

SCIP allows for simultaneous full Stokes measurements in two spectral regions. One of the spectral channels contains two of the Ca II infrared triplet lines at 849.8 nm and at 854.2 nm that form at chromospheric heights (see Figure 4). This spectral channel is highly suitable for studying the stratification of magnetic fields in the solar chromosphere due to its sensitivity to atmospheric heights ranging from the photosphere to the middle chromosphere (Quintero Noda et al. 2017). The second spectral window is centered on the K I D1 and D2 lines at 769.9 and 766.4 nm, respectively. These spectral lines allow us to probe the upper photosphere and the temperature minimum heights, but are very poorly accessible from the ground due to absorption mainly by O_2 in the Earth's atmosphere at these wavelengths (Quintero Noda et al. 2018). When combined with highly Zeeman-sensitive Fe I photospheric lines present in the Ca II spectral window, they allow to seamlessly retrieve the magnetic and thermodynamic parameters through all photospheric and most chromospheric heights.

The absence of atmospheric refraction and seeing at the float altitude of SUNRISE ensures perfect co-pointing between the two SCIP spectral regions, even though they are separated by almost 100 nm. Together, and along with the information from SUSI, the spectral lines in both spectral bands constrain the conditions in the solar atmosphere to unprecedented accuracy, well beyond what can be achieved by current ground-based solar telescopes.

The opto-mechanical layout of SCIP is shown in Figure 20 (Uraguchi et al. 2020). The basic optical configuration of the SCIP spectrograph is a reflective Littrow-configuration using a high-order echelle grating and aspheric mirrors (Tsuzuki et al. 2020). The slit width and the spatial pixel sampling are 0.094" to reach a spatial resolution of 0.19", which is the diffraction limit at 770 nm. The slit length and the scan mirror cover a FoV of 58" × 58". Both wavelength channels with different diffraction orders are separated by a dichroic beam-splitter and focused onto two cameras. Each camera employs a dual-beam polarimetric setup with a polarising beam-splitter (PBS) projecting both orthogonal polarization beams on the same sensor. The cameras employ a back-thinned, 2k × 2k complementary metal oxide semiconductor (CMOS) sensor (SPGCams, Orozco Suárez et al. 2023).

As in SUSI, the PMU is based on a rotating waveplate whose retardation is optimized to have good polarization modulation in the spectral channels (Kubo et al. 2020). By synchronizing rotating phases of the waveplate and exposures of two SPGCams, modulated spectra are read-out every 32 ms and are demodulated on-board to produce polarized spectra every 512 ms as a minimum integration cycle at each slit position (Kubo et al. 2023). Because the waveplate consists of quartz and sapphire plates, anti-reflection coating is applied to all the surfaces and their parallelism is well controlled to suppress fringing and intensity variations. The beam wobbling is attenuated by adjusting a tilt to the waveplate with respect

to the rotating axis and is smaller than 0.01" rms. The polarization measurement system of SCIP provides 3×10^{-4} (1σ) polarization precision (Kawabata et al. 2022) when integrated for 10 s.

The scan mirror mechanism (SMM, Oba et al. 2022) is placed in the SCIP scan unit (see Section 4.3.1). SCIP has a slit-jaw imager whose wavelength is centered at around 770.5 nm to obtain a continuum image. The read-out of the slit-jaw camera is also synchronized with the rotating waveplate and the two spectrograph cameras. In addition to the polarimetric measurements, SCIP allows a rapid scanning observation only for intensities in which the scan mirror is stepped every 64 ms to cover the FoV of 58" × 58" in 40 s. In this mode, the waveplate continues to rotate. The resulting intensity modulation is corrected in the post-flight data processing pipeline.

4.5. Electronic Units

4.5.1. Electronic Units of the Science Instruments

The scientific instruments described above are controlled by their own electronic units. The units for SCIP, TUMAG and CWS are located on the E-racks on the $+x$ and $-x$ side of the gondola (see Figure 9), whereas the SUSI is managed by the ICS directly and by a proximity electronic unit located in the PFI. The electronic units of the instruments are connected to the corresponding optical units and detailed in the individual instrument sections and papers.

4.5.2. Instrument Control System (ICS)

Unlike many ground-based solar observatories, the balloon-borne SUNRISE III observatory is designed for largely autonomous operation allowing for an automated execution of several-hour long scientific observing programs. For this purpose, the onboard hardware of SUNRISE III is hierarchically structured. The central node is the ICS that provides several Ethernet and serial interfaces for the communication with the scientific instruments, other onboard subsystems, and the ground operation center (see schematic representation in Figure 22). The main elements of the ICS are a single-board computer, also named Instrument Control Unit (ICU), and two Data Storage Systems (DSSs) for onboard storage of science data and HK data (see Figure 21).

The ICS carries out the following tasks: (i) Control the three science instruments SCIP, TUMAG, SUSI, the image stabilization and autofocus system CWS, as well as technical subsystems, (ii) store science and HK data on the DSS, (iii) transfer HK data and extracts of science data (thumbnails) to the ground station, (iv) monitor critical HK values and initiate pre-defined actions if lower or higher thresholds are hit, (v) receive commands from the ground station and execute them, and (vi) run the timeline, i.e., execute pre-defined observing programs in an coordinated way for all instruments.

The ICU is based on the mainboard Supermicro X10SDV-7TP8F, equipped with an Intel Xeon D-1587 processor with 16 cores, 128 GByte of volatile memory in the form of four Samsung DRAM 32 GB DDR4-2133 ECC modules, and two SSDs of 128 GByte each in a RAID1 configuration for redundant storage of program code and configuration files. The ICS is built up mainly from commercial off-the-shelf components, whose operational reliability is guaranteed by housing the ICS in a pressurized vessel.

48 Samsung PM883 7.68 TByte SSDs are available for storing HK and science data of the instruments. The SSDs are distributed over two DSSs that are identical in construction. Each DSS is equipped with an internal controller connected to the ICU via a serial interface.

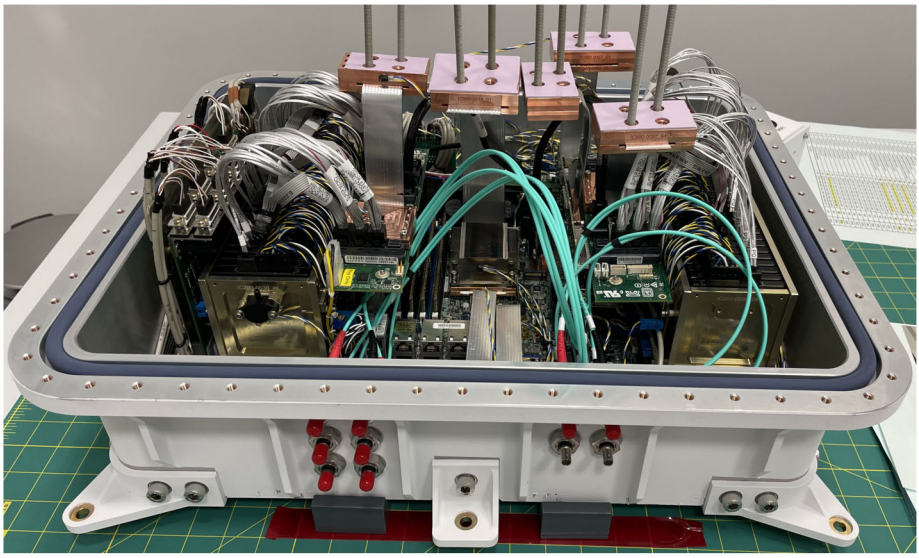


Figure 21 ICS shortly before the final closing in October 2021. The mainboard of the ICU is at the bottom of the housing, left and right are the two DSS stacks containing the SSD disks. Identified hot spots on the electronic boards are connected via heat pipes to copper blocks. During the closing procedure, the guiding threading rods are replaced by screws that attach the copper blocks to the lid via gap pads.

The controller provides HK data (temperatures, pressure, humidity) and allows for switching the power lines of the SSDs. In order to avoid data losses in the case of an SSD failure, the SSDs are organized in RAID5 chains of 4 SSDs each. The effective capacity of a chain is 20 TByte, which leads to a total capacity of the two DSSs of 240 TByte. To minimize the power consumption, just one chain is powered at any moment in time. If the current chain is completely filled with data, the chain is switched off and the next chain is used.

An important design driver was the high total data rate generated by the three science instruments of about 700 MByte/s, which is several orders of magnitude higher than the available telemetry bandwidth. Each science instrument is therefore equipped with an embedded PC acquiring and pre-processing the camera data as well as controlling its mechanisms. The camera data are transferred via a gigabit Ethernet to the ICU and stored on the DSS. A slightly different approach was chosen for the SUSI instrument. Because the data rate generated by SUSI is much higher than the network bandwidth of 1 Gbit/s, the SUSI software and the ICU software run on the same single-board computer of the ICS. It is thus possible to transfer the camera data directly from the SUSI software to the ICU software via local-host communication without requiring a 10-gigabit Ethernet interface.

The ICS is also responsible for preparing the HK data and quick-look thumbnails (see Section 4.5.5) for transfer to the ground station via the various communication channels (see Section 4.5.4). Central node of the ground station is the system electrical ground support equipment (EGSE), which displays system-relevant HK data. A color coding helps the operator to easily identify critical out-of-range values during testing and flight. In addition, the system EGSE distributes the instrument-specific HK data to the individual instrument EGSEs.

4.5.3. Electrical Power Consumption and Infrastructure

The nominal power consumption of SUNRISE III during science operation amounts to ≈ 750 W. The peak power consumption occurs during the ascent, where heaters are switched on to prevent the instruments and mechanisms to cool down below their non-operational limits, and can reach a maximum value of 1031 W. SUNRISE III can also be operated in an idle/safe mode, requiring 405 W.

The PDU is responsible for the power management. During the flight, it receives power from solar panels in combination with a battery buffer, and redistributes it to the various subsystems via ground controllable switched power lines. Two solar panels are mounted in two frames on the $+x$ and $-x$ side of the gondola (see coordinate system in Figure 9). At float altitude they provide a peak power of 1824 W and an average power of 1700 W after stable sun pointing is achieved. They are connected to the battery bank via a Morningstar TS-MPPT-60 maximum peak power tracker solar charge controller. The battery bank uses a set of four Odyssey PC1700 pure lead batteries with two cells wired in series and two in parallel (2s2p configuration). Each battery has a capacity of 60 Ah at room temperature, enough to operate the heaters and some selected electronic components (including the ICS) during the ascent phase when the gondola is free spinning and not constantly aimed at the Sun. The bus voltage ranges between 20.4 V and 29.2 V (nominal 27 V). For ground operations and battery charge-up, the system stays connected to a ground power supply until ≈ 30 minutes before launch. The scientific instrumentation is powered by the PDU via two separate 75 A circuits to two PFI Power Distribution Units (PPDs) ($+x/-x$) that provide individually switchable outputs for the instrument subsystems and mechanisms and a direct power output to the ICS.

As an independent system, the SIP, provided by CSBF, is responsible for controlling the balloon (e.g., ballast dropping, apex Helium valve venting, termination) and to communicate to and from the ground. The SIP is powered by its own independent power system with its own set of solar panels, installed on the 4 sides of the gondola, to ensure continuous power also when the gondola is freely rotating and not constantly facing its front side at the Sun. One component of the SIP is the so called Science Stack (SS), which provides an independent power switching and HK interface to the PDU.

The PDU including the batteries and the solar panels was built by APL. The SIP and SS fall under the responsibility of CSBF, whereas the PPDs were designed and built by MPS.

4.5.4. Network Infrastructure and Communication Systems

The internal communication within the SUNRISE III observatory is based on an Ethernet network (see Figure 22). This network ensures the communication between the ICS on one side and the Pointing Control System (PCS), the in-flight communication systems and the scientific instruments on the other side. A bandwidth of 1 Gbit/s (1000 base TX) is needed for the data transfer from SCIP, TUMAG, and the CWS to the ICS. The high frame rates of the SUSI cameras combined with the necessity to store all frames for on-ground spectral restoration require a different setup, with a local-host communication between SUSI and ICS. The SUSI cameras are directly connected to the ICS with fiber-optics cables, and the SUSI software for data acquisition and storage runs on the ICS. In addition, SUSI is connected via a 1 Gbit/s Ethernet line for commanding and communication with the SUSI hardware.

For the inflight communication (ground to gondola, gondola to ground), SUNRISE III uses LoS and satellite Telemetry and Telecommand (TM/TC) systems (i.e., systems for up- and

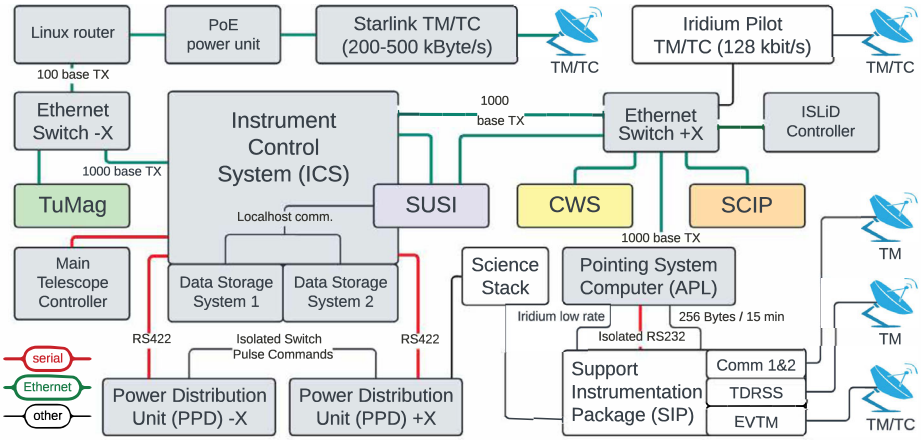


Figure 22 SUNRISE III network setup illustrating the data connections within the SUNRISE III observatory and to the TM/TC links to the ground stations. *Colored boxes* indicate the scientific instruments, *gray boxes* the central units provided by MPS and APL, and *white boxes* show the CSBF equipment.

Table 4 Communication channel overview used for the SUNRISE III flights in 2022 and 2024 with directional information (TM/TC = up- and downlink, TM = only downlink), achieved bandwidths and the availability during float phase (in percent) or during the LoS phase only.

	Comm 1&2	Iridum pilot	TDRSS		E-Link	Starlink	EVTM
			Omni	High-gain			
2022/2024	✓/✓	✓/✓	✓/✓	✓/✗	✓/✗	✗/✓	✓/✓
Bandwidth (kbit/s)	1.2	128	6	92	2000	8000	12,500
Direction	TM/TC	TM/TC	TM	TM	TM/TC	TM/TC	TM
Availability	near 100%	near 100%	$\geq 85\%$	$\geq 85\%$	LoS	99.9%	LoS

downlink), provided by CSBF and APL, and for the 2022 flight also by SSC (see summary in Table 4). They are used for commanding, house-keeping and thumbnail image transmissions.

The CSBF systems (white boxes in Figure 22) include the SIP on the flight deck below the telescope, the antenna boom for Global Positioning System (GPS) navigation and ground- and satellite communication antennas, and provide the following communication channels available during the full flight phase: (i) the TM/TC satellite communication system Iridium Pilot® with up to 128 kbit/s, (ii) two low-rate science port TM/TC channels primarily for commanding redundancy (Comm1 & Comm2, 1200 bit/s; TC availability depends on satellite schedule), and (iii) the Telemetry (TM, downlink-only) Tracking & Data Relay Satellite System (TDRSS) omni-directional channel with 6 kbit/s. For the 2022 flight, also the high-gain TDRSS TM channel (92 kbit/s) was available. For the early phase of the mission, when the balloon is still visible from the ground station, the downlink-only Ethernet Via Telemetry (EVTM) with up to 12.5 Mbits/s allows for an efficient data transfer during the commissioning phase. The duration of this so-called LoS phase depends strongly on the wind conditions on the launch day and was for the 2024 flight in the range of 12 hours.

As a last-minute upgrade to the 2024 flight, APL initiated the installation of Starlink from the U.S. company SpaceX. It proved to be the most reliable and fastest TM/TC communication during the Galactic/Extragalactic ULDB Spectroscopic Terahertz Observatory (GUSTO) flight in Antarctica (2023/2024 season, Goldsmith et al. 2022), offering higher bandwidth and coverage than the previously flown systems. Starlink on SUNRISE III is installed and managed by APL and MPS. The Starlink antenna is mounted on the CSBF antenna boom, and is powered via a proprietary Starlink cable connected to a Power over Ethernet (PoE) injector. A single-board Linux computer with two network interface controllers (NICs) acts as a router, providing the gateway from the gondola network to the wide-area network provided by Starlink.

During the 2022 flight, the Esrange Airborne Data Link (E-Link) system was rented from SSC. It promised a high-bandwidth, bi-directional communication during the LoS phase, to be extended to up to 20 hours after launch by the use of a mobile transmitter station placed in Andenes (Norway). This system was not used for the 2024 reflight, since E-Link is no longer maintained by SSC, and the costs for the system were too high for the unreliable performance during the 2022 campaign. Also, the TDRSS high-data rate channel with up to 92 kbit/s, used during the 2022 flight, was not available for the 2024 flight. The pointable high-gain antenna required by this system had to make space for the antenna of the Starlink system.

Connection to the observatory was maintained for 99.9% of the flight time, achieving data rates via Starlink consistently exceeding 1 MByte/s. The stable and high-speed connection allowed operating SUNRISE III almost like a ground-based telescope, with continuous housekeeping data and near real-time thumbnail image transmission (see next section). Commands sent from the GOC were executed with almost no delay, with the response visible on the housekeeping monitors after a few seconds only. The other communication channels also worked well, and were kept alive as a backup option in case Starlink would drop out, which did not happen.

4.5.5. Housekeeping and Thumbnail Concept

The ICU collects more than 1200 different HK values from the gondola and PCS, the telescope, PFI, ISLID, the CWS, and the three science instruments. The values were recorded every 2 seconds and sent to the ground station via the various communication channels (see Section 4.5.4). The HK values were displayed on a dedicated screen in the GOC and continuously monitored. A color-coding indicated for every HK value if it was within the expected range (green), close to the critical value (yellow), or outside the allowed range (red).

Of special interest were values about the power consumption (currents and voltages) of the instruments and the temperature of critical components. Under special surveillance were the temperatures of the HRW and inside the ICS. The HRW temperatures were lower than expected (40 – 45 °C), showing that the new concept of using a diamond-milled surface worked very well (see Section 4.2). Similarly, the ICS temperatures stayed within the allowed boundaries. Power monitoring turned out to be crucial for the success of the mission. Two major power anomalies occurred when the charge controller stopped delivering power from the solar panels to the batteries, and the observatory had to operate solely on battery power (see Section 2.2.1). The early discovery of this failure allowed the operators to develop a rescue strategy before the batteries had fully drained (4 – 5 hours). Reducing the load on the charge controller by turning the observatory away from the Sun and by switching off instruments brought the charge controller back to the nominal state, and observations could be resumed with only a minimal disruption.

The fast up- and downlink channel via Starlink enabled the download of around 118 GByte of data during the 6.5-day-long flight, including high-quality thumbnail images from the three science instruments nearly continuously. The accurate pointing to the targets defined during the science planning could be guaranteed by fine-adjusting the position using the near real-time thumbnail images, increasing the scientific value of the data significantly and enabling good overlap with the regions observed by the co-observing facilities. The quality of the thumbnail images could be tuned to almost native resolution, providing excellent information about the in-flight optical performance of telescope and instruments.

4.6. Piggybacks

SUNRISE III offers the opportunity of a stratospheric flight for two piggyback payloads: the Image Recording Instrument for SUNRISE III (IRIS-2) and the RAdiation MONitor (RAMON). IRIS-2 delivered spectacular images and videos of the observatory during all flight phases, and RAMON is a space radiation monitor dedicated to measure high-energy particle showers. The piggyback payloads were designed to have minimal interference with the observatory and to work completely autonomously.

4.6.1. IRIS-2

IRIS-2 is a video recording and picture capturing instrument. It was designed and built by a Spanish team of enthusiastic amateur astronomers, engineers and technicians, with heritage from IRIS-1, which flew on SUNRISE II in 2013. The instrument's primary goal is to provide imagery of the flight for communication and public outreach purposes, and additionally for monitoring and improving the performance of mechanical interfaces and the PCS of the observatory from launch to landing and recovery.

IRIS-2 is attached to the top of the gondola's left roll-cage (see yellow circle in Figure 23), and boasts four cameras pointing in four directions: to the front (horizon - sun-side), the rear (telescope mirror), lateral (horizon and part of the gondola), and upwards (sky, balloon, and part of the gondola). The cameras (GoPro Hero 4 Black) record 4K-resolution 30-fps video for 2 hours during launch, 1 hour during landing, 15 minutes at 120-fps during balloon release, and then capture pictures with a 120 s interval at other moments of the flight for time-lapse creation. The instrument can cover a flight duration of 6 to 12 days depending on the configured time-lapse interval.

The instrument's onboard computer is based on an MSP430 ferroelectric random access memory (FRAM)-based microcontroller, with spaceflight heritage, coupled with external memories for telemetry, real-time clock (RTC), IMU, and pressure (altimeter) sensors on a custom-designed printed circuit board (PCB). The flight software is coded in C on an finite state machine (FSM) structure with custom-made libraries for external bus communications. The power system, based on Nickel metal-hydride batteries with a capacity of 160 Wh, does not rely on external power from the gondola. The instrument is only interfaced to the ICS through a digital pin to signal flight events from mission control, with the gondola being isolated by an optocoupler. The IMU and altimeters are used as redundant triggers for the different phases of the mission, as the instrument does not provide feedback to mission control. All the telemetry from the instrument must be dumped from its internal memories once it is recovered. The structure, built on extruded aluminum profiles and panels, is internally protected by low thermal conductivity foam panels, and has internal camera holders that allow for fine-tuning of the pointing. IRIS-2 has a size of $200 \times 200 \times 150$ mm^3, a mass of about 5 kg, and consumes around 0.02 W in standby and a peak of around 18.1 W at launch



Figure 23 SUNRISE III shortly before the launch on 10 July 2024, hanging on the launch vehicle Hercules. The locations of the piggy back payloads IRIS-2 and RAMON are marked with the *yellow* and the *red circles*, respectively. Image courtesy: SSC / Mattias Forsberg.

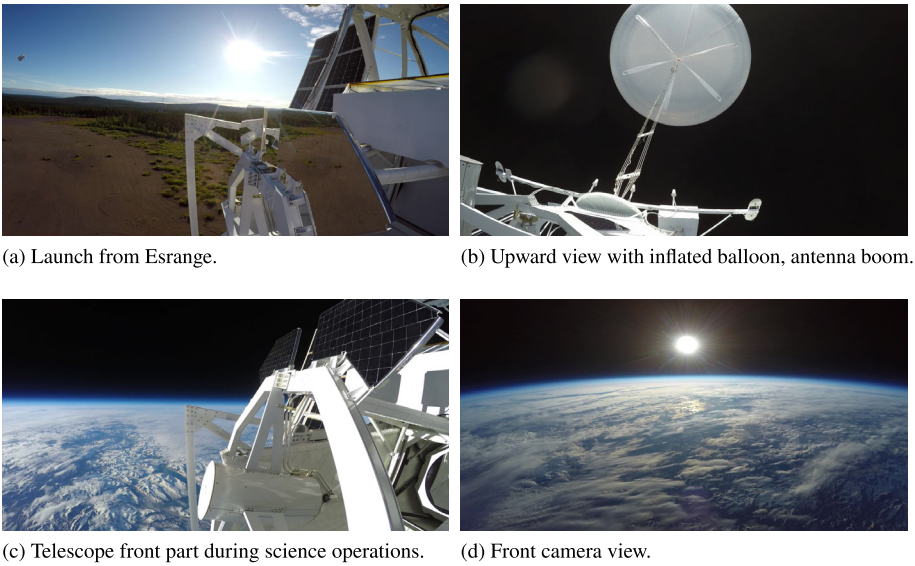
recording. The instrument was tested with a thermal-vacuum (TV) test and underwent several full-duration-flight runs simulating expected flight conditions.

The performance of IRIS-2 during the first SUNRISE III flight in 2022 was nominal, taking over 8 hours of video and over 16,000 still frames. The videos and pictures of the launch, flight, landing, and recovery have allowed the SUNRISE team to better understand the events that happened during the different phases of the flight, confirming the usefulness of a relatively small and inexpensive instrument for such flights.

IRIS-2 was flown again on the SUNRISE III flight in 2024 and produced a stunning view from the observatory during all phases of the mission, from launch until the landing and the recovery in Canada (see Figure 24). In total, IRIS-2 recorded 8.5 hours of video and captured over 16,000 still frames, 14,576 of which were taken during the flight and the remainder after landing. The only anomaly during the IRIS-2 mission was with the rear-facing camera, whose power was automatically cut three minutes before landing as a self-protection measure while passing through a thick layer of clouds and heavy rain. The other three cameras successfully captured the landing.

4.6.2. RAdiation MONitor (RAMON)

When a high level energy particle coming from space impacts the higher layers of the Earth's atmosphere, atmospheric showers are produced. They consist of a cascade of secondary particles produced by the interaction of the incoming particle with the air molecules. As the showers go down through the atmosphere, more secondary particles are produced, but with less energy, becoming a very useful natural mechanism to avoid dangerous space radiation from hitting the Earth's surface and thus to preserve life as we know it. Atmospheric



(a) Launch from Esrange.

(b) Upward view with inflated balloon, antenna boom.

(c) Telescope front part during science operations.

(d) Front camera view.

Figure 24 IRIS-2 images recorded during the 2024 flight.

showers have been frequently measured at aeronautic heights, as it is relatively easy to include radiation detectors in airplanes. However, there are less measurements at stratospheric heights, and this is becoming a very important layer for use cases like scientific balloons, communication platforms and high altitude pseudo satellites.

RAMON was developed by the Spanish SME Hidronav Technologies under the leadership of INTA, for a flight on the SUNRISE III mission (see red circle in Figure 23). It delivered already valuable data during the short 2022 flight, and was again part of the payload for the 2024 mission. Unfortunately, the 2024 flight did not deliver any data, since the long waiting time for the launch window resulted in the complete drainage of the batteries, which was discovered only a few hours before the launch with no possibility anymore to react.

RAMON is based on the Cosmic Watch radiation monitor developed by Massachusetts Institute of Technology (MIT), with modifications by Hidronav Technologies to improve its performance. Each monitor consists of two $5 \times 5 \times 1$ cm^3 scintillators, each with its associated Silicon PhotoMultiplier (SiPM), its Arduino microcontroller, and the necessary electronics to treat the electric pulse generated when an ionizing particle hits the scintillator. The scintillator converts the energy from the ionizing particle into visible light and the SiPM converts it into an electric pulse which can be conveniently managed. Every time this process occurs, an event is recorded on the corresponding storage card (one for every scintillator). Particles exciting both scintillators trigger a so-called coincidence event, useful for detecting primary particles which are more energetic than the secondary ones.

4.7. Thermal Concept

The SUNRISE III thermal design concept is similar to that of previous missions, with system-level solutions akin to those employed in the second flight (Pérez-Grande et al. 2011). However, advancements have been made in thermal analysis and modelling. A distinctive thermal

environment characterization (González-Llana et al. 2018), based on real-data observations, considers local and temporal variability in key parameters (albedo, outgoing longwave radiation (OLR), and solar radiation). The analysis assumes a quasi-steady state for a stratospheric balloon at 40 km altitude, allowing to focus on steady-state cases during which the combination of environmental parameters is maximized and minimized to determine maximum and minimum temperatures (González-Bárcena et al. 2019).

A thorough analysis of the ascent phase, critical for thermal considerations in platforms like SUNRISE III, has been conducted (González-Bárcena et al. 2022). Unlike satellites, the ascent phase means a challenge due to low temperatures in the tropopause and jet streams at around 12 km altitude. The system's minimum temperature may occur during this phase, thus, a quantification of convection heat transfer is needed (Fernández-Soler et al. 2023). A characterization of the thermal environment throughout the atmosphere, specific to the launch location and epoch, was also conducted for polar long duration balloon missions launched from Esrange in summer (González-Bárcena et al. 2020).

SUNRISE III's thermal design can be summarized as follows: The electronic units are mounted on two white-painted E-racks on both sides of the gondola, offering a direct view to the cold sky and Earth. The rack does not provide a controlled interface to the attached units, therefore their thermal control is their own responsibility. To avoid the freezing of the instruments during the ascent phase, the E-racks are shielded from external winds with transparent windshields made of a 1.5 mil thick linear low-density polyethylene (LLDPE) film, allowing solar and infrared radiation to pass through. During the initial phase of ascent, the gondola rotates, exposing the E-racks to direct sunlight, which contributes to heating the units.

The telescope thermal design is based on the concept of the previous flights with some improvements. The surface of the HRW is now diamond milled on the aluminum bulk (see Section 4.2), reflecting around 85% of the incoming solar radiation. To mitigate the blurring effect caused by too high temperatures, two ammonia-based heat pipes are used to transfer the absorbed heat flux by the HRW to two SSM radiators situated in the upper section of the telescope's front ring. A multilayer insulation (MLI) made of Betacloth 500 GW and vapor deposited aluminum (VDA)-coated Mylar is used to prevent additional heat loads on M2 and the HRW coming from the Earth or the lower deck equipment. It is attached to the front ring struts of the telescope, differing from its attachment to the roll cage in previous missions.

The science instruments are placed in the PFI module. Its sun-facing front part is protected with a sun shield. High solar reflectivity ($\varrho = 0.8$) for the whole structure is achieved by a styrofoam cover with aluminized Mylar on the outer face. The thermal control of the instrumentation is based on the use of radiators coated with white paint on the top to dissipate the internal power. Every instrument is insulated from the structure with a single layer of VDA-coated Mylar foil, providing them with more thermal stability. Finally, similarly to the E-racks, an LLDPE film, has been used to cover the top part of the PFI to act as a wind shield to avoid freezing of the instruments during the ascent phase.

During the flight in July 2022, the temperatures reached at the floating altitude were inline with steady-state predictions. Due to the malfunction during the launch, the thermal analyses were re-executed considering that the instruments were in a non-operational mode with the telescope elevation angle at 60°. The sensor's measurements are shown in Figure 25. The thermal analysis includes results from extreme hot and cold operational cases and hot and cold non-operational cases in which instruments were off and the telescope curtain was closed. During the initial phase of the ascent, the gondola rotation exposed the E-racks to direct solar radiation, preventing excessive cooling. At an altitude of around 26 km, the

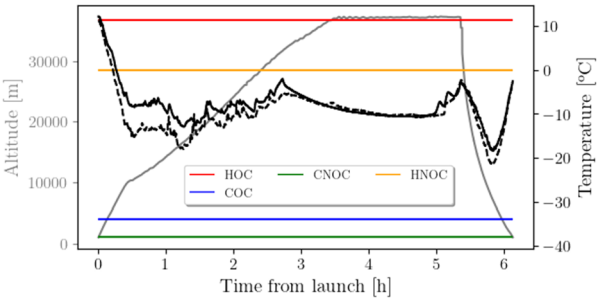


Figure 25 E-rack $-x$ temperature measurements during the 2022 flight of SUNRISE III (*solid* and *dashed black lines*) compared to operational (*red* and *blue*) and non-operational (*green* and *yellow*) case analyses.

gondola started pointing to the Sun, and the solar panels blocked direct sunlight, leading to a noticeable temperature reduction in the E-racks, and visible in Figure 25 in the smooth, exponential temperature decrease between 2.8 and 5 hours after launch. The temperature gap between the hot and cold non-operational cases was found to be influenced by the Sun's relative position over the horizon and the changing environmental conditions (albedo and outgoing longwave radiation) during the flight. The thermal analysis for the 2024 flight will only be available after the data reduction phase.

5. Observatory Testing and Flight Preparation

All components and instruments of the observatory underwent thorough testing on component/subsystem level and also in the fully assembled state. The tests on instrument level are described in the individual instrument papers, the description of the tests in this section concentrates on the ones performed at system level and after the integration of the instruments into the PFI.

5.1. Test of Mechanisms

A crucial part in a remotely operated observatory is the reliable operation of all its mechanisms, requiring extensive testing under realistic conditions. The mechanisms can be divided into four groups:

1. Gondola mechanisms: Momentum Transfer Unit (MTU), elevation drive, roll wheel, brake (launch-lock), and X-Y Stage mechanism. These mechanisms guarantee the correct pointing of the observatory and secure the telescope during launch, ascent, descent and landing. The mechanisms and their tests are described in the gondola paper (Bernasconi et al. 2025).
2. Telescope mechanisms: The M2 mechanism allows for an adjustment of M2 in three degrees of freedom (translational motions in x, y, z, in the telescope coordinate system, see Figure 9). M3 and M4 are equipped with mechanisms for axial movement, and the curtain mechanism opens and closes the protective curtain for M1 in the central frame of the telescope.
3. ISLID mechanism: The filter wheel in F2 (see Section 4.3.1) allows to insert 6 different targets and a closed (dark) position into the light beam. They are used for the calibration of the instruments, and to determine their in-flight performance and alignment.
4. Instrument mechanisms: Every instrument has its own mechanisms, e.g. for rotating filter wheels, moving the grating and the slit, or rotating the waveplate in the PMU. These

mechanisms and their testing are described in the individual instrument papers (Berkefeld et al. 2025; Feller et al. 2025; del Toro Iniesta et al. 2025; Katsukawa et al. 2025).

The telescope mechanisms to control the mirrors M2, M3 and M4, and for opening and closing the curtain were already flown in SUNRISE I and II. Thorough thermal vacuum testing was performed prior to those flights. For the re-use of the mechanisms in SUNRISE III a thorough maintenance and cleaning was performed, and their functional and electrical reliability was verified by extensive ground testing. Functional tests were repeated after the 2022 flight.

The ISLiD filter wheel is a new development for SUNRISE III. It allows placing the following targets into the light beam for calibration measurements: open beam (nominal observations), closed (common dark), 2 random dot targets (co-focus check), U.S. Air Force (USAF) target (resolution and image orientation), polka dot target (near-field straylight), rectangular grid (distortion), and a knife edge (far-field straylight). These targets allowed to assess the instruments' in-flight performance. Both, the filter wheel mechanism and its controller, were tested under flight conditions in the MPS thermal vacuum chambers. The detailed test report is available in the S3-DocDB document SR3-MPS-RP-LD700-004 (Eberhardt 2021).

5.2. Optical Tests

All optical instruments and ISLiD were individually optically tested and characterized prior to integration into the PFI. ISLiD was tested by interferometry between F2 and the exit foci, respectively, in double pass autocollimation against a high precision reference sphere. The interface positions were verified by a laser tracker. In addition, images of the F2 targets were taken in the exit foci by a camera. After the integration of the scientific instruments and the CWS into the PFI, co-alignment and optical performance between F2 and the science foci were tested using a stimulation system, which mimicks the telescope beam. High power light-emitting diodes (LEDs) were used as light sources, optimized for the different spectral channels.

For the optical tests of the instruments the filter wheel unit of ISLiD in F2 was used. An accurate determination of the performances of all instruments could be achieved, and the proper co-alignment between the different science foci could be verified (see instrument papers: Berkefeld et al. 2025; Feller et al. 2025; Katsukawa et al. 2025; del Toro Iniesta et al. 2025).

5.3. Polarimetric Calibrations

All three science instruments were designed to measure the polarization state of the incoming solar radiation to a level of 10^{-3} of the continuum intensity or better. To achieve this precision, polarimetric calibration campaigns were executed at various stages of the project. The most important ones were the calibration measurements in the fully assembled state, with the instruments in the PFI mounted on top of the telescope, and the calibration light sources feeding the instruments from the prime focus (F1, at the position of the HRW) and the secondary focus (F2, inside the PFI). Calibration measurements were performed before and after the hang tests, with the observatory suspended from a crane (see Section 5.5), performed in the MPS balloon hall (2021 and 2022), and in the integration hall 'The Dome' in Kiruna (2022 and 2024).

The polarimetric calibration measurements for SUSI were all performed on the ground. A total of 35 independent measurements were carried out at different wavelengths by placing the Polarization State Generator (PSG), a motorized device generating 40 well-defined

polarization states from LED light sources for different wavelength ranges, at three locations within the beam path. These locations were the SUNRISE foci F1 and F2, and the entrance port of SUSI. A detailed description of the entrance-port calibrations is given in Iglesias et al. (2025), that uses eight SUSI standalone measurements to prove the instrument polarimetric response is stable enough to achieve the required sensitivity of 10^{-3} of the continuum intensity. As part of the ongoing data reduction process, the SUSI team is analyzing the polarimetric calibrations performed at SUNRISE foci F1 and F2 to derive the final end-to-end calibration strategy. We note that the measurements performed at the primary telescope focus F1 account for the polarimetric effects of the full beampath, except for the main mirror M1, thus no independent telescope calibration is foreseen. Instead, a correction of residual polarimetric crosstalks is performed using solar signals of known polarization properties acquired during the flight. These include zero-polarization targets such as spectral continuum, average quiet Sun and the magnetically insensitive Fe I line at 406.538 nm (see Iglesias et al. 2025, for extra details).

The SCIP calibration measurements were first performed at the instrument level at NAOJ before the integration into the PFI, in which a wire-grid linear polarizer and achromatic waveplate in the SCIP wavelength range were placed in front of the SCIP beam entrance to produce the known polarization states from a halogen lamp. Polarization response matrices and their spatial and wavelength dependence were obtained, including the effects of synchronization with the PMU (rotating waveplate), cameras with rolling shutter, and onboard demodulation (see Kawabata et al. 2022, for details). After SCIP was mounted into the PFI and the telescope, the polarization response matrices were updated by the polarization calibration measurements from F1, accounting for the polarization effect of the telescope except for M1. The F1 calibration configuration was the same as for SUSI except for the achromatic wave plate and the LED, which were specific for the SCIP wavelength range. For both, SCIP and SUSI, no in-flight calibration measurements are possible.

TUMAG carried out the polarimetric calibrations for the three wavelengths and both cameras of the instrument with a modulation scheme by setting the retardances of the two LCVRs to [225°, 225°, 315°, 315°] (LCVR1) and [234.74°, 125.26°, 54.74°, 305.26°] (LCVR2), chosen to maximize the polarimetric efficiencies. The modulation was performed by applying voltages to the two LCVRs, corresponding to the calibration carried out with a variable angle spectroscopic ellipsometer from J. A. Woollam Co. The polarimetric efficiencies were further optimized by a fine-tuning procedure (Álvarez-Herrero, Parejo, and Silva-López 2018) to achieve polarimetric efficiencies over the whole FoV of $\epsilon \geq$ [0.95, 0.45, 0.45, 0.45], exceeding the requirements.

TUMAG allows for an in-flight, field dependent polarimetric calibration. The TUMAG filter wheel contains a linear polarizer and an array of 16×16 patches consisting of 3×3 micro-polarizers each, with polarization axes at 0°, 45°, 90°, and 135°. During in-flight calibration campaigns, the insertion of these targets allows to: (i) monitor the polarization modulation behavior of the instrument to identify deviations in polarimetric performance, and (ii) fine-tune the polarimetric modulation matrices over the entire FoV of TUMAG.

5.4. Vacuum Tests

5.4.1. ICS Thermal Vacuum Testing

The high requirements on computing power and disk storage capacity made it mandatory to assemble the ICS, SUNRISE III's main computer (see Section 4.5.2), from standard electronic components contained in a pressurized housing. The air-tightness of the housing and

the reliable cooling of the components inside the closed compartment had to be tested thoroughly under simulated flight conditions, including the thermally demanding ascent phase. The ICS was placed in a vacuum chamber at MPS, and over a time period of 5 days thermal cycles with the expected temperature ranges were executed, while the ICS was operated under full load and in idle state. It could be confirmed that the pressurized box was air-tight and that all temperatures measured with the temperature sensors inside the ICS as well as the mainboard temperature values (e.g. the CPU temperatures) stayed within the nominal values. The test procedure ('as-run') is described in the S3-DocDB document SR3-MPS-PR-IC000-001 (Ramanath and Bayon Laguna 2022).

5.4.2. PFI Vacuum Test

The PFI was tested in the big vacuum chamber of MPS ('Big Mac') in February 2022. The test setup, described in the S3-DocDB document SR3-MPS-PR-AV200-001 (Ramanath 2022), was as follows: The PFI with all scientific instruments installed in flight configuration was placed inside the vacuum chamber. The electronic units and EGSE systems to control the instruments and the mechanisms in ISLiD were placed outside the chamber, and connected to the PFI via vacuum feedthroughs. Illumination was done with both, artificial light sources and real sunlight, using the coelostat system on the roof of the MPS laboratory building, through a fused silica viewport located on the grey-room side of the vacuum chamber. During the 1-week long test the subsystems ISLiD, CWS, SUSI, SCIP, and TuMag were first operated individually, and on the last day together. The optical performance in vacuum between the F2 focus (optical entrance of the PFI) and the various science foci could be verified. The sunlight allowed to confirm the spectral performance of all instruments, and closed-loop locking of the CWS on the F2 target could be achieved. Since all sub-units had seen thermal vacuum testing before, the full PFI test was done at ambient temperature only. The PFI vacuum test confirmed that all subsystems performed within the specifications under the conditions expected during the flight.

5.5. Hang Tests

The so-called hang tests offer the possibility to test the observatory in full flight configuration. A crane takes over the role of the ladder/balloon and lifts the gondola a few tens of centimeters above the ground. This simulates well the flight configuration and allows to fully test all three degrees of freedom for the gondola and telescope pointing (azimuth, elevation, roll compensation). The tests were performed with solar illumination allowing full characterization of the PCS's Sun acquiring and tracking capabilities while simultaneously feeding all science instruments with real sunlight.

Hang tests were performed in October 2021 in the balloon hall at MPS, and during the preparations for the 2022 and the 2024 flights of SUNRISE III in and outside of the integration hall 'The Dome' at Esrange. The stable sun-pointing allowed for the opening of the curtain, and the illumination of the telescope and the PFI in a similar way as during the flight. Several hour-long stable sun-pointing could be achieved at both locations, proving the excellent performance of the PCS. Despite the poor seeing conditions for these locations, an rms pointing accuracy in the range of a few arcseconds could be achieved (see Section 6.1).

All three scientific instruments were operated in the planned orchestrated mode during these tests, and important inter-instrument alignment properties could be verified and confirmed for varying telescope elevation. The sunlight enabled the instruments to record spectra of the solar absorption lines, and to assess their spectral resolution. The achieved pointing

stability and the performance parameters of the instruments are summarized in the gondola paper (Bernasconi et al. 2025) and the individual instrument papers (Berkefeld et al. 2025; Feller et al. 2025; del Toro Iniesta et al. 2025; Katsukawa et al. 2025).

5.6. Communication Tests

Communication tests between the observatory and the ground station had been performed during the launch preparations in 2022 and 2024 at Esrange. For these tests, SUNRISE III was put into flight configuration with all communication hardware attached (including the LoS antennas for E-Link (2022 only) and EVTM and the antennas for the satellite communication systems Iridium Pilot and Starlink), and driven to a location on the balloon pad where satellite communication and ground radio station communication could be established.

The tests revealed some difficulties for the LoS communication system, especially for the E-Link service provided by SSC. The performance during the short 2022 flight was acceptable, albeit not optimal. Since the E-Link system is no longer maintained by SSC, and the high cost to benefit ratio, E-Link was not be used for the reflight in 2024. Similar tests were repeated prior to the Flight Readiness Review (FRR) for the 2024 flight, including tests of the Starlink system used for the first time on SUNRISE III.

5.7. Timeline Tests

The operation of SUNRISE III during the flight is based on the timeline concept described in Section 3.2.1: all instruments are directly controlled by the ICS with minimal required interference from the ground station. A thorough testing of the timelines and the observing blocks was therefore a mandatory step to ensure reliable and hassle-free operation.

The individual timelines from the instruments and the Pointing Control System (PCS) were compiled manually. A software simulator was used to verify the consistency of the timelines and to guarantee the accurate timing of the command sequences. Additionally, all timeline scripts where peer-reviewed to ensure consistency. After this consistency check, all the observing blocks were uploaded to the ICS and then executed on the flight hardware on ground. Some very long timeline sequences were replaced by shorter test versions for these ground tests. This procedure allowed to verify that the fully autonomous operation of the instruments by the ICS worked as expected.

The tests also included the simulation of unforeseen failures, like for example, a temporary error of an instrument. The individual instrument teams trained their capabilities of operating the instrument manually to recover it from the failure mode, and to re-join the timeline, which continued to run for the other instruments. Also, pointing control losses were simulated and efficient mitigation procedures, like safe entry points into the timeline, were implemented.

5.8. Path to Flight Readiness

CSBF requires to follow a strict procedure to achieve flight readiness[3] for zero-pressure LDB flights like SUNRISE III. The observatory needed to pass several reviews during the construction and testing phase, with the Mission Readiness Review (MRR) being the last one before the payload is being shipped to Kiruna. In the MRR, the SUNRISE team had to present, amongst others, a science status review, a deployment and integration schedule,

[3] See website of NASA's BPO: https://sites.wff.nasa.gov/code820/.

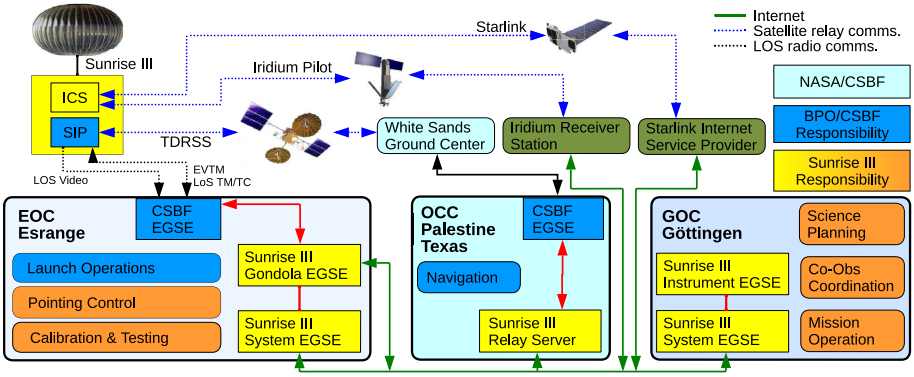


Figure 26 SUNRISE III ground segment, data flow and communication concept for the 2024 flight.

requirements for integration and operation, and to prove that the current status of the payload is ready for shipment to Esrange.

After arrival at Esrange early April 2024, the first milestone was achieved when the telescope and the PFI were mated, followed by functional tests and calibration measurements, for example, the final polarimetric calibration of the science instruments. On 01 May 2024, 'first light' was achieved: telescope and PFI were mounted in the gondola, and a hang test allowed for the first time to point the telescope towards the Sun at Esrange. In the following three weeks extensive tests of all the subsystems were performed by the SUNRISE team (timeline testing, operation training), and the CSBF hardware (e.g., SIP, antennas) for in-flight communication between observatory and ground station was installed. One week before the launch window opened on 25 May 2024, SUNRISE III completed the Science/Support Compatibility Test (SSCT). This is a final hang test to check on mission compliance with the stated requirements, and to confirm that integration is complete and SUNRISE III is ready for launch. It was followed by the Flight Readiness Review (FRR) where permission to proceed with the launch preparations was granted. Flight readiness for the 2024 flight was achieved on 21 May 2024.

5.9. Flight Operations

The 2024 flight of SUNRISE III was controlled by three flight operations centers: The flight control (i.e., launch, LoS communication, ballast control balloon venting, flight termination) was handled by CSBF from the Esrange Operations Center (EOC, Kiruna, Sweden) and the Operations Control Center (OCC) in Palestine (Texas, USA), whereas the science operations were executed from the Göttingen Operations Center (GOC). The GOC turned out to be a very efficient way to control SUNRISE III during the 2024 flight: it enabled optimum personnel support under the tight logistics situation at Esrange, caused by the dense 2024 balloon launch schedule, and it allowed to use the top-notch infrastructure of MPS. The communication between all three operations centers and the observatory in flight worked flawlessly. The operations center setup and the data flow concept is illustrated in Figure 26.

The system EGSE and all the instrument EGSEs were located at the GOC in a dedicated room at MPS. The control of the observatory was handed over from the EOC to the GOC already after first light on 01 May 2024, i.e., when the fully assembled observatory achieved sun-pointing during a hang test at Esrange. All subsequent tests, and the flight, were controlled from the GOC. It was connected via a virtual private network (VPN) to

the EOC where a second set of EGSE computers allowed for a mirrored operation of the system EGSE and all science instruments. The EOC provided the data analysis and storage computer for the scientific instruments used during their calibration and testing prior to the flight, when the produced data volume was too large for a direct transfer to the GOC. During the flight, the available data rates between balloon and ground station (see Section 4.5.4) allowed for very efficient remote operations, including the exact positioning of the telescope to the science targets using real-time thumbnails. In addition, the data from the satellite communication systems (Starlink, Iridium Pilot, TDRSS) were directly available from both operations centers.

A small flight-operations team at Esrange ensured the efficient communication between the operations centers in both, the technical aspects and the human interaction between science team and CSBF.

5.10. Fault Protection Measures

SUNRISE III was equipped with several fault protection measures, ensuring that the observatory is brought into a safe state in the case of a failure. Three important mechanical and thermal measures are briefly described here.

Aperture door: In the event of a loss of pointing, the solar image in F1 would not hit the HRW anymore, but could deposit the full radiative power collected by the main mirror M1 (≈ 1 kW) onto an element not designed to withstand this enormous power. Therefore, an emergency system was implemented, which closes the aperture door automatically when the PCS reports a loss of pointing. A curtain in the central frame in front of M1 is closed within a few seconds, fast enough to ensure that pointing loss does not cause any damage.

Survival heaters: When the temperature drops below 0 °C, survival heaters in various critical components are automatically turned on. These components include, e.g., the ICS, or the electronic units of the instruments. This case can, for example, be triggered by a failure in the unit itself, when the power consumption of the unit drops and the radiative cooling of the electronic box dominates. It can also occur when the predictions from the thermal modeling were not correct (see Section 4.7). This is likely to be the case especially during the ascent, given the unknown weather conditions and the uncontrolled spinning of the observatory. Survival heaters were added to critical components, where the thermal modeling predicted large uncertainties.

Elevation brake and hard stops: The elevation brake is a critical component during launch and landing of the observatory, holding the telescope in the safe 0°-elevation position. The strong torsional acceleration at the release from the Hercules launch vehicle caused this brake to fail during the 2022 launch. A significantly strengthened launch-lock mechanism ensured a safe launch under even harsher conditions in 2024. As an additional fault protection measure, two mechanical hard stops at $-5°$ and $+50°$ elevation ensure that the telescope stays within the clear area, to avoid damage in the case of a wrong elevation command.

However, the vast majority of fault protection measures are implemented in software. All subsystems have a plethora of fault protection code in place, reacting to out-of-bounds HK-values in an automated way. The last, very important element in the fault protection chain was the 24 h/day constant monitoring of the observatory operations and health by the ground operators.

6. Scientific Performance and Data Concept

The intensive testing of SUNRISE III in the laboratories, the hang tests and during the 2022 campaign provided insight into the scientific performance of the observatory. Here we summarize some selected parameters of the global performance of the observatory, whereas instrument specific scientific performance is described in the individual instrument sections and papers (Berkefeld et al. 2025; Feller et al. 2025; del Toro Iniesta et al. 2025; Katsukawa et al. 2025; Bernasconi et al. 2025). A detailed post-flight evaluation of the observatory performance will only be available after the data reduction phase is completed, and is intended to be published with the first scientific papers of the project.

6.1. Pointing Stability and Accuracy

Stable sun-pointing was achieved prior to the flights during the hang tests at MPS and Esrange. The performance estimates from those tests suffer from the fact that the atmospheric disturbances, the so-called "seeing", do not provide a stable and contrast-rich image of the Sun, but only a highly variable, blurry one. Nevertheless, the PCS could be tested and proved to work even under those unfavorable conditions. Surprisingly it was even possible, during the hang test at the MPS in Göttingen, to achieve closed-loop locking on a sunspot with the CWS.

At both locations, an rms jitter in the range of 1" could be achieved by using the SGT. During the 2022 flight, the azimuth pointing stability could be measured, and it exceeded the expected performance and achieved the same rms jitter (1") albeit with only the IMU of the PCS being available. The elevation pointing jitter and the expected improvement of the pointing stability using the SGT could not be tested because of the failure of the launch-lock mechanism.

Pointing accuracy, i.e., how well the telescope can be pointed at a desired target on the Sun, depends on a limb-seeking calibration routine. During hang tests on the ground, atmospheric seeing reduces the clarity of the Sun's limbs resulting in reduced absolute pointing accuracy. During those ground tests, by aiming the telescope at various prominent positions on the Sun, e.g. active regions or the solar limb, we estimated the pointing accuracy to be in the range of 10 – 15".

During the flight in 2024, the gondola PCS achieved stable sun-pointing continuously, with only one major interruption due to an unexpected avionics computer reboot. The rms pointing stability was determined to be on average better than 3", exceeding the specifications by a factor of 5. Locking on solar features with the CWS in closed loop was achieved almost continuously during the science observing programs, with a record-long time series of more than four hours at milli-arcsecond rms accuracy.

The absolute pointing accuracy of the gondola PCS, directly after performing the limb-seeking calibration, was better than the values found during the hang tests. With time, due to elevation dependence of gravitational force and thermal stress on the telescope, an offset was introduced, mainly along the elevation direction. A new limb-seeking calibration was performed when this offset in absolute pointing was larger than half the 60"-FoV of the science instruments, or when absolute pointing accuracy was crucial for the science program.

6.2. Slit Alignment

The near-space like observing conditions in the stratosphere are not only advantageous for the image quality, stability and the access to new wavelength regimes, but also for removing

the effects of differential refraction in the Earth's atmosphere, enabling the co-alignment of instruments operating at different wavelength bands. Both, SCIP and SUSI are equipped with their own slit-scanning mechanisms, allowing for a near-perfect alignment of the slits at any position within the TuMag FoV. Simultaneous spectra over long time periods in the near-IR and near-UV with sub-arcsecond alignment accuracy (0.1") over hours become possible. The slit-alignment procedure could be tested during the hang tests using the grid target in the F2 filter wheel, and was repeated during the commissioning phase of the flight. Similarly, the scan speeds for both slits were calibrated, allowing for simultaneous scans of the full FoVs of both slit instruments.

Many observing programs required strictly co-aligned scanning. Therefore, a common scan speed for both instruments was agreed upon within the SSWG during the phase of defining the observation blocks. The exact alignment of the slits and the calibration of the scan speeds was part of the in-flight calibration procedure. Using near-real-time slit-jaw images of SUSI and SCIP of the grid target in F2, which were continuously sent to the GOC through the various communication channels (see Section 4.5.4), the position of the slit could be accurately determined. The SPPT software (see Section 3.3) computed offsets and speed based on cross-correlating the two slit-jaw images.

The angle alignment of the SUSI and the SCIP slits was performed during the installation of the instruments into the PFI. A very accurate angle alignment with a difference of only 0.1° could be achieved and maintained during the flight. A preliminary assessment of the data shows that the common scanning was successful, but the detailed performance analysis and alignment accuracy can only be performed during the data reduction phase.

6.3. SUNRISE III Open-Access Data Concept

All data obtained with the SUNRISE III observatory will be treated as a public resource. The tentative schedule for the data recovery, processing, and publishing and the expected duration of the individual steps are sketched here.

(i) After landing (16 July 2024): Recovery of the DSS from the landing site in Canada and transport to MPS (duration: 1 month).
(ii) Raw-data archiving and backup to the storage servers hosted by the MPS computing center (1 month).
(iii) Data reduction: The raw data will be processed with the SUNRISE III data pipeline software to produce calibrated spectropolarimetric data (Stokes I, Q, U, and V) (3 – 6 months).
(iv) Embargo period: During this period the partner institutes and invited collaborators (e.g. co-observers) have prioritized access to the data. This period is dedicated to achieve the highest possible data quality prior to the public data release. It also allows the participating institutes to execute the scientific analysis according to their submitted ideas which formed the baseline of the observation timeline (6 months).
(v) Public release of the science-ready SUNRISE III data in the Flexible Image Transport System (FITS) file format (Wells, Greisen, and Harten 1981), accessible through a website hosted at the MPS.

According to this schedule, the date for the public release of the data of the successful SUNRISE III 2024 flight is expected for the end of 2025. However, delays in this schedule are possible. Especially the duration of step (iii) is influenced by the in-flight performance of the instruments, the telescope, and the PCS. Although the data reduction software has been prepared thoroughly, the complexity of the observations does not allow to cover all

possible effects in advance, and might even require post-calibration measurements using the flown instruments in the MPS laboratory. A delay in the data reduction process will automatically shift the public release date by the same amount. The timeline of the data reduction process and the data policy are described in the S3-DocDB document SR3-MPS-CO-GEN-002 (Lagg et al. 2021).

7. Summary and Outlook

The SUNRISE III stratospheric observatory has been designed to deepen our understanding of the magnetism and the dynamic processes of the solar atmosphere. Equipped with instrumentation of a complexity comparable to world-class ground-based solar observatories, the 1-meter aperture telescope allows to resolve solar structures as small as 60 km on the Sun. Three scientific instruments allow for diffraction limited, spectropolarimetric observations at high spectral resolution: (i) SUSI performs many-line observations in the vastly unexplored near-UV, (ii) TUMAG provides 2-dimensional maps over a FoV of 46×46 Mm^2 in the visible, and (iii) SCIP concentrates on the near-IR wavelength range.

The common goal of all three instruments is to provide highly complementary data to determine the dynamics and the magnetism in the solar atmosphere, seamlessly from the photosphere to the chromosphere in multi-hour, uninterrupted data sets with constant high resolution and quality. The diffraction limited observations reach a polarimetric sensitivity of better than 10^{-3} of the continuum intensity for all science instruments. This requires the stabilization of the telescope and the instrumentation to an accuracy of better than 0.005" rms, achieved with the combination of the 3-axis stabilized gondola Pointing Control System and an internal image stabilization system based on correlation tracking (CWS), which also controls the autofocus mechanism of the telescope and allows for an in-flight coma correction.

The science flight of SUNRISE III took place from 10 to 16 July 2024. Stratospheric winds carried the observatory on a long-distance zero-pressure balloon from Esrange Space Center in Sweden to the landing site west of Great Bear Lake (Canada) at a float altitude between 33 – 37 km in 6.5 days. The preliminary analysis of in-flight data indicates excellent performance of the observatory, exceeding the high expectations of the SUNRISE III team. A detailed performance assessment will only be possible after the completion of the data reduction phase. We hope that the rich data gathered by SUNRISE III will help to solve many mysteries of the solar atmosphere, and to discover new ones.

Appendix: Acronyms

ALMA	Atacama Large Millimeter/sub-millimeter Array
AMHD	Analog, Motor, and Heaters Drivers
AO	adaptive optics
BBSO	Big Bear Solar Observatory
BPO	Balloon Program Office
CAD	Computer Aided Design
CFRP	carbon fiber-reinforced polymers
CHASE	Chinese Hα Solar Explorer
CMOS	complementary metal oxide semiconductor
CSBF	Columbia Scientific Ballooning Facility
CT	correlation tracker

CWS	Correlating Wavefront Sensor
DKIST	Daniel K. Inouye Solar Telescope
S3-DocDB	SUNRISE III Document Database
DSS	Data Storage System
DST	Dunn Solar Telescope
EGSE	electrical ground support equipment
E-Link	Esrange Airborne Data Link
EOC	Esrange Operations Center
E-rack	electronic rack
Esrange	Esrange Space Center
EVTM	Ethernet Via Telemetry
FEM	finite element model
FITS	Flexible Image Transport System
FoV	field-of-view
fps	frames per second
FRAM	ferroelectric random access memory
FRR	Flight Readiness Review
FSM	finite state machine
FWHM	full width at half maximum
GOC	Göttingen Operations Center
GPS	Global Positioning System
GREGOR	GREGOR
GST	Goode Solar Telescope
GUSTO	Galactic/Extragalactic ULDB Spectroscopic Terahertz Observatory
HMI	Helioseismic Magnetic Imager
HRW	Heat Rejection Wedge
HVPS	high voltage power supply
IAA	Instituto de Astrofísica de Andalucía
IAC	Instituto de Astrofísica de Canarias
ICS	Instrument Control System
ICU	Instrument Control Unit
IHOP	IRIS/*Hinode* Operations Plan
IMAX	Imaging Magnetograph eXperiment
IMTEK	Department of Microsystems Engineering
IMU	Inertial Measurement Unit
INTA	Instituto Nacional de Técnica Aeroespacial
Iridium Pilot	Iridium Pilot®
IRIS-1	Image Recording Instrument for SUNRISE II
IRIS-2	Image Recording Instrument for SUNRISE III
IRIS	Interface Region Imaging Spectrograph
ISLID	Image Stabilization and Light Distribution unit
JAXA	Japan Aerospace Exploration Agency
APL	Johns Hopkins University Applied Physics Laboratory
KBSI	Korea Basic Science Institute
KIS	Institut für Sonnenphysik
LCVR	liquid crystal variable retarder
LDB	long-distance balloon
LED	light-emitting diode
LLDPE	linear low-density polyethylene

LoS	line-of-sight
LTE	local thermodynamic equilibrium
MAST	Multi-Application Solar Telescope
MHD	magneto-hydrodynamic
MIT	Massachusetts Institute of Technology
MLI	multilayer insulation
MPAe	Max-Planck-Institut für Aeronomie
MPS	Max Planck Institute for Solar System Research
MRR	Mission Readiness Review
MTC	Main Telescope Controller
MTU	Momentum Transfer Unit
MURaM-ChE	MURaM Chromospheric Extension
MURaM	MPS/University of Chicago Radiative MHD
NAOJ	National Astronomical Observatory of Japan
NASA	National Aeronautics and Space Administration
NIC	network interface controller
near-IR	near-infrared
non-LTE	non-local thermodynamic equilibrium
near-UV	near-ultraviolet
NVST	New Vacuum Solar Telescope
OCC	Operations Control Center
OLR	outgoing longwave radiation
PBS	polarising beam-splitter
PCB	printed circuit board
PDU	Power Distribution Unit
PFI	Post Focus Instrumentation
PHI	Polarimetric and Helioseismic Imager
PMU	Polarization Modulation Unit
PoE	Power over Ethernet
PPD	PFI Power Distribution Unit
PSG	Polarization State Generator
PSF	point spread function
PCS	Pointing Control System
HK	housekeeping
RAMON	RAdiation MONitor
rms	root-mean-square
RTC	real-time clock
S/N	signal-to-noise
S^3PC	Spanish Space Solar Physics Consortium
SCIP	SUNRISE Chromospheric Infrared spectro-Polarimeter
SDO	Solar Dynamics Observatory
SGT	Sun Guider Telescope
SiPM	Silicon PhotoMultiplier
SIP	Support Instrumentation Package
SMART	Solar Magnetic Activity Research Telescope
SMM	scan mirror mechanism
Solar Orbiter	Solar Orbiter
NFI	Narrowband Filter Imager
SP	Spectro-Polarimeter

SOT	Solar Optical Telescope
SPGCam	Solar Physics Group Camera
SSCT	Science/Support Compatibility Test
SSC	Swedish Space Corporation
SSD	solid state disk
SSM	second surface mirror
SST	Swedish Solar Telescope
SSWG	SUNRISE Science Working Group
SS	Science Stack
Starlink	Starlink (a division of SpaceX)
SUFI	SUNRISE Filter Imager
SPPT	SUNRISE III Science Planning and Pointing Tool
SUSI	SUNRISE UV Spectropolarimeter and Imager
SUIT	Solar Ultraviolet Imaging Telescope
SUVI	Solar Ultraviolet Imager
SUTRI	Solar Upper Transition Region Imager
TC	Telecommand
TDRSS	Tracking & Data Relay Satellite System
TM/TC	Telemetry and Telecommand
TM	Telemetry
TUMAG	Tunable Magnetograph
TV	thermal-vacuum
UV	Universitat de València
UPM	Universidad Politécnica de Madrid
USAF	U.S. Air Force
UV	ultraviolet
VDA	vapor deposited aluminum
VPN	virtual private network
VTT	German Vacuum Tower Telescope
WFS	wavefront sensor

Acknowledgments We thank the Max Planck Society for the financial support. A special thanks goes to the Max-Planck-Förderstiftung, especially to Frau Pfündl, Frau Philipp and Prof. Pöllath, for their enthusiasm for SUNRISE III and the generous funding of this research. We thank the employees of CSBF and Esrange / SSC for their support and hospitality during the launch campaigns. We warmly thank the kind and professional help of the personnel at Calar Alto Astronomical Observatory (Spain) who re-aluminized the SUNRISE mirrors. We are grateful to C. Müller and M. Wölfle of IMTEK (Freiburg, Germany) for excellent technical support in diamond milling of the HRW, and Mike Smith from Aerostar International (TX, USA) for the excellent support during the 2024 campaign for providing the wind shield film for the E-rack and the PFI.

Author Contributions Korpi-Lagg, Andreas: main author; Álvarez-Alonso, María-Teresa: design, building, testing, operating RAMON; Álvarez-Herrero, Alberto: Sunrise III CoI, TuMag optical unit; Álvarez García, Daniel: TuMag/SCIP AMHD HW/FW design and TuMag/SCIP cameras HW design ; Aparicio del Moral, Beatriz: TuMag/SCIP firmware design and testing; Atiénzar, Julia: TuMag E2E; Ayoub, Daniel: Gondola mission operations; Bailén, Francisco Javier: TuMag: camera assembly and testing, on-ground and in-flight wavefront calibration, instrument verification, data reduction; Bailón Martínez, Eduardo: TuMag/SCIP ground segment design; Balaguer Jiménez, Maria: TuMaG and S3PC contribution to SCIP project management; Barthol, Peter: science support; Bayon Laguna, Montserrat: mecahnical and thermal engineering; Bell, Alexander: Sunrise III CoI, CWS software and operation; Bellot Rubio, Luis R.: TuMag coI, scientific contribution; Bergmann, Melani: thermal hardware; Berkefeld, Thomas: Sunrise III Lead-CoI, writing of CWS section; Bernasconi, Pietro: Sunrise III Lead-CoI, writing of gondola section; Blanco Rodríguez, Julian: TuMag CoI; TuMagsm developer, scientific contribution; Bochmann, Jan: mechanical engineering; Borrero, Juan Manuel: Science working group, science section; Campos-Jara, Antonio: TuMag polarimetric calibration and testing;

Carpenter, Michael: Sunrise III CoI, gondola design, setup, testing; Castellanos Durán, Juan Sebastián: scientific planning and operation; Cebollero, María: TuMag AIV coordination; Conde Rodríguez, Aitor: design, building, testing, operating IRIS-2; del Toro Iniesta, Jose Carlos: Sunrise III Lead-CoI, writing of TuMag section; Deutsch, Werner: Sunrise III lead engineer; Eaton, Harry: Gondola pointing control system lead; Feller, Alex: Sunrise III Lead-CoI, writing of SUSI section; Fernández-Medina, Ana Belen: TuMag optical unit project management and system engineering; Fernandez-Rico, German: thermal design and analysis, writing of thermal section; Ferreres, Agustin: TuMag/SCIP: PCM design and simulation; Gandorfer, Achim: Sunrise III project scientist, section telescope, PFI; García, Andrés: design, building, testing, operating RAMON; García Alarcia, Ramón María: design, building, testing, operating IRIS-2; García Parejo, Pilar: TuMag polarimetric calibration and testing; Garranzo-García, Daniel: TuMag optical Unit AIV, verification and testing; Gasent Blesa, José Luis: TuMag/SCIP: project management, PCM and E-Unit mechanical design, MAIV; Gerber, Karin: CWS: workshop management; Germerott, Dietmar: network and communication chapter; Gilabert Palmer, David: TuMag/SCIP: PCM design and testing; Gizon, Laurent: project support; Gómez Sánchez-Tirado, Miguel Ángel: design, building, testing, operating IRIS-2; González-Bárcena, David: TuMag thermal analysis and design; Gonzalo Melchor, Alejandro: TuMag Optical Unit thermomechanical design/analysis and testing; Goodyear, Sam: electrical engineer; Grauf, Bianca: Sunrise III CoI, optical design, setup and testing; Hara, Hirohisa: SCIP mechanical and thermal design and AITV; Harnes, Edvarda: science operations; Heerlein, Klaus: camera design and electronics, software; Heidecke, Frank: CWS: E-Unit design and AIV; Heinrichs, Jan: mechanical engineer; Hernández Expósito, David: TuMag/SCIP DPU firmware design; Hirzberger, Johann: scienc planning; Hoelken, Johannes: Timelines, SUSI operation and data reduction; Hyun, Sangwon: PFI mirror contribution; Iglesias, Francisco A.: SUSI: camera design and validation, polarimetric calibration, instrument validation, flight calibration and operation, data reduction; Ishikawa, Ryohtaroh T.: SCIP operation, coordination with Hinode/IRIS, and calibration; Jeon, Minwoo: PFI mirror contribution; Katsukawa, Yukio: Sunrise III Lead-CoI, writing of SCIP section; Kawabata, Yusuke: SCIP optical AITV, polarization calibration, operation; Kolleck, Martin: system software; Kubo, Masahito: Sunrise III CoI, SCIP science and hardware; Laguna, Hugo: TuMag, Electro-optical engineer, Harness design and testing, Electronic AIV; Lomas, Julian: design, building, testing, operating RAMON; López Jiménez, Antonio C.: Design of High Voltage Power Supply and harness of TUMag and SCIP; Manzano, Paula: design, building, testing, operating RAMON; Martínez Pillet, Valentín: Sunrise III CoI (NSO), scientific contribution; Matsumoto, Takuma: SCIP numerical modeling, operation, and calibration; Mayo Turrado, David: design, building, testing, operating IRIS-2; Meierdierks, Thimo: mechanical engineer; Meining, Stefan: optical engineer; Monecke, Markus: mechanical engineer; Morales-Fernández, José Miguel: TuMag/SCIP firmware design and testing; Moreno Mantas, Antonio Jesús: TuMag/SCIP DPU design and testing; Moreno Vacas, Alejandro: TuMag: scientific contribution; Müller, Marc Ferenc: system harness; Müller, Reinhard: motor controllers, central data unit design; Naito, Yoshihiro: SCIP operation and calibration ; Nakai, Eiji: CWS: thermal vacuum testing and documentation ; Núñez Peral, Armonía: TuMag optical design, setup and testing; Oba, Takayoshi: development of scan mirror for SCIP, science operations; Orozco Suárez, David: Sunrise III CoI, TuMag and S3PC contribution to SCIP project scientist; Palo, Geoffrey: Gondola integration and testing, mission operations; Pérez-Grande, Isabel: Sunrise thermal design; Piqueras Carreño, Javier: Thermal design and analysis; Preis, Tobias: CWS: E-Unit design and AIV; Przybylski, Damien: science section writing; Quintero Noda, Carlos: scientific support; Ramanath, Sandeep: testing, QA, T; Ramos Más, Jose Luis: TuMag/SCIP DPU design and testing; Raouafi, Nour: Scientific support; Riethmüller, Tino L.: Sunrise III Lead-CoI, writing of Data section; Rivas-Martínez, María-Jesús: design, building, testing, operating RAMON; Rodríguez Martínez, Pedro: TuMag/SCIP: Mechanical design and structural analysis; Rodríguez Valido, Manuel: TuMag/SCIP camera firmware FPGA design and testing; Ruiz Cobo, Basilio: TuMag coI: scientific contribution; Sánchez Rodríguez, Antonio: TuMag Optical Unit mechanical design and testing; Sanchez Toledo, Mariano: HK analysis, observation overview; Sánchez Gómez, Antonio: TuMag/SCIP software design and testing; Sanchis Kilders, Esteban: TuMag/SCIP CoI; PCM design, review and analysis; Sant, Kamal: camera characterization; Santamarina Guerrero, Pablo: TuMag data reduction pipeline; Schulze, Erich: Gondola lead mechanical engineer and integration and testing support; Shimizu, Toshifumi: SCIP: development of polarization modulator unit and slit scan mirror mechanism; Silva-López, Manuel: TuMag spectroscopic calibration and testing; Singh, Kunal: Housekeeping Analysis; Siu-Tapia, Azaymi L.: TuMag coI, scientific contribution; Smitha, H. N.: Sunrise III CoI, science planning ; Solanki, Sami K.: Sunrise III PI, science section; Sonner, Thomas: CWS: O-Unit mechanics design and assembly; Staub, Jan: mechanical design; Strecker, Hanna: TuMag coI, scientific contribution; Tobaruela, Angel: TuMag/SCIP harness, elelctronics AIV; Torralbo, Ignacio: Thermal Design and Engineering; Tritschler, Alexandra: Scientific support; Tsuzuki, Toshihiro: SCIP optical design and analysis; Uraguchi, Fumihiro: SCIP mechanical design and analysis; Volkmer, Reiner: CWS: project management, thermal vacuum testing; Vourlidas, Angelos: Scientific support and lead SECCHI coordinated observation campaig for Sunrise III; Vukadinović, Dušan: science operations; Werner, Stephan: development SUSI controller; Zerr, Andreas: electronic systems;

Funding Information Open Access funding enabled and organized by Projekt DEAL. SUNRISE III is supported by funding from the Max-Planck-Förderstiftung (Max Planck Foundation), NASA under Grant #80NSSC18K0934 and #80NSSC24M0024 ("Heliophysics Low Cost Access to Space' program), and the ISAS/JAXA Small Mission-of-Opportunity program and JSPS KAKENHI JP18H05234/JP23H01220. This research has received financial support from the European Union's Horizon 2020 research and innovation program under grant agreement No. 824135 (SOLARNET) and No. 101097844 (WINSUN) from the European Research Council (ERC). It has also been funded by the Deutsches Zentrum für Luft- und Raumfahrt e.V. (DLR, grant no. 50 OO 1608). The Spanish contributions have been funded by the Spanish MCIN/AEI under projects RTI2018-096886-B-C5, and PID2021-125325OB-C5, and from "Center of Excellence Severo Ochoa" awards to IAA-CSIC (SEV-2017-0709, CEX2021-001131-S), all co-funded by European REDEF funds, "A way of making Europe".

D. Orozco Suárez acknowledges financial support from a *Ramón y Cajal* fellowship. The contributions of J. Hölken, D. Vukadinović, E. Harnes and K. Sant have been supported by the International Max Planck Research School for Solar System Science at the University of Göttingen (IMPRS), Germany. F. A. Iglesias is a member of the "Carrera del Investigador Científico" of CONICET and supported by MPS through the Max Planck Partner Group between MPS and the University of Mendoza, Argentina. The research activities and the flight operation of the SCIP team members, R. T. Ishikawa, M. Kubo, Y. Kawabata, and T. Oba, have been supported from the JSPS KAKENHI grants No. 23KJ0299, No. 24K07105, No. 23K13152, and No. 21K13972, respectively.

Data Availability No datasets were generated or analysed during the current study.

Declarations

Competing Interests The authors declare no competing interests.

Open Access This article is licensed under a Creative Commons Attribution 4.0 International License, which permits use, sharing, adaptation, distribution and reproduction in any medium or format, as long as you give appropriate credit to the original author(s) and the source, provide a link to the Creative Commons licence, and indicate if changes were made. The images or other third party material in this article are included in the article's Creative Commons licence, unless indicated otherwise in a credit line to the material. If material is not included in the article's Creative Commons licence and your intended use is not permitted by statutory regulation or exceeds the permitted use, you will need to obtain permission directly from the copyright holder. To view a copy of this licence, visit http://creativecommons.org/licenses/by/4.0/.

References

Álvarez Herrero, A., Garranzo-García, D., Núnez, A., Silva-López, M., Campos-Jara, A., García Parejo, P., Cebollero, M., Atiénzar, J., Bailén, F.J., Blanco Rodríguez, J., Santamarina, P., Orozco Suárez, D., del Toro Iniesta, J.C.: 2022, End-to-end tests of the TuMag instrument for the SUNRISE III mission. In: Evans, C.J., Bryant, J.J., Motohara, K. (eds.) *Ground-Based and Airborne Instrumentation for Astronomy IX*, *Society of Photo-Optical Instrumentation Engineers (SPIE) Conference Series* **12184**, 121842F. DOI. ADS.

Álvarez-Herrero, A., Parejo, P.G., Silva-López, M.: 2018, Fine tuning method for optimization of liquid crystal based polarimeters. *Opt. Express* **26**, 12038. DOI. https://opg.optica.org/oe/abstract.cfm?URI=oe-26-9-12038.

Anderson, L.S., Athay, R.G.: 1989, Chromospheric and coronal heating. *Astrophys. J.* **336**, 1089. DOI. ADS.

Anusha, L.S., Solanki, S.K., Hirzberger, J., Feller, A.: 2017, Statistical evolution of quiet-Sun small-scale magnetic features using Sunrise observations. *Astron. Astrophys.* **598**, A47. DOI. ADS.

Bai, X., Tian, H., Deng, Y., Wang, Z., Yang, J., Zhang, X., Zhang, Y., Qi, R., Wang, N., Gao, Y., Yu, J., He, C., Shen, Z., Shen, L., Guo, S., Hou, Z., Ji, K., Bi, X., Duan, W., Yang, X., Lin, J., Hu, Z., Song, Q., Yang, Z., Chen, Y., Qiao, W., Ge, W., Li, F., Jin, L., He, J., Chen, X., Zhu, X., He, J., Shi, Q., Liu, L., Li, J., Xu, D., Liu, R., Li, T., Feng, Z., Wang, Y., Fan, C., Liu, S., Guo, S., Sun, Z., Wu, Y., Li, H., Yang, Q., Ye, Y., Gu, W., Wu, J., Zhang, Z., Yu, Y., Ye, Z., Sheng, P., Wang, Y., Li, W., Huang, Q., Zhang, Z.: 2023, The Solar Upper Transition Region Imager (SUTRI) onboard the SATech-01 satellite. *Res. Astron. Astrophys.* **23**, 065014. DOI. ADS.

Bailén, F.J., Orozco Suárez, D., Blanco Rodríguez, J., del Toro Iniesta, J.C.: 2022a, Optimal defocus for phase diversity wave front retrieval. *Astrophys. J. Suppl. Ser.* **263**, 8. DOI. ADS.

Bailén, F.J., Orozco Suárez, D., Blanco Rodríguez, J., del Toro Iniesta, J.C.: 2022b, Performance of sequential phase diversity with dynamical solar scenes. *Astrophys. J. Suppl. Ser.* **263**, 7. DOI.

Barthol, P., Gandorfer, A., Solanki, S.K., Schüssler, M., Chares, B., Curdt, W., Deutsch, W., Feller, A., Germerott, D., Grauf, B., Heerlein, K., Hirzberger, J., Kolleck, M., Meller, R., Müller, R., Riethmüller, T.L., Tomasch, G., Knölker, M., Lites, B.W., Card, G., Elmore, D., Fox, J., Lecinski, A., Nelson, P., Summers, R., Watt, A., Martínez Pillet, V., Bonet, J.A., Schmidt, W., Berkefeld, T., Title, A.M., Domingo, V., Gasent Blesa, J.L., Del Toro Iniesta, J.C., López Jiménez, A., Álvarez-Herrero, A., Sabau-Graziati, L., Widani, C., Haberler, P., Härtel, K., Kampf, D., Levin, T., Pérez Grande, I., Sanz-Andrés, A., Schmidt, E.: 2011, The Sunrise mission. *Sol. Phys.* **268**, 1. DOI. ADS.

Bellot Rubio, L., Orozco Suárez, D.: 2019, Quiet Sun magnetic fields: an observational view. *Living Rev. Sol. Phys.* **16**, 1. DOI. ADS.

Berkefeld, T., Schmidt, W., Soltau, D., Bell, A., Doerr, H.P., Feger, B., Friedlein, R., Gerber, K., Heidecke, F., Kentischer, T., v. d. Lühe, O., Sigwarth, M., Wälde, E., Barthol, P., Deutsch, W., Gandorfer, A., Germerott, D., Grauf, B., Meller, R., Álvarez-Herrero, A., Knölker, M., Martínez Pillet, V., Solanki, S.K., Title, A.M.: 2011, The wave-front correction system for the Sunrise balloon-borne Solar Observatory. *Sol. Phys.* **268**, 103. DOI. ADS.

Berkefeld, T., Bell, A., Volkmer, R., Heidecke, F., Preis, T., Sonner, T., Nakai, E., Borrero, J.M., Korpi-Lagg, A., Gandorfer, A., Solanki, S.K., del Toro Iniesta, J.C., Katsukawa, Y., Bernasconi, P., Feller, A., Riethmüller, T.L., Álvarez-Herrero, A., Kubo, M., Martínez Pillet, V., Smitha, S., Orozco Suárez, D., Grauf, B., Carpenter, M.: 2025, Sunrise III: the Wavefront Correction System. *Sol. Phys.* **300**. Part of the Topical Collection "The Sunrise III Solar Observatory".

Bernasconi, P., Carpenter, M., Eaton, H., Schulze, E., Carkhuff, B., Palo, G., Young, D., Raouafi, N., Vourlidas, A., Coker, R., Solanki, S.K., Korpi-Lagg, A., Gandorfer, A., Feller, A., Riethmüller, T.L., Smitha, H.N., Grauf, B., del Toro Iniesta, J.C., Suárez, D.O., Katsukawa, Y., Kubo, M., Berkefeld, T., Bell, A., Álvarez-Herrero, A., Martínez Pillet, V.: 2025, The Gondola for the Sunrise III balloon-borne Solar Observatory. *Sol. Phys.* **300**. Part of the Topical Collection "The Sunrise III Solar Observatory".

Borrero, J.M., Jafarzadeh, S., Schüssler, M., Solanki, S.K.: 2017, Solar magnetoconvection and small-scale dynamo. Recent developments in observation and simulation. *Space Sci. Rev.* **210**, 275. DOI. ADS.

Brian Alvarez, E., Eaton, H.A., Carpenter, M.S., Carkhuff, B.G., Bernasconi, P.N.: 2023, APL's contributions to stratospheric ballooning for space science. *Johns Hopkins APL Tech. Dig.* **36**, 363. https://secwww.jhuapl.edu/techdigest/Content/techdigest/pdf/V36-N04/36-04-Alvarez.pdf.

Buehler, D., Lagg, A., Solanki, S.K.: 2013, Quiet Sun magnetic fields observed by Hinode: support for a local dynamo. *Astron. Astrophys.* **555**, A33. DOI. ADS.

Cameron, R., Vögler, A., Schüssler, M.: 2011, Decay of a simulated mixed-polarity magnetic field in the solar surface layers. *Astron. Astrophys.* **533**, A86. DOI. ADS.

Cao, W., Gorceix, N., Coulter, R., Ahn, K., Rimmele, T.R., Goode, P.R.: 2010, Scientific instrumentation for the 1.6 m new solar telescope in Big Bear. *Astron. Nachr.* **331**, 636. DOI. ADS.

Carlsson, M., De Pontieu, B., Hansteen, V.H.: 2019, New view of the solar chromosphere. *Annu. Rev. Astron. Astrophys.* **57**, 189. DOI. ADS.

Cattaneo, F.: 1999, On the origin of magnetic fields in the quiet photosphere. *Astrophys. J. Lett.* **515**, L39. DOI. ADS.

Centeno, R., Socas-Navarro, H., Lites, B., Kubo, M., Frank, Z., Shine, R., Tarbell, T., Title, A., Ichimoto, K., Tsuneta, S., Katsukawa, Y., Suematsu, Y., Shimizu, T., Nagata, S.: 2007, Emergence of small-scale magnetic loops in the quiet-Sun internetwork. *Astrophys. J. Lett.* **666**, L137. DOI. ADS.

Centeno, R., Blanco Rodríguez, J., Del Toro Iniesta, J.C., Solanki, S.K., Barthol, P., Gandorfer, A., Gizon, L., Hirzberger, J., Riethmüller, T.L., van Noort, M., Orozco Suárez, D., Berkefeld, T., Schmidt, W., Martínez Pillet, V., Knölker, M.: 2017, A tale of two emergences: Sunrise II observations of emergence sites in a solar active region. *Astrophys. J. Suppl. Ser.* **229**, 3. DOI. ADS.

Charbonneau, P., Sokoloff, D.: 2023, Evolution of solar and stellar dynamo theory. *Space Sci. Rev.* **219**, 35. DOI. ADS.

Chen, F., Rempel, M., Fan, Y.: 2017, Emergence of magnetic flux generated in a solar convective dynamo. I. The formation of sunspots and active regions and the origin of their asymmetries. *Astrophys. J.* **846**, 149. DOI. ADS.

Cheung, M.C.M., Isobe, H.: 2014, Flux emergence (theory). *Living Rev. Sol. Phys.* **11**, 3. DOI. ADS.

Chitta, L.P., Peter, H., Solanki, S.K., Barthol, P., Gandorfer, A., Gizon, L., Hirzberger, J., Riethmüller, T.L., van Noort, M., Blanco Rodríguez, J., Del Toro Iniesta, J.C., Orozco Suárez, D., Schmidt, W., Martínez Pillet, V., Knölker, M.: 2017, Solar coronal loops associated with small-scale mixed polarity surface magnetic fields. *Astrophys. J. Suppl. Ser.* **229**, 4. DOI. ADS.

Chitta, L.P., Peter, H., Priest, E.R., Solanki, S.K.: 2020, Impulsive coronal heating during the interaction of surface magnetic fields in the lower solar atmosphere. *Astron. Astrophys.* **644**, A130. DOI. ADS.

Chitta, L.P., Peter, H., Parenti, S., Berghmans, D., Auchère, F., Solanki, S.K., Aznar Cuadrado, R., Schühle, U., Teriaca, L., Mandal, S., Barczynski, K., Buchlin, É., Harra, L., Kraaikamp, E., Long, D.M., Rodriguez, L., Schwanitz, C., Smith, P.J., Verbeeck, C., Zhukov, A.N., Liu, W., Cheung, M.C.M.: 2022, Solar coronal heating from small-scale magnetic braids. *Astron. Astrophys.* **667**, A166. DOI. ADS.

Cirtain, J.W., Golub, L., Winebarger, A.R., de Pontieu, B., Kobayashi, K., Moore, R.L., Walsh, R.W., Korreck, K.E., Weber, M., McCauley, P., Title, A., Kuzin, S., Deforest, C.E.: 2013, Energy release in the solar corona from spatially resolved magnetic braids. *Nature* **493**, 501. DOI. ADS.

da Silva Santos, J.M., Danilovic, S., Leenaarts, J., de la Cruz Rodríguez, J., Zhu, X., White, S.M., Vissers, G.J.M., Rempel, M.: 2022, Heating of the solar chromosphere through current dissipation. *Astron. Astrophys.* **661**, A59. DOI. ADS.

Danilovic, S., Schüssler, M., Solanki, S.K.: 2010a, Magnetic field intensification: comparison of 3D MHD simulations with Hinode/SP results. *Astron. Astrophys.* **509**, A76. DOI. ADS.

Danilovic, S., Schüssler, M., Solanki, S.K.: 2010b, Probing quiet Sun magnetism using MURaM simulations and Hinode/SP results: support for a local dynamo. *Astron. Astrophys.* **513**, A1. DOI. ADS.

Danilovic, S., Beeck, B., Pietarila, A., Schüssler, M., Solanki, S.K., Martínez Pillet, V., Bonet, J.A., del Toro Iniesta, J.C., Domingo, V., Barthol, P., Berkefeld, T., Gandorfer, A., Knölker, M., Schmidt, W., Title, A.M.: 2010, Transverse component of the magnetic field in the solar photosphere observed by SUNRISE. *Astrophys. J. Lett.* **723**, L149. DOI. ADS.

Danilovic, S., Rempel, M., van Noort, M., Cameron, R.: 2016, Observed and simulated power spectra of kinetic and magnetic energy retrieved with 2D inversions. *Astron. Astrophys.* **594**, A103. DOI. ADS.

Darnel, J.M., Seaton, D.B., Bethge, C., Rachmeler, L., Jarvis, A., Hill, S.M., Peck, C.L., Hughes, J.M., Shapiro, J., Riley, A., Vasudevan, G., Shing, L., Koener, G., Edwards, C., Mathur, D., Timothy, S.: 2022, The GOES-R Solar UltraViolet Imager. *Space Weather* **20**, e2022SW003044. DOI. ADS.

de la Cruz Rodríguez, J., Leenaarts, J.: 2024, Improved reconstruction of solar magnetic fields from imaging spectropolarimetry through spatio-temporal regularisation. arXiv e-prints. arXiv. ADS.

de la Cruz Rodríguez, J., van Noort, M.: 2017, Radiative diagnostics in the solar photosphere and chromosphere. *Space Sci. Rev.* **210**, 109. DOI. ADS.

De Pontieu, B., Title, A.M., Lemen, J.R., Kushner, G.D., Akin, D.J., Allard, B., Berger, T., Boerner, P., Cheung, M., Chou, C., Drake, J.F., Duncan, D.W., Freeland, S., Heyman, G.F., Hoffman, C., Hurlburt, N.E., Lindgren, R.W., Mathur, D., Rehse, R., Sabolish, D., Seguin, R., Schrijver, C.J., Tarbell, T.D., Wülser, J.-P., Wolfson, C.J., Yanari, C., Mudge, J., Nguyen-Phuc, N., Timmons, R., van Bezooijen, R., Weingrod, I., Brookner, R., Butcher, G., Dougherty, B., Eder, J., Knagenhjelm, V., Larsen, S., Mansir, D., Phan, L., Boyle, P., Cheimets, P.N., DeLuca, E.E., Golub, L., Gates, R., Hertz, E., McKillop, S., Park, S., Perry, T., Podgorski, W.A., Reeves, K., Saar, S., Testa, P., Tian, H., Weber, M., Dunn, C., Eccles, S., Jaeggli, S.A., Kankelborg, C.C., Mashburn, K., Pust, N., Springer, L., Carvalho, R., Kleint, L., Marmie, J., Mazmanian, E., Pereira, T.M.D., Sawyer, S., Strong, J., Worden, S.P., Carlsson, M., Hansteen, V.H., Leenaarts, J., Wiesmann, M., Aloise, J., Chu, K.-C., Bush, R.I., Scherrer, P.H., Brekke, P., Martinez-Sykora, J., Lites, B.W., McIntosh, S.W., Uitenbroek, H., Okamoto, T.J., Gummin, M.A., Auker, G., Jerram, P., Pool, P., Waltham, N.: 2014, The Interface Region Imaging Spectrograph (IRIS). *Sol. Phys.* **289**, 2733. DOI. ADS.

del Toro Iniesta, J.C., Orozco Suárez, D., Álvarez-Herrero, A., Sanchis Kilders, E., Pérez-Grande, I., Ruiz Cobo, B., Bellot Rubio, L.R., Balaguer Jiménez, M., López Jiménez, A.C., Álvarez García, D., Ramos Más, J.L., Cobos Carrascosa, J.P., Labrousse, P., Moreno Mantas, A.J., Morales-Fernández, J.M., Aparicio del Moral, B., Sánchez Gómez, A., Bailón Martínez, E., Bailén Martínez, F.J., Strecker, H., Siu-Tapia, A.L., Santamarina Guerrero, P., Moreno Vacas, A., Atiénzar García, J., Dorantes Monteagudo, A.J., Bustamante, I., Tobaruela, A., Fernández-Medina, A.B., Núñez Peral, A., Cebollero, M., Garranzo-García, D., García Parejo, P., Gonzalo Melchor, A., Sánchez Rodríguez, A., Campos-Jara, A., Laguna, H., Silva-López, M., Blanco Rodríguez, J., Gasent Blesa, J.L., Rodríguez Martínez, P., Ferreres, A., Gilabert Palmer, D., Torralbo, I., Piqueras, J., González-Bárcena, D., Fernándes, A.J., Hernández Expósito, D., Páez Mañá, E., Magdaleno Castillo, E., Rodríguez Valido, M., Korpi-Lagg, A., Gandorfer, A., Solanki, S.K., Berkefeld, T., Bernasconi, P., Feller, A., Katsukawa, Y., Riethmüller, T.L., Smitha, H.N., Kubo, M., Martínez Pillet, V., Grauf, B., Bell, A., Carpenter, M.: 2025, TuMag: the tunable magnetograph for the Sunrise III mission. *Sol. Phys.* **300**. Part of the Topical Collection "The Sunrise III Solar Observatory".

Eberhardt, M.: 2021, ISLiD E-Unit FM and F2 Filter Wheel FM Test Report. Sunrise iii document database, MPS. https://www.mps.mpg.de/solar-physics/sunrise/documents.

Ebert, E., Milic, I., Borrero, J.M.: 2024, Solar internetwork magnetic fields: Statistical comparison between observations and MHD simulations. arXiv e-prints. arXiv. ADS.

Feller, A., Gandorfer, A., Iglesias, F.A., Lagg, A., Riethmüller, T.L., Solanki, S.K., Katsukawa, Y., Kubo, M.: 2020, The SUNRISE UV spectropolarimeter and imager for SUNRISE III. In: Evans, C.J., Bryant, J.J., Motohara, K. (eds.) *Ground-Based and Airborne Instrumentation for Astronomy VIII* **11447**, SPIE, Bellingham, 2260. DOI.

Feller, A., Gandorfer, A., Grauf, B., Hölken, J., Iglesias, F.A., Korpi-Lagg, A., Riethmüller, T.L., Staub, J., Fernandez-Rico, G., Castellanos Durán, J.S., Solanki, S.K., Smitha, H.N., Sant, K., Barthol, P., Bayon Laguna, M., Bergmann, M., Bischoff, J., Bochmann, J., Bruns, S., Deutsch, W., Eberhardt, M., Enge, R., Goodyear, S., Heerlein, K., Heinrichs, J., Hirche, D., Meining, S., Mende, R., Meyer, S., Mühlhaus, M., Müller, M.F., Monecke, K., Oberdorfer, D., Papagiannaki, I., Ramanath, S., Vergöhl, M., Vukadinović, D., Werner, S., Zerr, K., Bell, A., Berkefeld, T., Bernasconi, P., Carpenter, M., Katsukawa, Y., del Toro Iniesta, J.C., Álvarez Herrero, A., Kubo, M., Martínez Pillet, V., Orozco Suárez, D.: 2025, The Sunrise Ultraviolet Spectropolarimeter and Imager (SUSI): Instrument description. *Sol. Phys.* **300**. Part of the Topical Collection "The Sunrise III Solar Observatory".

Fernández-Medina, A., Frövel, M., López Heredero, R., Belenguer, T., de la Torre, A., Moravec, C., San Julián, R., Gonzalo, A., Cebollero, M., Álvarez-Herrero, A.: 2023, Embedded fiber Bragg grating sensors for monitoring temperature and thermo-elastic deformations in a carbon fiber optical bench. *Sensors* **23**, 6499. DOI. https://www.mdpi.com/1424-8220/23/14/6499.

Fernández-Soler, A., González-Bárcena, D., Torralbo-Gimeno, I., Pérez-Grande, I.: 2023, Ascent phase convective heat transfer of a stratospheric-balloon-borne payload. *Adv. Space Res.* **72**, 503. DOI. ADS.

Fontenla, J.M., Avrett, E.H., Loeser, R.: 1993, Energy balance in the solar transition region. III. Helium emission in hydrostatic, constant-abundance models with diffusion. *Astrophys. J.* **406**, 319. DOI. ADS.

Gandorfer, A.: 2005, *The Second Solar Spectrum: A High Spectral Resolution Polarimetric Survey of Scattering Polarization at the Solar Limb in Graphical Representation. Volume III: 3160 Å to 3915 Å*. vdf Hochschulverlag AG an der ETH Zürich. ADS.

Gandorfer, A., Grauf, B., Barthol, P., Riethmüller, T.L., Solanki, S.K., Chares, B., Deutsch, W., Ebert, S., Feller, A., Germerott, D., Heerlein, K., Heinrichs, J., Hirche, D., Hirzberger, J., Kolleck, M., Meller, R., Müller, R., Schäfer, R., Tomasch, G., Knölker, M., Martínez Pillet, V., Bonet, J.A., Schmidt, W., Berkefeld, T., Feger, B., Heidecke, F., Soltau, D., Tischenberg, A., Fischer, A., Title, A., Anwand, H., Schmidt, E.: 2011, The filter imager SuFI and the Image Stabilization and Light Distribution system ISLiD of the Sunrise balloon-borne Observatory: instrument description. *Sol. Phys.* **268**, 35. DOI. ADS.

Georgoulis, M.K., Rust, D.M., Bernasconi, P.N., Schmieder, B.: 2002, Statistics, morphology and energetics of Ellerman bombs. *Astrophys. J.* **575**, 506. DOI. ADS.

Gizon, L., Birch, A.C.: 2005, Local helioseismology. *Living Rev. Sol. Phys.* **2**, 6. DOI. ADS.

Gizon, L., Birch, A.C., Spruit, H.C.: 2010, Local helioseismology: three-dimensional imaging of the solar interior. *Annu. Rev. Astron. Astrophys.* **48**, 289. DOI. ADS.

Goldsmith, P., Walker, C., Kulesa, C., Bernasconi, P., Tielens, A., Wolfire, M., Melnick, G., Hollenbach, D., Seo, Y., Shipman, R., Neufeld, D., Groppi, C., Tolls, V., Young, E., Stark, A., Yorke, H., Pineda, J., Kawamura, J.: 2022, GUSTO — the Galactic/Extragalactic Spectroscopic Terahertz Observatory. In: *American Astronomical Society Meeting #240*, *American Astronomical Society Meeting Abstracts* **54**, 333.01. ADS.

González-Bárcena, D., González-Llana, A., Grande, I., Sanz-Andres, A.: 2019, Parametric worst case thermal environment conditions selection for polar summer long duration balloon missions. In: *24th ESA Symposium on European Rocket and Balloon Programmes and Related Research*.

González-Bárcena, D., Fernández-Soler, A., Pérez-Grande, I., Sanz-Andrés, Á.: 2020, Real data-based thermal environment definition for the ascent phase of polar-summer long duration balloon missions from Esrange (Sweden). *Acta Astronaut.* **170**, 235. DOI. ADS.

González-Bárcena, D., Fernández-Soler, A., González-Llana, A., Díez-González, J., Álvarez, R., Pérez-Grande, I., Sanz-Andrés, Á.: 2022, Ascent phase thermal analysis of long duration balloons. *Acta Astronaut.* **195**, 416. DOI. ADS.

González-Llana, A., González-Bárcena, D., Pérez-Grande, I., Sanz-Andrés, Á.: 2018, Selection of extreme environmental conditions, albedo coefficient and Earth infrared radiation, for polar summer long duration balloon missions. *Acta Astronaut.* **148**, 276. DOI. ADS.

Gonzalo, A., Reina, M., Sánchez, A., Fernández-Medina, A., Cebollero, M., Laguna, H., Escribano, D., Álvarez-Herrero, A.: 2023, TuMag optical unit thermal control for a stratospheric balloon-borne mission. In: *52nd International Conference on Environmental Systems*, 139.

Goode, P.R., Yurchyshyn, V., Cao, W., Abramenko, V., Andic, A., Ahn, K., Chae, J.: 2010, Highest resolution observations of the quietest Sun. *Astrophys. J. Lett.* **714**, L31. DOI. ADS.

Guglielmino, S.L., Martínez Pillet, V., Bonet, J.A., del Toro Iniesta, J.C., Bellot Rubio, L.R., Solanki, S.K., Schmidt, W., Gandorfer, A., Barthol, P., Knölker, M.: 2012, The frontier between small-scale bipoles and ephemeral regions in the solar photosphere: emergence and decay of an intermediate-scale bipole observed with SUNRISE/IMaX. *Astrophys. J.* **745**, 160. DOI. ADS.

Haigh, J.D., Winning, A.R., Toumi, R., Harder, J.W.: 2010, An influence of solar spectral variations on radiative forcing of climate. *Nature* **467**, 696. DOI. ADS.

Hamilton, A.: 2024, Gondola Structural Design Requirements. Requirements document, NASA Balloon Program Office (BPO). https://www.csbf.nasa.gov/documents/gondola/820-PG-8700.0.1A%20Gondola%20Structural%20Design%20Req.%2011.4.pdf.

Hotta, H., Rempel, M., Yokoyama, T.: 2015, Efficient small-scale dynamo in the solar convection zone. *Astrophys. J.* **803**, 42. DOI. ADS.

Iglesias, F.A., Feller, A.: 2019, Instrumentation for solar spectropolarimetry: state of the art and prospects. *Opt. Eng.* **58**, 082417. DOI. ADS.

Iglesias, F.A., Feller, A., Gandorfer, A., Riethmüller, T.L., Korpi-Lagg, A., Solanki, S.K., Katsukawa, Y., Kubo, M., Sanchez Toledo, M.: 2025, The Sunrise Ultraviolet Spectropolarimeter and Imager: Standalone polarimetric calibration. *Sol. Phys.* To be published in Solar Physics Topical Collection "The Sunrise III Solar Observatory".

Jess, D.B., Mathioudakis, M., Erdélyi, R., Crockett, P.J., Keenan, F.P., Christian, D.J.: 2009, Alfvén waves in the lower solar atmosphere. *Science* **323**, 1582. DOI. ADS.

Judge, P., Kleint, L., Casini, R., de Wijn, A.G., Schad, T., Tritschler, A.: 2024, Magnetic fields and plasma heating in the Sun's atmosphere. *Astrophys. J.* **960**, 129. DOI. ADS.

Katsukawa, Y., del Toro Iniesta, J.C., Solanki, S.K., Kubo, M., Hara, H., Shimizu, T., Oba, T., Kawabata, Y., Tsuzuki, T., Uraguchi, F., Nodomi, Y., Shinoda, K., Tamura, T., Suematsu, Y., Ishikawa, R., Kano, R., Matsumoto, T., Ichimoto, K., Nagata, S., Quintero Noda, C., Anan, T., Orozco Suárez, D., Balaguer Jiménez, M., López Jiménez, A.C., Cobos Carrascosa, J.P., Feller, A., Riethmüller, T., Gandorfer, A., Lagg, A.: 2020, Sunrise Chromospheric Infrared SpectroPolarimeter (SCIP) for Sunrise III: system design and capability. In: Evans, C.J., Bryant, J.J., Motohara, K. (eds.) *Ground-Based and Airborne Instrumentation for Astronomy VIII*, *Society of Photo-Optical Instrumentation Engineers (SPIE) Conference Series* **11447**, 114470Y. DOI. ADS.

Katsukawa, Y., del Toro Iniesta, J.C., Solanki, S.K., Kubo, M., Hara, H., Shimizu, T., Oba, T., Kawabata, Y., Tsuzuki, T., Uraguchi, F., Shinoda, K., Tamura, T., Suematsu, Y., Matsumoto, T., Ishikawa, R.T., Naito, Y., Ichimoto, K., Nagata, S., Anan, T., Orozco Suárez, D., Balaguer Jiménez, M., López Jiménez, A.C., Quintero Noda, C., Álvarez García, D., Ramos Más, J.L., Aparicio del Moral, B., Sánchez Gómez, A., Hernández Expósito, D., Bailón Martínez, E., Morales Fernández, J.M., Moreno Mantas, A., Tobaruela, A., Bustamante, I., Piqueras, J., Pérez Grande, I., Korpi-Lagg, A., Gandorfer, A., Berkefeld, T., Bernasconi, P., Feller, A., Riethmüller, T.L., Smitha, H.N., Martínez Pillet, V., Grauf, B., Bell, A., Carpenter, M.: 2025, The Sunrise Chromospheric Infrared Spectro-Polarimeter SCIP: an Instrument for Sunrise III. *Sol. Phys.* **300**. Part of the Topical Collection "The Sunrise III Solar Observatory".

Kawabata, Y., Katsukawa, Y., Kubo, M., Anan, T., Ichimoto, K., Shinoda, K., Tsuzuki, T., Uraguchi, F., Nagata, S., Oba, T., Expósito, D.H., Sánchez Gómez, A., Orozco Suárez, D., Balaguer Jiménz, M., Bailón Martínez, E., Morales Fernández, J.M., Moreno Mantas, A., del Toro Iniesta, J.C., Gandorfer, A., Feller, A.: 2022, Polarimetric calibration of a spectropolarimeter instrument with high precision: Sunrise chromospheric infrared spectropolarimeter (SCIP) for the Sunrise iii balloon telescope. *Appl. Opt.* **61**, 9716. DOI. ADS.

Kawabata, Y., Quintero Noda, C., Katsukawa, Y., Kubo, M., Matsumoto, T., Oba, T.: 2024, Multiline Stokes synthesis of Ellerman bombs: obtaining seamless information from photosphere to chromosphere. *Astrophys. J.* **960**, 26. DOI. ADS.

Khomenko, E., Vitas, N., Collados, M., de Vicente, A.: 2017, Numerical simulations of quiet Sun magnetic fields seeded by the Biermann battery. *Astron. Astrophys.* **604**, A66. DOI. ADS.

Klimchuk, J.A.: 2006, On solving the coronal heating problem. *Sol. Phys.* **234**, 41. DOI. ADS.

Korpi-Lagg, M.J., Korpi-Lagg, A., Olspert, N., Truong, H.-L.: 2022, Solar-cycle variation of quiet-Sun magnetism and surface gravity oscillation mode. *Astron. Astrophys.* **665**, A141. DOI. ADS.

Kosugi, T., Matsuzaki, K., Sakao, T., Shimizu, T., Sone, Y., Tachikawa, S., Hashimoto, T., Minesugi, K., Ohnishi, A., Yamada, T., Tsuneta, S., Hara, H., Ichimoto, K., Suematsu, Y., Shimojo, M., Watanabe, T., Shimada, S., Davis, J.M., Hill, L.D., Owens, J.K., Title, A.M., Culhane, J.L., Harra, L.K., Doschek, G.A., Golub, L.: 2007, The Hinode (Solar-B) mission: an overview. *Sol. Phys.* **243**, 3. DOI. ADS.

Krivova, N.A., Solanki, S.K., Floyd, L.: 2006, Reconstruction of solar UV irradiance in cycle 23. *Astron. Astrophys.* **452**, 631. DOI. ADS.

Kubo, M., Shimizu, T., Katsukawa, Y., Kawabata, Y., Anan, T., Ichimoto, K., Shinoda, K., Tamura, T., Nodomi, Y., Nakayama, S., Yamada, T., Tajima, T., Nakata, S., Nakajima, Y., Okutani, K., Feller, A., del Toro Iniesta, J.C.: 2020, Sunrise Chromospheric Infrared spectroPolarimeter (SCIP) for SUNRISE III: polarization modulation unit. In: Evans, C.J., Bryant, J.J., Motohara, K. (eds.) *Ground-Based and Airborne Instrumentation for Astronomy VIII*, *Society of Photo-Optical Instrumentation Engineers (SPIE) Conference Series* **11447**, 11447A3. DOI. ADS.

Kubo, M., Katsukawa, Y., Hernández Expósito, D., Sánchez Gómez, A., Balaguer Jimenéz, M., Orozco Suárez, D., Morales Fernández, J.M., Aparicio del Moral, B., Moreno Mantas, A.J., Bailón Martínez, E., del Toro Iniesta, J.C., Kawabata, Y., Quintero Noda, C., Oba, T., Ishikawa, R.T., Shimizu, T.: 2023, High-speed data processing onboard Sunrise chromospheric infrared spectropolarimeter for the SUNRISE III balloon telescope. *J. Astron. Telesc. Instrum. Syst.* **9**, 034003. DOI. ADS.

Kuridze, D., Uitenbroek, H., Wöger, F., Mathioudakis, M., Morgan, H., Campbell, R., Fischer, C., Cauzzi, G., Schad, T., Reardon, K., da Silva Santos, J.M., Beck, C., Tritschler, A., Rimmele, T.: 2024, Insight into the solar plage chromosphere with DKIST. *Astrophys. J.* **965**, 15. DOI. ADS.

Kurucz, R.L., Bell, B.: 1995, Atomic line list. ADS.

Lagg, A., Solanki, S.K., Riethmüller, T.L., Martínez Pillet, V., Schüssler, M., Hirzberger, J., Feller, A., Borrero, J.M., Schmidt, W., del Toro Iniesta, J.C., Bonet, J.A., Barthol, P., Berkefeld, T., Domingo, V., Gandorfer, A., Knölker, M., Title, A.M.: 2010, Fully resolved quiet-Sun magnetic flux tube observed with the SUNRISE/IMAX instrument. *Astrophys. J. Lett.* **723**, L164. DOI. ADS.

Lagg, A., Lites, B., Harvey, J., Gosain, S., Centeno, R.: 2017, Measurements of photospheric and chromospheric magnetic fields. *Space Sci. Rev.* **210**, 37. DOI. ADS.

Lagg, A., Solanki, S.K., Katsukawa, Y., Bernasconi, P., del Toro Iniesta, J.C., Berkefeld, T., Gandorfer, A., Feller, A., Riethmüller, T.: 2021, MoA Data Policy and Co-Authorship. Sunrise iii document database, MPS. https://www.mps.mpg.de/solar-physics/sunrise/documents.

Lamb, D.A., Howard, T.A., DeForest, C.E., Parnell, C.E., Welsch, B.T.: 2013, Solar magnetic tracking. IV. The death of magnetic features. *Astrophys. J.* **774**, 127. DOI. ADS.

Li, C., Fang, C., Li, Z., Ding, M., Chen, P., Qiu, Y., You, W., Yuan, Y., An, M., Tao, H., Li, X., Chen, Z., Liu, Q., Mei, G., Yang, L., Zhang, W., Cheng, W., Chen, J., Chen, C., Gu, Q., Huang, Q., Liu, M., Han, C., Xin, H., Chen, C., Ni, Y., Wang, W., Rao, S., Li, H., Lu, X., Wang, W., Lin, J., Jiang, Y., Meng, L., Zhao, J.: 2022, The Chinese Hα Solar Explorer (CHASE) mission: an overview. *Sci. China, Phys. Mech. Astron.* **65**, 289602. DOI. ADS.

Lites, B.W., Centeno, R., McIntosh, S.W.: 2014, The solar cycle dependence of the weak internetwork flux. *Publ. Astron. Soc. Jpn.* **66**, S4. DOI. ADS.

Liu, Z., Xu, J., Gu, B.-Z., Wang, S., You, J.-Q., Shen, L.-X., Lu, R.-W., Jin, Z.-Y., Chen, L.-F., Lou, K., Li, Z., Liu, G.-Q., Xu, Z., Rao, C.-H., Hu, Q.-Q., Li, R.-F., Fu, H.-W., Wang, F., Bao, M.-X., Wu, M.-C., Zhang, B.-R.: 2014, New vacuum solar telescope and observations with high resolution. *Res. Astron. Astrophys.* **14**, 705. DOI. ADS.

Martínez González, M.J., Collados, M., Ruiz Cobo, B., Solanki, S.K.: 2007, Low-lying magnetic loops in the solar internetwork. *Astron. Astrophys.* **469**, L39. DOI. ADS.

Martínez González, M.J., Bellot Rubio, L.R., Solanki, S.K., Martínez Pillet, V., Del Toro Iniesta, J.C., Barthol, P., Schmidt, W.: 2012, Resolving the internal magnetic structure of the solar network. *Astrophys. J. Lett.* **758**, L40. DOI. ADS.

Martínez Pillet, V., Del Toro Iniesta, J.C., Álvarez-Herrero, A., Domingo, V., Bonet, J.A., González Fernández, L., López Jiménez, A., Pastor, C., Gasent Blesa, J.L., Mellado, P., Piqueras, J., Aparicio, B., Balaguer, M., Ballesteros, E., Belenguer, T., Bellot Rubio, L.R., Berkefeld, T., Collados, M., Deutsch, W., Feller, A., Girela, F., Grauf, B., Heredero, R.L., Herranz, M., Jerónimo, J.M., Laguna, H., Meller, R., Menéndez, M., Morales, R., Orozco Suárez, D., Ramos, G., Reina, M., Ramos, J.L., Rodríguez, P., Sánchez, A., Uribe-Patarroyo, N., Barthol, P., Gandorfer, A., Knoelker, M., Schmidt, W., Solanki, S.K., Vargas Domínguez, S.: 2011, The Imaging Magnetograph eXperiment (IMaX) for the Sunrise balloon-borne Solar Observatory. *Sol. Phys.* **268**, 57. DOI. ADS.

Martínez-Sykora, J., Hansteen, V.H., Gudiksen, B., Carlsson, M., De Pontieu, B., Gošić, M.: 2019, On the origin of the magnetic energy in the quiet solar chromosphere. *Astrophys. J.* **878**, 40. DOI. ADS.

Mathew, S.K., Bayanna, A.R., Tiwary, A.R., Bireddy, R., Venkatakrishnan, P.: 2017, First observations from the Multi-Application Solar Telescope (MAST) narrow-band imager. *Sol. Phys.* **292**, 106. DOI. ADS.

Matsumoto, T., Kawabata, Y., Katsukawa, Y., Iijima, H., Quintero Noda, C.: 2023, Synthesis of infrared Stokes spectra in an evolving solar chromospheric jet. *Mon. Not. R. Astron. Soc.* **523**, 974. DOI. ADS.

McIntosh, S.W., de Pontieu, B., Carlsson, M., Hansteen, V., Boerner, P., Goossens, M.: 2011, Alfvénic waves with sufficient energy to power the quiet solar corona and fast solar wind. *Nature* **475**, 477. DOI. ADS.

Molnar, M.E., Reardon, K.P., Chai, Y., Gary, D., Uitenbroek, H., Cauzzi, G., Cranmer, S.R.: 2019, Solar chromospheric temperature diagnostics: a joint ALMA-Hα analysis. *Astrophys. J.* **881**, 99. DOI. ADS.

Müller, D., St. Cyr, O.C., Zouganelis, I., Gilbert, H.R., Marsden, R., Nieves-Chinchilla, T., Antonucci, E., Auchère, F., Berghmans, D., Horbury, T.S., Howard, R.A., Krucker, S., Maksimovic, M., Owen, C.J., Rochus, P., Rodriguez-Pacheco, J., Romoli, M., Solanki, S.K., Bruno, R., Carlsson, M., Fludra, A., Harra, L., Hassler, D.M., Livi, S., Louarn, P., Peter, H., Schühle, U., Teriaca, L., del Toro Iniesta, J.C., Wimmer-Schweingruber, R.F., Marsch, E., Velli, M., De Groof, A., Walsh, A., Williams, D.: 2020, The Solar Orbiter mission. Science overview. *Astron. Astrophys.* **642**, A1. DOI. ADS.

Nordlund, Å., Stein, R.F., Asplund, M.: 2009, Solar surface convection. *Living Rev. Sol. Phys.* **6**, 2. DOI. ADS.

Oba, T., Shimizu, T., Katsukawa, Y., Kubo, M., Kawabata, Y., Hara, H., Uraguchi, F., Tsuzuki, T., Tamura, T., Shinoda, K., Kodeki, K., Fukushima, K., Morales Fernández, J.M., Sánchez Gómez, A., Balaguer Jimenéz, M., Hernández Expósito, D., Gandorfer, A.: 2022, Development of fast and precise scan mirror mechanism for an Airborne solar telescope. *Sol. Phys.* **297**, 114. DOI. ADS.

Offner, A.: 1973, Unit power imaging catoptric anastigmat 3,748,015. https://patents.google.com/patent/US3748015A/en.

Orozco Suárez, D., Álvarez García, D., López Jiménez, A.C., Balaguer Jiménez, M., Hernández Expósito, D., Labrousse, P., Bailén, F.J., Bustamante Díaz, I., Bailón Martínez, E., Aparicio del Moral, B., Morales Fernández, J.M., Sánchez Gómez, A., Tobaruela Abarca, Á., Moreno Mantas, A.J., Ramos Más, J.L., Pérez Grande, I., Piqueras Carreño, J., Katsukawa, Y., Kubo, M., Kawabata, Y., Oba, T., Rodríguez Valido, M., Magdaleno Castelló, E., Del Toro Iniesta, J.C.: 2023, SPGCam: a specifically tailored camera for solar observations. *Front. Astron. Space Sci.* **10**, 1167540. DOI. ADS.

Parker, E.N.: 1983, Magnetic neutral sheets in evolving fields - part two - formation of the solar corona. *Astrophys. J.* **264**, 642. DOI. ADS.

Pereira, T.M.D., Uitenbroek, H.: 2015, RH 1.5D: a massively parallel code for multi-level radiative transfer with partial frequency redistribution and Zeeman polarisation. *Astron. Astrophys.* **574**, A3. DOI. ADS.

Pérez-Grande, I., Sanz-Andrés, A., Bezdenejnykh, N., Farrahi, A., Barthol, P., Meller, R.: 2011, Thermal control of SUNRISE, a balloon-borne solar telescope. *Proc. Inst. Mech. Eng., Part G, J. Aerosp. Eng.* **225**, 1037. DOI.

Pesnell, W.D., Thompson, B.J., Chamberlin, P.C.: 2012, The Solar Dynamics Observatory (SDO). *Sol. Phys.* **275**, 3. DOI. ADS.

Peter, H., Gudiksen, B.V., Nordlund, Å.: 2004, Coronal heating through braiding of magnetic field lines. *Astrophys. J. Lett.* **617**, L85. DOI. ADS.

Petrovay, K., Szakaly, G.: 1993, The origin of intranetwork fields: a small-scale solar dynamo. *Astron. Astrophys.* **274**, 543. ADS.

Pontin, D.I., Hornig, G.: 2020, The Parker problem: existence of smooth force-free fields and coronal heating. *Living Rev. Sol. Phys.* **17**, 5. DOI. ADS.

Przybylski, D., Cameron, R., Solanki, S.K., Rempel, M., Leenaarts, J., Anusha, L.S., Witzke, V., Shapiro, A.I.: 2022, Chromospheric extension of the MURaM code. *Astron. Astrophys.* **664**, A91. DOI. ADS.

Quintero Noda, C., Shimizu, T., Katsukawa, Y., de la Cruz Rodríguez, J., Carlsson, M., Anan, T., Oba, T., Ichimoto, K., Suematsu, Y.: 2017, Chromospheric polarimetry through multiline observations of the 850-nm spectral region. *Mon. Not. R. Astron. Soc.* **464**, 4534. DOI. ADS.

Quintero Noda, C., Villanueva, G.L., Katsukawa, Y., Solanki, S.K., Orozco Suárez, D., Ruiz Cobo, B., Shimizu, T., Oba, T., Kubo, M., Anan, T., Ichimoto, K., Suematsu, Y.: 2018, Solar polarimetry in the K I D_2 line: a novel possibility for a stratospheric balloon. *Astron. Astrophys.* **610**, A79. DOI. ADS.

Ramanath, S.: 2022, Sunrise III PFI TV Test. Sunrise iii document database, MPS. https://www.mps.mpg.de/solar-physics/sunrise/documents.

Ramanath, S., Bayon Laguna, M.: 2022, ICS TV Test. Sunrise iii document database, MPS. https://www.mps.mpg.de/solar-physics/sunrise/documents.

Rast, M.P., Bello González, N., Bellot Rubio, L., Cao, W., Cauzzi, G., Deluca, E., de Pontieu, B., Fletcher, L., Gibson, S.E., Judge, P.G., Katsukawa, Y., Kazachenko, M.D., Khomenko, E., Landi, E., Martínez Pillet, V., Petrie, G.J.D., Qiu, J., Rachmeler, L.A., Rempel, M., Schmidt, W., Scullion, E., Sun, X., Welsch, B.T., Andretta, V., Antolin, P., Ayres, T.R., Balasubramaniam, K.S., Ballai, I., Berger, T.E., Bradshaw, S.J., Campbell, R.J., Carlsson, M., Casini, R., Centeno, R., Cranmer, S.R., Criscuoli, S., Deforest, C., Deng, Y., Erdélyi, R., Fedun, V., Fischer, C.E., González Manrique, S.J., Hahn, M., Harra, L., Henriques, V.M.J., Hurlburt, N.E., Jaeggli, S., Jafarzadeh, S., Jain, R., Jefferies, S.M., Keys, P.H., Kowalski, A.F., Kuckein, C., Kuhn, J.R., Kuridze, D., Liu, J., Liu, W., Longcope, D., Mathioudakis, M., McAteer, R.T.J., McIntosh, S.W., McKenzie, D.E., Miralles, M.P., Morton, R.J., Muglach, K., Nelson, C.J., Panesar, N.K., Parenti, S., Parnell, C.E., Poduval, B., Reardon, K.P., Reep, J.W., Schad, T.A., Schmit, D., Sharma, R., Socas-Navarro, H., Srivastava, A.K., Sterling, A.C., Suematsu, Y., Tarr, L.A., Tiwari, S., Tritschler, A., Verth, G., Vourlidas, A., Wang, H., Wang, Y.-M., NSO and DKIST Project, DKIST Instrument Scientists, DKIST Science Working Group, DKIST Critical Science Plan Community: 2021, Critical science plan for the Daniel K. Inouye Solar Telescope (DKIST). *Sol. Phys.* **296**, 70. DOI. ADS.

Rempel, M.: 2012, Numerical sunspot models: robustness of photospheric velocity and magnetic field structure. *Astrophys. J.* **750**, 62. DOI. ADS.

Rempel, M.: 2014, Numerical simulations of quiet Sun magnetism: on the contribution from a small-scale dynamo. *Astrophys. J.* **789**, 132. DOI. ADS.

Rempel, M., Schlichenmaier, R.: 2011, Sunspot modeling: from simplified models to radiative MHD simulations. *Living Rev. Sol. Phys.* **8**, 3. DOI. ADS.

Rempel, M., Schüssler, M., Cameron, R.H., Knölker, M.: 2009, Penumbral structure and outflows in simulated sunspots. *Science* **325**, 171. DOI. ADS.

Rempel, M., Bhatia, T., Bellot Rubio, L., Korpi-Lagg, M.J.: 2023, Small-scale dynamos: from idealized models to solar and stellar applications. *Space Sci. Rev.* **219**, 36. DOI. ADS.

Requerey, I.S., Del Toro Iniesta, J.C., Bellot Rubio, L.R., Bonet, J.A., Martínez Pillet, V., Solanki, S.K., Schmidt, W.: 2014, The history of a quiet-Sun magnetic element revealed by IMaX/SUNRISE. *Astrophys. J.* **789**, 6. DOI. ADS.

Requerey, I.S., Del Toro Iniesta, J.C., Bellot Rubio, L.R., Martínez Pillet, V., Solanki, S.K., Schmidt, W.: 2017, Convectively driven sinks and magnetic fields in the quiet-Sun. *Astrophys. J. Suppl. Ser.* **229**, 14. DOI. ADS.

Riethmüller, T.L., Solanki, S.K.: 2019, The potential of many-line inversions of photospheric spectropolarimetric data in the visible and near-UV. *Astron. Astrophys.* **622**, A36. DOI. ADS.

Rimmele, T.R., Warner, M., Keil, S.L., Goode, P.R., Knölker, M., Kuhn, J.R., Rosner, R.R., McMullin, J.P., Casini, R., Lin, H., Wöger, F., von der Lühe, O., Tritschler, A., Davey, A., de Wijn, A., Elmore, D.F., Fehlmann, A., Harrington, D.M., Jaeggli, S.A., Rast, M.P., Schad, T.A., Schmidt, W., Mathioudakis, M., Mickey, D.L., Anan, T., Beck, C., Marshall, H.K., Jeffers, P.F., Oschmann, J.M., Beard, A., Berst, D.C., Cowan, B.A., Craig, S.C., Cross, E., Cummings, B.K., Donnelly, C., de Vanssay, J.-B., Eigenbrot, A.D., Ferayorni, A., Foster, C., Galapon, C.A., Gedrites, C., Gonzales, K., Goodrich, B.D., Gregory, B.S., Guzman, S.S., Guzzo, S., Hegwer, S., Hubbard, R.P., Hubbard, J.R., Johansson, E.M., Johnson, L.C., Liang, C., Liang, M., McQuillen, I., Mayer, C., Newman, K., Onodera, B., Phelps, L., Puentes, M.M., Richards, C., Rimmele, L.M., Sekulic, P., Shimko, S.R., Simison, B.E., Smith, B., Starman, E., Sueoka, S.R., Summers, R.T., Szabo, A., Szabo, L., Wampler, S.B., Williams, T.R., White, C.: 2020, The Daniel K. Inouye solar telescope - observatory overview. *Sol. Phys.* **295**, 172. DOI. ADS.

Rouppe van der Voort, L.H.M., Rutten, R.J., Vissers, G.J.M.: 2016, Reconnection brightenings in the quiet solar photosphere. *Astron. Astrophys.* **592**, A100. DOI. ADS.

Rouppe van der Voort, L.H.M., van Noort, M., de la Cruz Rodríguez, J.: 2023, Ultra-high-resolution observations of plasmoid-mediated magnetic reconnection in the deep solar atmosphere. *Astron. Astrophys.* **673**, A11. DOI. ADS.

Sánchez, A., Gonzalo, A., Garranzo, D., Silva-López, M., Núñez, A., Laguna, H., Cebollero, M., Fernández-Medina, A.B., Álvarez-Herrero, A.: 2022, High precision and thermally controlled filter wheel. In: *Society of Photo-Optical Instrumentation Engineers (SPIE) Conference Series*, *Society of Photo-Optical Instrumentation Engineers (SPIE) Conference Series* **12188**, 121883A. DOI. ADS.

Scharmer, G.B., Sliepen, G., Sinquin, J.-C., Löfdahl, M.G., Lindberg, B., Sütterlin, P.: 2024, The 85-electrode adaptive optics system of the Swedish 1-m solar telescope. *Astron. Astrophys.* **685**, A32. DOI. ADS.

Scherrer, P.H., Schou, J., Bush, R.I., Kosovichev, A.G., Bogart, R.S., Hoeksema, J.T., Liu, Y., Duvall, T.L., Zhao, J., Title, A.M., Schrijver, C.J., Tarbell, T.D., Tomczyk, S.: 2012, The Helioseismic and Magnetic Imager (HMI) Investigation for the Solar Dynamics Observatory (SDO). *Sol. Phys.* **275**, 207. DOI. ADS.

Schmidt, W., von der Lühe, O., Volkmer, R., Denker, C., Solanki, S.K., Balthasar, H., Bello González, N., Berkefeld, T., Collados, M., Fischer, A., Halbgewachs, C., Heidecke, F., Hofmann, A., Kneer, F., Lagg, A., Nicklas, H., Popow, E., Puschmann, K.G., Schmidt, D., Sigwarth, M., Sobotka, M., Soltau, D., Staude, J., Strassmeier, K.G., Waldmann, T.A.: 2012, The 1.5 meter solar telescope GREGOR. *Astron. Nachr.* **333**, 796. DOI. ADS.

Schou, J., Borrero, J.M., Norton, A.A., Tomczyk, S., Elmore, D., Card, G.L.: 2012, Polarization calibration of the Helioseismic and Magnetic Imager (HMI) onboard the Solar Dynamics Observatory (SDO). *Sol. Phys.* **275**, 327. DOI. ADS.

Schrijver, C.J., Title, A.M., van Ballegooijen, A.A., Hagenaar, H.J., Shine, R.A.: 1997, Sustaining the quiet photospheric network: the balance of flux emergence, fragmentation, merging and cancellation. *Astrophys. J.* **487**, 424. DOI. ADS.

Schüssler, M., Vögler, A.: 2006, Magnetoconvection in a sunspot umbra. *Astrophys. J. Lett.* **641**, L73. DOI. ADS.

Seetha, S., Megala, S.: 2017, Aditya-L1 mission. *Curr. Sci.* **113**, 610. DOI. ADS.

Shchukina, N., Trujillo Bueno, J.: 2011, Determining the magnetization of the quiet Sun photosphere from the Hanle effect and surface dynamo simulations. *Astrophys. J. Lett.* **731**, L21. DOI. ADS.

Shibata, K., Nakamura, T., Matsumoto, T., Otsuji, K., Okamoto, T.J., Nishizuka, N., Kawate, T., Watanabe, H., Nagata, S., UeNo, S., Kitai, R., Nozawa, S., Tsuneta, S., Suematsu, Y., Ichimoto, K., Shimizu, T., Katsukawa, Y., Tarbell, T.D., Berger, T.E., Lites, B.W., Shine, R.A., Title, A.M.: 2007, Chromospheric anemone jets as evidence of ubiquitous reconnection. *Science* **318**, 1591. DOI. ADS.

Singh, N.K., Raichur, H., Brandenburg, A.: 2016, High-wavenumber solar f-mode strengthening prior to active region formation. *Astrophys. J.* **832**, 120. DOI. ADS.

Smitha, H.N., Korpi-Lagg, A.: 2024, Sunrise III Observing Plan. Sunrise iii document database, MPS. https://www.mps.mpg.de/solar-physics/sunrise/documents.

Smitha, H.N., Anusha, L.S., Solanki, S.K., Riethmüller, T.L.: 2017, Estimation of the magnetic flux emergence rate in the quiet Sun from Sunrise data. *Astrophys. J. Suppl. Ser.* **229**, 17. DOI. ADS.

Solanki, S.K.: 1993, Smallscale solar magnetic fields - an overview. *Space Sci. Rev.* **63**, 1. DOI. ADS.

Solanki, S.K.: 2003, Sunspots: an overview. *Astron. Astrophys. Rev.* **11**, 153. DOI. ADS.

Solanki, S.K.: 2017, Overview of the special issue on the first science results from the second flight of sunrise. *Astrophys. J. Suppl. Ser.* **229**, 1. DOI. ADS.

Solanki, S.K., Inhester, B., Schüssler, M.: 2006, The solar magnetic field. *Rep. Prog. Phys.* **69**, 563. DOI. ADS.

Solanki, S.K., Krivova, N.A., Haigh, J.D.: 2013, Solar irradiance variability and climate. *Annu. Rev. Astron. Astrophys.* **51**, 311. DOI. ADS.

Solanki, S.K., Stenflo, J.O.: 1984, Properties of solar magnetic fluxtubes as revealed by Fe I lines. *Astron. Astrophys.* **140**, 185. ADS.

Solanki, S.K., Barthol, P., Danilovic, S., Feller, A., Gandorfer, A., Hirzberger, J., Riethmüller, T.L., Schüssler, M., Bonet, J.A., Martínez Pillet, V., del Toro Iniesta, J.C., Domingo, V., Palacios, J., Knölker, M., Bello González, N., Berkefeld, T., Franz, M., Schmidt, W., Title, A.M.: 2010, SUNRISE: instrument, mission, data and first results. *Astrophys. J. Lett.* **723**, L127. DOI. ADS.

Solanki, S.K., Riethmüller, T.L., Barthol, P., Danilovic, S., Deutsch, W., Doerr, H.-P., Feller, A., Gandorfer, A., Germerott, D., Gizon, L., Grauf, B., Heerlein, K., Hirzberger, J., Kolleck, M., Lagg, A., Meller, R., Tomasch, G., van Noort, M., Blanco Rodríguez, J., Gasent Blesa, J.L., Balaguer Jiménez, M., Del Toro Iniesta, J.C., López Jiménez, A.C., Orozco Suarez, D., Berkefeld, T., Halbgewachs, C., Schmidt, W., Álvarez-Herrero, A., Sabau-Graziati, L., Pérez Grande, I., Martínez Pillet, V., Card, G., Centeno, R., Knölker, M., Lecinski, A.: 2017, The second flight of the Sunrise balloon-borne Solar Observatory: overview of instrument updates, the flight, the data and first results. *Astrophys. J. Suppl. Ser.* **229**, 2. DOI. ADS.

Solanki, S.K., del Toro Iniesta, J.C., Woch, J., Gandorfer, A., Hirzberger, J., Alvarez-Herrero, A., Appourchaux, T., Martínez Pillet, V., Pérez-Grande, I., Sanchis Kilders, E., Schmidt, W., Gómez Cama, J.M., Michalik, H., Deutsch, W., Fernandez-Rico, G., Grauf, B., Gizon, L., Heerlein, K., Kolleck, M., Lagg, A., Meller, R., Müller, R., Schühle, U., Staub, J., Albert, K., Alvarez Copano, M., Beckmann, U., Bischoff, J., Busse, D., Enge, R., Frahm, S., Germerott, D., Guerrero, L., Löptien, B., Meierdierks, T., Oberdorfer, D., Papagiannaki, I., Ramanath, S., Schou, J., Werner, S., Yang, D., Zerr, A., Bergmann, M., Bochmann, J., Heinrichs, J., Meyer, S., Monecke, M., Müller, M.-F., Sperling, M., Álvarez García, D., Aparicio, B., Balaguer Jiménez, M., Bellot Rubio, L.R., Cobos Carracosa, J.P., Girela, F., Hernández Expósito, D., Herranz, M., Labrousse, P., López Jiménez, A., Orozco Suárez, D., Ramos, J.L., Barandiarán, J., Bastide, L., Campuzano, C., Cebollero, M., Dávila, B., Fernández-Medina, A., García Parejo, P., Garranzo-García, D., Laguna, H., Martín, J.A., Navarro, R., Núñez Peral, A., Royo, M., Sánchez, A., Silva-López, M., Vera, I., Villanueva, J., Fourmond, J.-J., de Galarreta, C.R., Bouzit, M., Hervier, V., Le Clec'h, J.C., Szwec, N., Chaigneau, M., Buttice, V., Dominguez-Tagle, C., Philippon, A., Boumier, P., Le Cocguen, R., Baranjuk, G., Bell, A., Berkefeld, T., Baumgartner, J., Heidecke, F., Maue, T., Nakai, E., Scheiffelen, T., Sigwarth, M., Soltau, D., Volkmer, R., Blanco Rodríguez, J., Domingo, V., Ferreres Sabater, A., Gasent Blesa, J.L., Rodríguez Martínez, P., Osorno Caudel, D., Bosch, J., Casas, A., Carmona, M., Herms, A., Roma, D., Alonso, G., Gómez-Sanjuan, A., Piqueras, J., Torralbo, I., Fiethe, B., Guan, Y., Lange, T., Michel, H., Bonet, J.A., Fahmy, S., Müller, D., Zouganelis, I.: 2020, The Polarimetric and Helioseismic Imager on Solar Orbiter. *Astron. Astrophys.* **642**, A11. DOI. ADS.

Soltau, D.: 1991, The German solar telescopes on Tenerife. *Adv. Space Res.* **11**, 133. DOI. ADS.

Stein, R.F.: 2012, Solar surface magneto-convection. *Living Rev. Sol. Phys.* **9**, 4. DOI. ADS.

Stenflo, J.O.: 1973, Magnetic-field structure of the photospheric network. *Sol. Phys.* **32**, 41. DOI. ADS.

Stenflo, J.: 1994, *Solar Magnetic Fields: Polarized Radiation Diagnostics* **189**, Springer, Berlin. DOI. ADS.

Stenflo, J.O.: 2012, Basal magnetic flux and the local solar dynamo. *Astron. Astrophys.* **547**, A93. DOI. ADS.

Stenflo, J.O., Keller, C.U.: 1997, The second solar spectrum. A new window for diagnostics of the Sun. *Astron. Astrophys.* **321**, 927. ADS.

Stenflo, J.O., Kosovichev, A.G.: 2012, Bipolar magnetic regions on the Sun: global analysis of the SOHO/MDI data set. *Astrophys. J.* **745**, 129. DOI. ADS.

Thaler, I., Borrero, J.M.: 2023, Photospheric signatures of retraction and reconnection in realistic magnetohydrodynamic simulations. *Astron. Astrophys.* **673**, A163. DOI. ADS.

Thornton, L.M., Parnell, C.E.: 2011, Small-scale flux emergence observed using Hinode/SOT. *Sol. Phys.* **269**, 13. DOI. ADS.

Trujillo Bueno, J., Shchukina, N., Asensio Ramos, A.: 2004, A substantial amount of hidden magnetic energy in the quiet Sun. *Nature* **430**, 326. DOI. ADS.

Tsuneta, S., Ichimoto, K., Katsukawa, Y., Nagata, S., Otsubo, M., Shimizu, T., Suematsu, Y., Nakagiri, M., Noguchi, M., Tarbell, T., Title, A., Shine, R., Rosenberg, W., Hoffmann, C., Jurcevich, B., Kushner, G., Levay, M., Lites, B., Elmore, D., Matsushita, T., Kawaguchi, N., Saito, H., Mikami, I., Hill, L.D., Owens, J.K.: 2008, The solar optical telescope for the Hinode mission: an overview. *Sol. Phys.* **249**, 167. DOI. ADS.

Tsuzuki, T., Katsukawa, Y., Uraguchi, F., Hara, H., Kubo, M., Nodomi, Y., Suematsu, Y., Kawabata, Y., Shimizu, T., Gandorfer, A., Feller, A., Grauf, B., Solanki, S., Carlos del Toro Iniesta, J.: 2020, Sunrise Chromospheric Infrared spectroPolarimeter (SCIP) for SUNRISE III: optical design and performance.

In: Evans, C.J., Bryant, J.J., Motohara, K. (eds.) *Ground-Based and Airborne Instrumentation for Astronomy VIII*, *Society of Photo-Optical Instrumentation Engineers (SPIE) Conference Series* **11447**, 11447AJ. DOI. ADS.

Ueno, S., Nagata, S.-i., Kitai, R., Kurokawa, H., Ichimoto, K.: 2004, The development of filter vector magnetographs for the Solar Magnetic Activity Research Telescope (SMART). In: Moorwood, A.F.M., Iye, M. (eds.) *Ground-Based Instrumentation for Astronomy*, *Society of Photo-Optical Instrumentation Engineers (SPIE) Conference Series* **5492**, 958. DOI. ADS.

Uitenbroek, H.: 2001, Multilevel radiative transfer with partial frequency redistribution. *Astrophys. J.* **557**, 389. DOI. ADS.

Uraguchi, F., Tsuzuki, T., Katsukawa, Y., Hara, H., Iwamura, S., Kubo, M., Nodomi, Y., Suematsu, Y., Kawabata, Y., Shimizu, T., Gandorfer, A., del Toro Iniesta, J.C.: 2020, Sunrise Chromospheric Infrared spectroPolarimeter (SCIP) for SUNRISE III: opto-mechanical analysis and design. In: Evans, C.J., Bryant, J.J., Motohara, K. (eds.) *Ground-Based and Airborne Instrumentation for Astronomy VIII*, *Society of Photo-Optical Instrumentation Engineers (SPIE) Conference Series* **11447**, 11447AB. DOI. ADS.

van Ballegooijen, A.A., Martens, P.C.H.: 1989, Formation and eruption of solar prominences. *Astrophys. J.* **343**, 971. DOI. ADS.

van Ballegooijen, A.A., Asgari-Targhi, M., Cranmer, S.R., DeLuca, E.E.: 2011, Heating of the solar chromosphere and corona by Alfvén wave turbulence. *Astrophys. J.* **736**, 3. DOI. ADS.

van Noort, M.: 2017, Image restoration of solar spectra. *Astron. Astrophys.* **608**, A76. DOI. ADS.

Varma, M., u'Padinhatteeri, S., Sinha, S., Tyagi, A., Burse, M., Yadav, R., Kumar, G., Ramaprakash, A., Tripathi, D., Sankarasubramanian, K., Nagaraju, K., Vadodariya, K., Tadepalli, S., Deogaonkar, R., Olekar, M., Azaruddin, M., Unnikrishnan, A.: 2023, The Solar Ultra-Violet Imaging Telescope (SUIT) onboard intelligence for flare observations. *Sol. Phys.* **298**, 16. DOI. ADS.

Vissers, G.J.M., Rouppe van der Voort, L.H.M., Rutten, R.J., Carlsson, M., De Pontieu, B.: 2015, Ellerman bombs at high resolution. III. Simultaneous observations with IRIS and SST. *Astrophys. J.* **812**, 11. DOI. ADS.

Vögler, A., Schüssler, M.: 2007, A solar surface dynamo. *Astron. Astrophys.* **465**, L43. DOI. ADS.

Waidele, M., Roth, M., Singh, N.K., Käpylä, P.J.: 2023, On strengthening of the solar f-mode prior to active region emergence using the Fourier-Hankel analysis. *Sol. Phys.* **298**, 30. DOI. ADS.

Warnecke, J., Korpi-Lagg, M.J., Gent, F.A., Rheinhardt, M.: 2023, Numerical evidence for a small-scale dynamo approaching solar magnetic Prandtl numbers. *Nat. Astron.* **7**, 662. DOI. ADS.

Weber, M.A., Schunker, H., Jouve, L., Işık, E.: 2023, Understanding active region origins and emergence on the Sun and other cool stars. *Space Sci. Rev.* **219**, 63. DOI. ADS.

Wedemeyer, S., Bastian, T., Brajša, R., Hudson, H., Fleishman, G., Loukitcheva, M., Fleck, B., Kontar, E.P., De Pontieu, B., Yagoubov, P., Tiwari, S.K., Soler, R., Black, J.H., Antolin, P., Scullion, E., Gunár, S., Labrosse, N., Ludwig, H.-G., Benz, A.O., White, S.M., Hauschildt, P., Doyle, J.G., Nakariakov, V.M., Ayres, T., Heinzel, P., Karlicky, M., Van Doorsselaere, T., Gary, D., Alissandrakis, C.E., Nindos, A., Solanki, S.K., Rouppe van der Voort, L., Shimojo, M., Kato, Y., Zaqarashvili, T., Perez, E., Selhorst, C.L., Barta, M.: 2016, Solar science with the Atacama large millimeter/submillimeter array—a new view of our Sun. *Space Sci. Rev.* **200**, 1. DOI. ADS.

Wedemeyer-Böhm, S., Scullion, E., Steiner, O., Rouppe van der Voort, L., de La Cruz Rodriguez, J., Fedun, V., Erdélyi, R.: 2012, Magnetic tornadoes as energy channels into the solar corona. *Nature* **486**, 505. DOI. ADS.

Wells, D.C., Greisen, E.W., Harten, R.H.: 1981, FITS - a flexible image transport system. *Astron. Astrophys. Suppl. Ser.* **44**, 363. ADS.

Withbroe, G.L., Noyes, R.W.: 1977, Mass and energy flow in the solar chromosphere and corona. *Annu. Rev. Astron. Astrophys.* **15**, 363. DOI. ADS.

Wootten, A., Thompson, A.R.: 2009, The Atacama large millimeter/submillimeter array. *Proc. IEEE* **97**, 1463. DOI. ADS.

Yadav, N., Cameron, R.H., Solanki, S.K.: 2021, Slow magneto-acoustic waves in simulations of a solar plage region carry enough energy to heat the chromosphere. *Astron. Astrophys.* **652**, A43. DOI. ADS.

Zirker, J.B.: 1998, The Sacramento Peak Observatory. *Sol. Phys.* **182**, 1. DOI. ADS.

Zwaan, C.: 1987, Elements and patterns in the solar magnetic field. *Annu. Rev. Astron. Astrophys.* **25**, 83. DOI. ADS.

Publisher's Note Springer Nature remains neutral with regard to jurisdictional claims in published maps and institutional affiliations.

Authors and Affiliations

Andreas Korpi-Lagg[1,2] · Achim Gandorfer[1] · Sami K. Solanki[1] · Jose Carlos del Toro Iniesta[3,4] · Yukio Katsukawa[5,6,7] · Pietro Bernasconi[8] · Thomas Berkefeld[9] · Alex Feller[1] · Tino L. Riethmüller[1] · Alberto Álvarez-Herrero[10,4] · Masahito Kubo[5] · Valentín Martínez Pillet[11,4] · H.N. Smitha[1] · David Orozco Suárez[3,4] · Bianca Grauf[1] · Michael Carpenter[8] · Alexander Bell[9] · María-Teresa Álvarez-Alonso[10] · Daniel Álvarez García[3,4] · Beatriz Aparicio del Moral[3,4] · Julia Atiénzar[12,4] · Daniel Ayoub[8] · Francisco Javier Bailén[3,4] · Eduardo Bailón Martínez[3,4] · Maria Balaguer Jiménez[3,4] · Peter Barthol[1] · Montserrat Bayon Laguna[1] · Luis R. Bellot Rubio[3,4] · Melani Bergmann[1] · Julian Blanco Rodríguez[13,4] · Jan Bochmann[1] · Juan Manuel Borrero[9] · Antonio Campos-Jara[10,4] · Juan Sebastián Castellanos Durán[1] · María Cebollero[10,4] · Aitor Conde Rodríguez[14,15] · Werner Deutsch[1] · Harry Eaton[8] · Ana Belen Fernández-Medina[10,4] · German Fernandez-Rico[1] · Agustin Ferreres[13,4] · Andrés García[10] · Ramón María García Alarcia[16,15] · Pilar García Parejo[10,4] · Daniel Garranzo-García[10,4] · José Luis Gasent Blesa[13,4] · Karin Gerber[9] · Dietmar Germerott[1] · David Gilabert Palmer[13,4] · Laurent Gizon[1,17] · Miguel Angel Gómez Sánchez-Tirado[15] · David González-Bárcena[18,4] · Alejandro Gonzalo Melchor[10,4] · Sam Goodyear[1] · Hirohisa Hara[5] · Edvarda Harnes[1] · Klaus Heerlein[1] · Frank Heidecke[9] · Jan Heinrichs[1] · David Hernández Expósito[11,4] · Johann Hirzberger[1] · Johannes Hoelken[1] · Sangwon Hyun[19] · Francisco A. Iglesias[1,20] · Ryohtaroh T. Ishikawa[21] · Minwoo Jeon[19] · Yusuke Kawabata[5] · Martin Kolleck[1] · Hugo Laguna[10,4] · Julian Lomas[10] · Antonio C. López Jiménez[3,4] · Paula Manzano[10] · Takuma Matsumoto[22] · David Mayo Turrado[15] · Thimo Meierdierks[1] · Stefan Meining[1] · Markus Monecke[1] · José Miguel Morales-Fernández[3,4] · Antonio Jesús Moreno Mantas[3,4] · Alejandro Moreno Vacas[3,4] · Marc Ferenc Müller[1] · Reinhard Müller[1] · Yoshihiro Naito[7,5] · Eiji Nakai[9] · Armonía Núñez Peral[10,4] · Takayoshi Oba[1,5] · Geoffrey Palo[8] · Isabel Pérez-Grande[18,4] · Javier Piqueras Carreño[23,4] · Tobias Preis[9] · Damien Przybylski[1] · Carlos Quintero Noda[11,24,4] · Sandeep Ramanath[1] · Jose Luis Ramos Más[3,4] · Nour Raouafi[8] · María-Jesús Rivas-Martínez[10] · Pedro Rodríguez Martínez[13,4] · Manuel Rodríguez Valido[24,4] · Basilio Ruiz Cobo[11,24,4] · Antonio Sánchez Rodríguez[10,4] · Mariano Sanchez Toledo[20] · Antonio Sánchez Gómez[3,4] · Esteban Sanchis Kilders[13,4] · Kamal Sant[1] · Pablo Santamarina Guerrero[3,4] · Erich Schulze[8] · Toshifumi Shimizu[6,25] · Manuel Silva-López[10,4] · Kunal Singh[1] · Azaymi L. Siu-Tapia[3,4] · Thomas Sonner[9] · Jan Staub[1] · Hanna Strecker[3,4] · Angel Tobaruela[3,4] · Ignacio Torralbo[23,4] · Alexandra Tritschler[26] · Toshihiro Tsuzuki[5] · Fumihiro Uraguchi[5] · Reiner Volkmer[9] · Angelos Vourlidas[8] · Dušan Vukadinović[1] · Stephan Werner[1] · Andreas Zerr[1]

✉ A. Korpi-Lagg
lagg@mps.mpg.de

A. Gandorfer
gandorfer@mps.mpg.de

S.K. Solanki
solanki@mps.mpg.de

J.C. del Toro Iniesta
jti@iaa.es

Y. Katsukawa
yukio.katsukawa@nao.ac.jp

P. Bernasconi
pietro.bernasconi@jhuapl.edu

T. Berkefeld
thomas.berkefeld@leibniz-kis.de

A. Feller
feller@mps.mpg.de

T.L. Riethmüller
riethmueller@mps.mpg.de

1 Max-Planck-Institut für Sonnensystemforschung, Justus-von-Liebig-Weg 3, 37077 Göttingen, Germany

2 Aalto University, Department of Computer Science, Konemiehentie 2, 02150 Espoo, Finland

3 Instituto de Astrofísica de Andalucía, CSIC, Glorieta de la Astronomía s/n, 18008 Granada, Spain

4 Spanish Space Solar Physics Consortium (S3PC) https://s3pc.es

5 National Astronomical Observatory of Japan, 2-21-1 Osawa, Mitaka, Tokyo 181-8588, Japan

6 Department of Earth and Planetary Science, The University of Tokyo, 7-3-1, Hongo, Bunkyo-ku, Tokyo 113-0033, Japan

7 Department of Astronomical Science, The Graduate University for Advanced Studies (SOKENDAI), 2-21-1 Osawa, Mitaka, Tokyo 1818588, Japan

8 Johns Hopkins University Applied Physics Laboratory, 11100 Johns Hopkins Road, Laurel, MD, USA

9 Institut für Sonnenphysik (KIS), Georges-Köhler-Allee 401a, 79110 Freiburg, Germany

10 Instituto Nacional de Técnica Aeroespacial (INTA), Ctra. de Ajalvir, km. 4, E-28850 Torrejón de Ardoz, Spain

11 Instituto de Astrofísica de Canarias, Vía Láctea, s/n, E-38205 La Laguna, Spain

12 Departamento de Mineralogía y Petrología. Facultad de Ciencias. Avda. de Fuentenueva s/n, 18071 Granada, Spain

13 Universitat de Valencia Catedrático José Beltrán 2, E-46980 Paterna-Valencia, Spain

14 Satlantis Microsats S.A., Edif. Sede 2a planta, Parque Científico, Campus UPV Bizkaia, 48940 Leioa (Bizkaia), Spain

15 IRIS-2 Instrument Development Team, Bilbao, Spain

16 Technical University of Munich, Department of Aerospace and Geodesy, Lise-Meitner-Straße 9, 85521 Ottobrunn, Germany

17 Institut für Astrophysik und Geophysik, Georg-August-Universität Göttingen, 37077 Göttingen, Germany

18 Instituto de Microgravedad “Ignacio da Riva” / Universidad Politécnica de Madrid (IDR-UPM), Plaza Cardenal Cisneros 3, E-28040 Madrid, Spain

19 Dept. Optical Instrumentation Development, Korea Basic Science Institute, 169-148 Gwahak-ro, Yuseong-gu, Daejeon, South Korea

[20] Grupo de Estudios en Heliofísica de Mendoza, CONICET, Universidad de Mendoza, Boulogne sur Mer 683, 5500 Mendoza, Argentina

[21] National Institute for Fusion Science, 322-6 Oroshi-cho, Toki City 509-5292, Japan

[22] Centre for Integrated Data Science, Institute for Space-Earth Environmental Research, Nagoya University, Furocho, Chikusa-ku, Nagoya, Aichi 464-8601, Japan

[23] Universidad Politécnica de Madrid, Plaza Cardenal Cisneros 3, E-28040 Madrid, Spain

[24] Universidad de La Laguna, E-38205 La Laguna, Spain

[25] Institute of Space and Astronautical Science, Japan Aerospace Exploration Agency, 3-1-1, Yoshinodai, Chuo-ku, Sagamihara, Kanagawa 252-5210, Japan

[26] National Solar Observatory, 3665 Discovery Drive, Boulder, CO 80303, USA